Swimming of Multi-flagellated Bacteria

Dissertation

zur Erlangung des Grades
des Doktors der Naturwissenschaften
der Naturwissenschaftlich-Technischen Fakultät
der Universität des Saarlandes

Von
Javad Najafi

Saarbrücken
2018

Tag des Kolloquiums:	December 4th, 2018
Dekan:	Prof. Dr. Guido Kickelbick
Berichterstatter:	Prof. Dr. Christian Wagner
	Prof. Anke Lindner
Vorsitz:	Prof. Dr. Christoph Becher
Akad. Mitarbeiter:	Dr. Zeinab Sadjadi

I do not know what I may appear to the world, but to myself I seem to have been only like a boy playing on the seashore, and diverting myself in now and then finding a smoother pebble or a prettier shell than ordinary, whilst the great ocean of truth lay all undiscovered before me.

Isaac Newton

Saarland University

Abstract

Faculty of Natural Sciences and Technology
Department of Experimental Physics

Doctor of Philosophy

Swimming of Multi-flagellated Bacteria

by Javad Najafi

Many prokaryotes employ rotating helical appendages known as flagella to swim in an aqueous medium. We studied differentially flagellated *B. subtilis* strains as model systems study the dynamics of swimming bacteria with numerous flagella.

We found out that decreasing the number of flagella of individual cells reduces the average turning angle after the tumbling, enhances the run time and directional persistency of the run phase. Consequently, having a few flagella is beneficial for the fast spreading, while having many flagella is advantageous for the processes which require slower spreading. The results of numerical simulations based on the two-state model were used to discuss the search efficiency of different strains. Fluorescence microscopy shows that *B. subtilis* can make several bundles during the run phase, where the probability distribution of the number of bundles is similar for all strains independent of the flagellar number. The angle between the bundles on the observation plane widens with increasing the number of flagella, which leads to a slight modification of the effective cell aspect ratio while the other bundle properties do not significantly change.

The collective motion of dense suspension of bacteria was also investigated to understand how the swimming persistency of individual cells and their geometrical properties can influence characteristic features of the collective behavior. The results show that the characteristic time and length scale of the collective motion are robust to these parameters.

Universität des Saarlandes

Zusammenfassung

Naturwissenschaftlich-Technischen Fakultät
Fachrichtung Experimentalphysik

Schwimmen von Bakterien mit mehreren Flagellen

von Javad Najafi

Viele Bakterien nutzen Flagellen - kleine spiralförmige Anhänge - um sich zu bewegen. Beispielsweise können E. coli Bakterien ihre Flagellen synchronisieren und bündeln um aktiv zu schwimmen. Die Auswirkungen der Flagellenanzahl auf die Dynamik der Bakterien ist nicht genau verstanden. Daher haben wir Bakterien der Art B. Subtilis mit verschiedener Anzahl an Flagellen untersucht.

Die Verringerung der Flagellenanzahl reduziert den mittleren Änderungswinkel zwischen aufeinanderfolgenden Renn-Phassen und erhöht die Renn-Zeit sowie die Richtungsbeständigkeit. Eine geringe Anzahl von Flagellen ist daher vorteilhaft für Transportprozesse, wohingegen eine hohe Anzahl von Flagellen vorteilhaft für eine langsamere Verteilung wichtig ist (Entstehung von Biofilmen). Wir haben ein Zwei-Zustands Random-Walk Modell entwickelt, welches einen exakten analytischen Ausdruck für die Transporteigenschaften liefert. Die Ergebnisse der numerischen Simulationen dienten als Grundlage für die Diskussion der Such-Effizienz verschiedener Stämme. Wir konnten beobachten, dass verschiedene Flagellen-Bündel während der Renn-Phase entstehen.

Außerdem untersuchten wir die kollektive Bewegung in einer dichten Suspension von Bakterien. Die Ergebnisse zeigen, dass innerhalb der Reichweite unserer experimentellen Parameter die charakteristische Zeit- und Länge-Skalen der kollektiven Bewegung stabil gegenüber Form- und Persistenzänderungen einzelner Bakterien sind.

Acknowledgements

First of all, I would like to thank Prof. Dr. Christian Wagner for the opportunity that he gave me to pursue my Ph.D. in his group.

I thank all the members of the group with whom I had some great times during my Ph.D. years: Alexander, Andreas (Christ), Andreas (Gross), Asena, Christian, Daiki, Daniel, Francois, Greta, Jorge, Matthias (Brust), Matthias (Mussler), Oliver, Othmane, Revaz, Rishab, Sebastian, Stephan, Thomas, Viviana, Zakaria, and those who I may forget to name them. I am additionally very grateful to both Matthias for their help in the first weeks of my arrival to Saarbrücken and assisting a lot with the accommodation and initial administrative works. Thanks to Christian as my officemate, for his interest in my work, useful suggestions, and discussions. I am thankful to Oliver for the translation of abstract into German. Thanks to Elke and Karin for their help with the necessary paperwork and chemical preparation.

I appreciate Dr. Gert Bange for providing us with the bacterial mutants and Florian Altegoer for building the fluorescently stainable strains. I acknowledge Dr. Thomas John for his tracking code and technical help with some parts of my thesis. Thanks to Dr. Emmanuel Terriac for his early help with the fluorescent microscopy. My special thank goes to Dr. Mohammad Reza Shaebani for all the scientific, fruitful, and engaging discussions that we had during these years. I also appreciate him for supporting some part of my measurements by his analytical and numerical models. Thanks to Dr. Sigolene Lecuyer at LiPhy lab in Grenoble for her help with the protocol of biofilm growth and the time she spent on discussions and resolving arising problems. I regret that we lately, in my last year of Ph.D., started to collaborate with her and I could not find time to accomplish our idea.

I am very grateful to Zeinab who I will not forget her help and suggestions especially in the first months of my stay in Germany. I also would like to appreciate my friends in Saarbrücken with whom I had an enjoyable time: Ahmad, Amir Abbas, Amir Hossein, Daiki, Fatemeh (Behjati), Fatemeh (Torabi), Hamid, Hosna, Jiaqi, Majid, Maryam (Ghareghani), Maryam (Nazarieh), Mohammad Reza, Roqiyeh, Zahra (Hemati), Zahra (Mostajeran), Zakaria, and Zeinab. I also appreciate very much the time which the proofreaders spent to comment on my thesis.

And last but not least, my greatest and sincere gratitude goes to my parents and sisters for their constant support, encouragement, and unconditional love.

To my family...

Contents

1

Introduction

Bacteria are single cell organisms whose size is in the order of a few microns. They are abundant in the air, soil, water, as well as our mouth, intestine, skin, hair, and even in the food we consume [1]. Bacteria make an essential contribution to the total biomass on earth. The estimated total biomass of planktonic *Cyanobacteria* in the oceans exceeds the biomass of humans, and consequently, their profound impacts on the ecology and different aspects of mankind's life are not deniable [2]. They are widely considered as harmful and unwanted creatures because a few species can cause diseases or spoil food, while most of the microbes are beneficial [1]. Among others, bacteria that live in a digestive tract can help to break down substances for easier digestion and prevent invasion of the gut by yeast or fungi [3]. Industrial microbiology has been traditionally used to make valuable microbial products via fermentation processes including fermented foods and beverages [4]. Additionally, genetically engineered microorganisms have been employed in the production of feedstocks, energy sources, enzymes, food ingredients, and pharmaceuticals. They also play a crucial role in the water treatment and pollution control using their ability to degrade virtually all natural and man-made products [4]. However, most people are barely aware of their presence except when they become sick.

Bacteria are classified as *prokaryotes* since they do not have a membrane bounded nucleus [5]. They contain their DNA and other genetic materials as a single strand in their cytoplasm, and they reproduce themselves through so-called *binary fission* process [4]. In contrast, the cytoplasm of *eukaryotes* comprises a separated nucleus allowing them to replicate DNA. Eukaryotes such as *Chlamydomonas* are typically much larger than prokaryotes, ranging from ~10 μm up to 100 μm, and use more complicated functionality to produce energy and synthesize proteins in their organelle. They have the potential to turn into multicellular organs in animals and plants through functional differentiation [4–6]. Bacteria can tolerate extreme conditions by quick mutation or the high ability for adaption. Therefore, they were able to convey their life up to now through the very beginning of life on earth. Bacteria can be found in three basic morphological shapes of coccus, bacillus, and spiral [5]. Most of them employ similar appendages in diverse ways to intentionally propel themselves in the external medium. All kinds of bacteria respond to changes in the environment, such as chemical gradient, light intensity, and temperature, referring to the different types of *-taxis* or as Howard Berg nicely describes in his book "they can go where the grass is greener" [3].

Bacteria as microscopic swimmers, or similar systems that can take the energy from the environment and drive themselves far from the equilibrium, are known as

the *active matter* [7, 8]. Diverse bacterial species, particularly *E. coli* as a unicellular organism, have been served as simple model systems to study different features of life. The detailed classical picture of bacterial motility has been drawn by the seminal work of Howard Berg on intestinal bacterium *E. coli* around half a century ago [9]. On the one hand, in the last two decades *miniaturization* and the field of active matter, in particular, microswimmers, have rapidly expanded along with the demand for designing of nanomachines. On the other hand, this rapid growth is indebted in part to new experimental methods such as visualization techniques (e.g., fluorescent staining of flagella) and the ability to measure the forces at the scale of single microorganisms (e.g., optical tweezers and atomic force microscopy) for studying cell motility. Indeed, various aspects of motility in the small scale need to be carefully studied, since a bright propulsion approach is exploited in this scale due to the dominant viscous forces in the limit of *low Reynolds number*. The acquired knowledge has, in fact, applications in various disciplines such as statistical physics [7], biology [10], robotics [11], social transport [12], soft matter [8], biomedicine [13], biomimetic, and drug delivery. Tremendous efforts have been recently made to fabricate artificial micro- and nanoswimmers that can drive themselves based on diverse propulsion mechanisms [14–17]. The potential applications of artificial self-propellers depend on their key functionalities, namely transport, sensing, and manipulation. These small-scale machines are expected to perform delicate tasks in an autonomous, targeted, and selective way [18]. The significant challenges in this attempt are the availability of sustainable energy sources and physical concepts for efficient energy conversion to propulsive force. The other issue is how to actively control them to respond to external stimuli or perform tasks [19].

Biological microswimmers that are usually found as assemblies of motile microorganisms, cooperatively move together and have rich dynamic and social behavior. They release chemicals that signal their neighbors to change their behavior in high concentrations, a phenomenon known as *quorum sensing* [20]. It is fascinating how bacteria employ hydrodynamics and geometry as well as biochemistry to establish their social interactions. Nevertheless, the contribution of these factors, in reality, is still an open question [20]. Despite the differences in length scales and cognitive abilities of the individuals in bacteria and other larger systems such as bird flocks or mammal herds, similar emerged spatiotemporal patterns suggests general principles and universality of the collective motion [21]. Synthetic self-propelled objects can also move collectively in high concentrations. However, their behavior is not as sophisticated as biological swimmers and is more controllable. Swimming microorganisms are known to undergo *bioconvection* that is driven by the changes in buoyancy exerted on the fluid in the presence of concentration gradients of the microswimmers [22]. This phenomenon happens when cells, on average, swim upwards either due to gravitational torque keeping them upward aligned or they do chemo- or phototaxis [20]. Many bacterial species can adapt to their environment by secretion of protective extracellular polymeric substance (EPS) to form *biofilm* in adverse conditions as a sessile mode [23] or *swarm* to colonize on nutritious solid substrates [24].

This thesis includes six chapters. The first chapter is devoted to a general introduction to give an insight about the research area and whole dissertation. The required backgrounds will be provided in the second chapter where readers who are unfamiliar with biology can get information about the general field as well as the specific bacterial strains that have been used in this study. Mathematical and theoretical essentials can also be found in the second chapter. The main body of the research will be presented in chapters three to five, including swimming in the single cell level, fluorescent visualization of the flagellar bundles, and finally collective motion of the

dense bacterial suspensions, respectively. Each chapter contains a short review of the past relevant works, motivation, methods, and results along with the discussion and summary. General conclusion will be presented in the sixth chapter and a few outlooks will be suggested for the future studies.

2

Background

Contents

2.1 Biology

2.1.1 Motility strategies

Movement is crudely known to be the most obvious feature of life. All creatures including plants need to move in different speeds depending on the environmental conditions. Henrichsen identified six different categories for the motility of microorganisms: swimming, swarming, twitching, gliding, sliding, and darting [26]. These categories are described in the following.

Swimming

Swimming is perhaps the most studied tactics of movement although there are some other types depending on the different surrounding situations. Physicists, in a very rough manner, consider swimming as a movement generated by deformation of the body of an object or creature in a periodic way [27]. Many microorganisms use one or

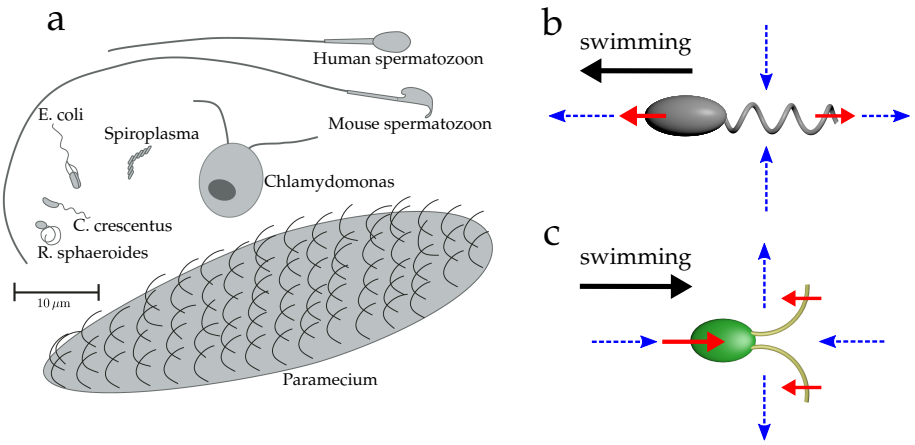

Figure 2.1: (a) The movement of these cells are generally considered as different approaches of swimming [25]. Flow fields around a pusher (b), and puller (c) cell are depicted by the blue arrows. See the text for more details.

more moving appendages known as flagella to propel themselves. This attachment in prokaryotic cells such as *E. coli* is a rather stiff helix that is rotated by a motor embedded in the cell membrane. In eukaryotic cells such as *Chlamydomonas* or spermatozoa of many species, the moving appendage is a flexible filament undergoing whip-like motion due to the activity of molecular motors distributed along the length of filament [25]. There are some other elegant kinds of motion which are included in this description (Fig. 2.1a). *C. crescentus* employs a single right-handed helical filament driven by a rotary motor that can spin in either direction. The preferential turning direction of the motor that pushes the body forward is clockwise. Counter clockwise rotation of the motor pulls the body instead of pushing. The extended helical filament of *R. sphaeroides* turns in only one direction but stops from time to time and makes a compact coil at the end of the cell body [25]. There are also bacteria that swim without any external flagellar filaments. The axial flagella of spirochetes such as *B. burgdorferi* lie in the thin periplasmic space between the inner and outer layer of cell membranes. Its body is deformed as it swims, which is probably due to the rotation of periplasmic flagella. *Spiroplasma* is also a helically shaped bacteria without flagella, and it moves by the propagation of pairs of kinks along the length of its body. The kinks are supposed to be formed by the contraction of the cytoskeleton instead of periplasmic flagella [25]. In a more precise classification of motility, the importance of flagella and individual cell movement in the bulk of aqueous medium is emphasized in the definition of swimming [24, 28].

Swimmers depending on the flow fields that create around themselves are divided into pushers and pullers as shown in Fig. 2.1b and c. Pushers like *E. coli* drive fluid back from the body along the long axis and draw fluid into the sides, while pullers like *Chlamydomonas* draw fluid in along the elongated direction and push fluid out from the sides. One should note that some cells such as *Caulobacter* can switch between pusher and puller mode when they change the direction of motor rotation [25] (see Figs. 2.1 and 2.2a).

Swarming

The other important moving strategy in which flagella play a crucial role is swarming motility (Fig. 2.2b). It is practically defined as a fast collective motion of bacteria on top of a surface powered by rotating flagella. This simple definition lacks several

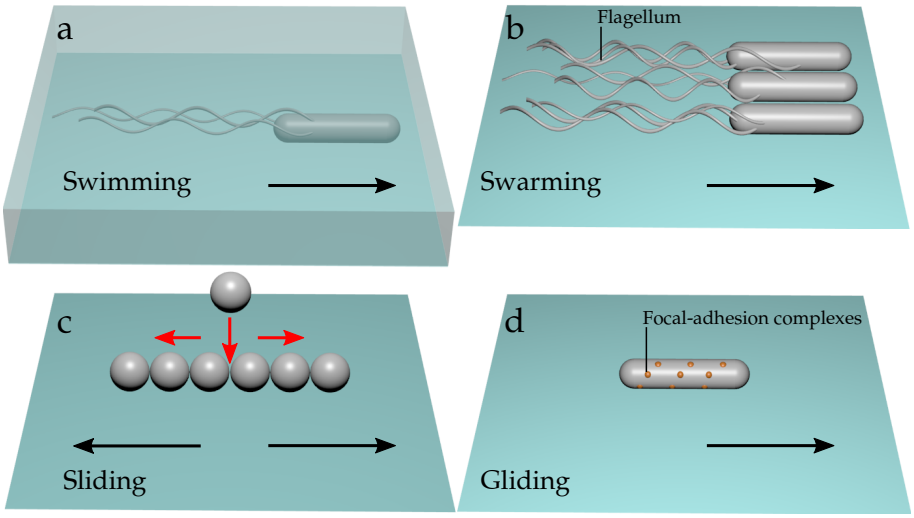

Figure 2.2: Schematic demonstration of important motility tactics. (a) Swimming is an individual motion in the bulk of fluid that is derived by rotating flagella. (b) Swarming is a collective motion of cells over a surface that alike to swimming is powered by rotating helical flagella. (c) Sliding is a passive surface displacement due to growth and is assisted by surfactant secretion. (d) Gliding is an active surface motility without the aid of flagella or pili and involves focal-adhesion complexes. Colored circles indicate the motors that drive the cell movement. Black arrow in each image represents the direction of cell movement [24].

important features of swarming such as the behavior associated with swarming of wide array of phenotypes. Indeed, solidified media with agar concentration above 0.3% prohibits swimming of bacteria and forces them to move over the surface. However, agar concentration above 1% stops swarming of most of the bacterial species. Swarming may naturally happen on nutrient-rich, soft substrates such as hydrated soils, plant roots, and animal tissues since the ideal surface of precisely dried agar plate cannot be found in the nature [24]. There is a lag time before the swarming motion starts and after cells are placed on the agar surface. Cells experience a physiological change during this period, and together with elongation synthesize more flagella that is known as *hyperflagellation* [24]. In fact, it appears that more flagella are needed for swarming over a surface than for swimming in the liquid media. This is probably due to the higher friction or viscosity of the agar surface, but it is not yet clear whether hyperflagellation is required for raft formation or not [24, 28]. Some bacterial species also secrete a kind of biological surfactant called *surfactin* to lubricate the surface and facilitate spreading, while without its presence the swarming would be suppressed. Some others can synthesize separate and distinct flagella for swimming and swarming, while many of them exploit only one kind of flagella for both modes of motility [28, 29]. It has been shown that flagella is specific only to swimming and swarming, and they do not play any role in the other types of movement [24].

Twitching

Twitching motility in some species such as *P. aeruginosa* is a kind of single cell movement over wet surface powered by the so-called polar *type IV pili* which operate in a way similar to a grabbing hook. These pili are about 6 nm in diameter and up to 4 μm in length and typically can be found in both poles [28]. Twitching occurs by the extension, attachment, and then retraction of the pili, and bacteria pull themselves over the surface which often leads to a slow motion of the cell along a

jerky trajectory [30, 31]. Radial expansion rates of colonies via twitching can reach 0.3 μm/s [28]. Twitching is important in the host colonization by a wide range of plant and animal pathogens, as well as in biofilm formation [32] and fruiting body development [30].

Sliding

Sliding or spreading motility is a passive form of cell spreading over a surface which does not use any active motor. It instead relies on production of surfactant to decrease the surface tension and allow the cells to spread away from the origin driven by the outward pressure of the growing cells (Fig. 2.2c). There is a strong correlation between the surfactant secretion such as lipopeptides, lipopolysaccharides (LPS), and glycolipids and sliding motility. Colony front can spread from relatively slow (0.03 μm/s in *S. smegmatis*) to moderately fast (2-6 μm/s in *S. marcescens*) [28]. Swarming sometimes is mistaken with this type of motility especially when the flagella are interrupted in bacteria and they cannot basically do swarming [24]. Despite the passive form of spreading, this type of movement probably plays an important role in bacterial surface colonization.

Gliding

Gliding motility is a kind of active surface movement along the long axis of the cell body without the aid of flagella (Fig. 2.2d). Gliding bacteria are phylogenetically[1] various and are abundant in many environments. Gliding generally requires the cell body movement using *focal adhesion complexes* on the cell membrane that could be bound to a substrate surface. However, more than one mechanism is often required to describe all forms of bacterial gliding motilities, e.g., *M. xanthus* social gliding motility is similar to twitching motility and depends on type IV pilus extension and retraction for cell displacement [33]. The advancing edges of gliding bacteria resemble to those of swarming and twitching motilities, and are also connected to reversals. The mechanism of other types of gliding still remains as a secret and it is possible that several different mechanisms are involved in gliding [28].

Darting

Darting is the most enigmatic type of surface motility. It is produced by developing expansive forces in an aggregate of cells insides a common capsule that ends up with an ejection of cells from the aggregate. Cells and aggregates of cells are distributed at random places with some empty areas left on the agar plate in the micromorphological pattern. Cell pairs or aggregates cannot move except during the ejection which is observed as a flickering under the microscope [26].
The common motility strategies are schematically summarized in Fig. 2.2 [24].

2.1.2 Flagellar structure

Prokaryotic flagella

The bacterial flagellum of prokaryotes is composed of over 20 protein species with approximately another 30 proteins required for regulation and assembly [34]. The bacterial flagellar motor is a nanomachine with ~50 nm in diameter. It spins either clockwise (CW) or counter clockwise (CCW) at speeds on the order of 100 Hz driving

[1] Evolutionary history and relationships among individuals or groups of organisms

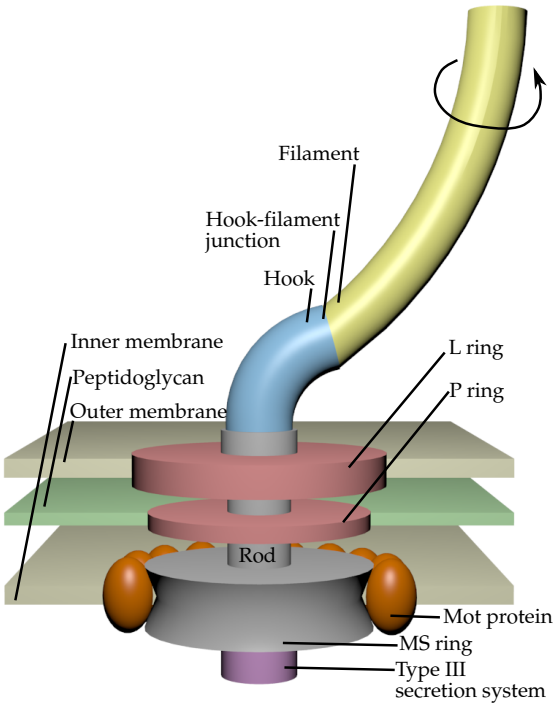

Figure 2.3: The primary composing units of prokaryotic flagella consist of a filament, hook, and membrane-embedded motor. The motor is driven by the proton-motive force and mainly includes a rod, series of rings, Mot proteins, and switch complexes (not shown).

long thin helical filaments that enables cells to swim. Receptors near the surface of the cell sense the concentration of desired molecules such as sugars, amino acids, and dipeptides and control the direction of flagellar rotation. The probability of CW spinning is increased by CheY that is a chemotactic signaling protein. CheY binds to the cytoplasmic side of the flagellar motor when it is phosphorylated. The phosphorylation of CheY is catalysed by a kinase whose activity is controlled by chemoreceptors. The activity of the kinase is reduced by the extra attractant. A transmembrane electrochemical gradient or *proton-motive force* powers protons to run the motors. Adenosine triphosphate (ATP) plays a role only in motor assembly and in chemotactic signaling, i.e., the coupling of receptors and flagella. Some gram negative marine bacteria have motors that are driven by sodium ions instead of protons [35].

The structure of flagella consists of three major units namely basal body, hook and filament as shown in Fig. 2.3. The basal body comprises a rod, a series of rings, the Mot proteins, the switch complex, and the flagellum-specific export apparatus. The rings attach the flagellum to the cytoplasmic membrane (MS ring), the peptidoglycan (P ring), and the outer membrane (L ring). The flagella of gram positive bacteria lack the P and L rings [34]. The basal body is a passive structure that transfers the torque from the motor to the hook and then to the filament [36]. The flagellar motor is operated by a rotary mechanism and can be subdivided into stator and rotor. The switch proteins (FliG, FliM, and FliN)[2] permit the flagellum to change the rotation direction and consequently, the orientation of swimming in response to the environmental signals that are detected by complex chemotaxis system [34]. FliM and FliN morphologically form a cytoplasmic cup- or ring-like structure called the

[2]Genes for which mutant cells lacked flagellar filaments were originally called *fla* representing flagellum, but after more than 26 had been found, the nomination simplified; *fla* genes are now indicated by *flg*, *flh*, *fli*, or *flj* depending upon their location on the genetic map. Genes for which mutant cells lead to disabled flagella are called *mot* representing motility [35].

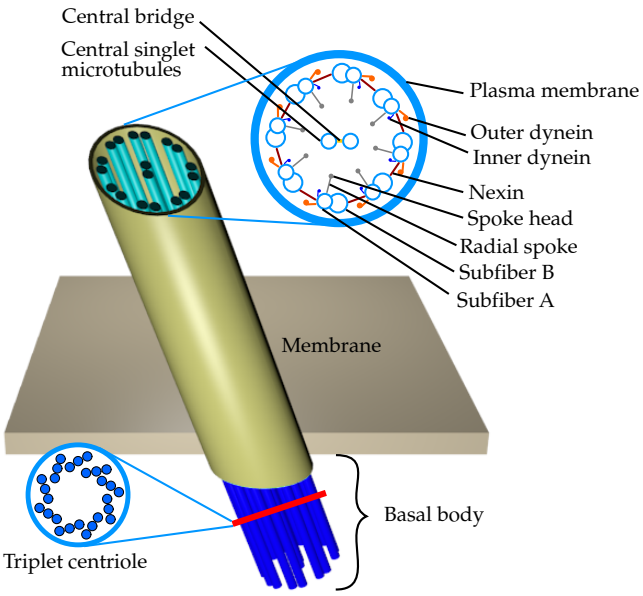

Figure 2.4: Axoneme composed of two central microtubules surrounded by another nine pairs of microtubule on the periphery of a circular section. The microtubules are connected by means of linker proteins. Bending of eukaryotic flagella is active and imposed by motor proteins connecting neighbor pairs of microtubules.

C ring. FliG participates in switching and torque generation, FliM is the target for the output of the sensory transduction chain, and yet the role of FliN is unclear. The flagellar hook has a cylindrical structure constructed in a similar way to the filament and operates as a flexible universal joint that plays an important role in enabling the filaments to make a bundle [36]. The hook region, unlike the filament, has a defined length of 55 nm that is composed of approximately 120 subunits of FlgE [34]. The filament is a long, cylindrical structure with about 20 nm in diameter and helical in shape, and it functions as a propeller when rotated. The growth of the filament is unusual since the individual flagellin monomers are added to the distal tip furthest from the cell [34]. The entire flagellar structure from the basal body through the hook and filament is ~3 nm hollow tube allowing for the passage of new subunits. There is a capping structure at the tip of the growing filament that is made of pentamer of HAP2 and resembles a plate structure with five legs extending downwards interacting with the filament [34, 36]. The genes which have contributed to building different parts of flagella can be found in [37].

Eukaryotic flagella

Eukaryotic flagella or *cilia* are hair-like extensions that consist of longitudinal fibrils or tubules arranged as a number of peripheral pairs plus a central pair. The number of outer pairs is often nine, although many other numbers and modifications of this main pattern have been observed. 'Arms' consisting of dynein protrude from the outer pairs of fibrils [38]. The bundles of microtubules are stabilized by the both *interdoublet* or *nexin* links and radial spokes that are known as connecting proteins. Electron microscopy studies have revealed that the microtubules keep their length constant during the bending and the bending is associated with longitudinal switching of the radial spokes [39]. Motor proteins connecting neighbor pairs of microtubules induce a local active bending force by sliding the microtubules relative to each other. Therefore, the motor activity is spread all over the length of the eukaryotic flagellum. The

described structure of eukaryotic flagella is called *axoneme*. The structure of axoneme, which is well conserved across all eukaryotes, is shown in Fig. 2.4 [19]. Propulsion is always obtained by propagation of waves along the cilia or flagella. This wave is usually propagated from the base to the tip and could be planar, helical, or some combination of the two waves. One can typically find about two wavelengths along the flagella, and the direction of propulsion is normally opposite to the direction of wave propagation. The energy source for the motion is ATP that could either diffuse along the length of the flagellum or be diffused in from the surrounding fluid [38]. The phase of the beat in which the cilium is generally straightened out and the microorganism propelled is termed *effective stroke*. The rest of the beat is known as the *recovery stroke* and the cilium slides back to its beginning point in a bent position. In the recovery stroke, a noticeable part of the cilium moves tangential to the fluid rather than normal to it as in the case of effective stroke. The ensemble of eukaryotic cilia often shows *metachrony*: a cilium beats slightly out of phase with its neighbor in one surface direction to make metachronal wave travelling over the surface. The direction of propagating wave could have almost any orientation relative to the direction of the effective stoke. Many microorganisms can reverse the direction of metachronal wave propagation and thus their direction of motion that is known as *ciliary reversal* [38]. Some of the significant differences between the cilia and eukaryotic flagella are their length, number, and occurrence place on the cell membrane [19].

2.1.3 Flagellar polymorphism and tumbling

Every flagellar filament consists of 11 *protofilaments* on the surface of a cylinder that have been slightly tilted relative to the cylindrical axis. Each of the 11 protofilaments composed of approximately 20,000 flagellin proteins (FliC) and can be in a left-handed (L) or right-handed (R) state when all the subunits within the protofilament are in the same state (L or R). Assembly of protofilaments by only one type of flagellin monomers refers to *Calladine's rule* [40]. The L state has about 0.8 Å longer intersubunit distance than R state. A normal filament will contain a mixture of both L and R protofilaments with the short protofilaments running along the inside of the helical shape. Mechanical strain energy is minimized when short or long protofilaments are next to the same type leading to 12 possible conformations. The final shape of the bacterial filament depends on the number of L-type protofilaments (n_{L}) and the corresponding number of R-type protofilaments ($n_{\mathrm{R}} = 11 - n_{\mathrm{L}}$). A filament composed entirely of L-type (R-type) protofilaments is straight with a left-handed (right-handed) structure. Short protofilaments can arrange together and form helical structures if the filament is made of protofilaments of different lengths [34, 35]. Different stable polymorphic shapes of the filament have been predicted by Calladine using the theory of elasticity, which are represented in Fig. 2.5a. The transformation between different shapes are called *polymorphic transition* and can happen due to a change of the amino acid sequence of the proteins, pH value (acidity), temperature, ionic strength (salt content), and mechanical twist (torsion) [44].

Tumble starts with loosening the bundle near the cell body and afterwards, one or more filaments disjoin from the bundle and consequently the cell body changes the direction. Separated filaments display right-handed waveforms (usually semicoiled and then curly 1), and therefore, their driving motors must have switched from CCW to CW [44]. According to the models of Calladine [40] and Kamiya [45], the succession of waveforms that expected to increase the twist is normal, coiled, semicoiled, and curly 1. This is the order that was observed experimentally during tumbles except for the absence of coiled waveform. Curly 2 has been observed with the filaments

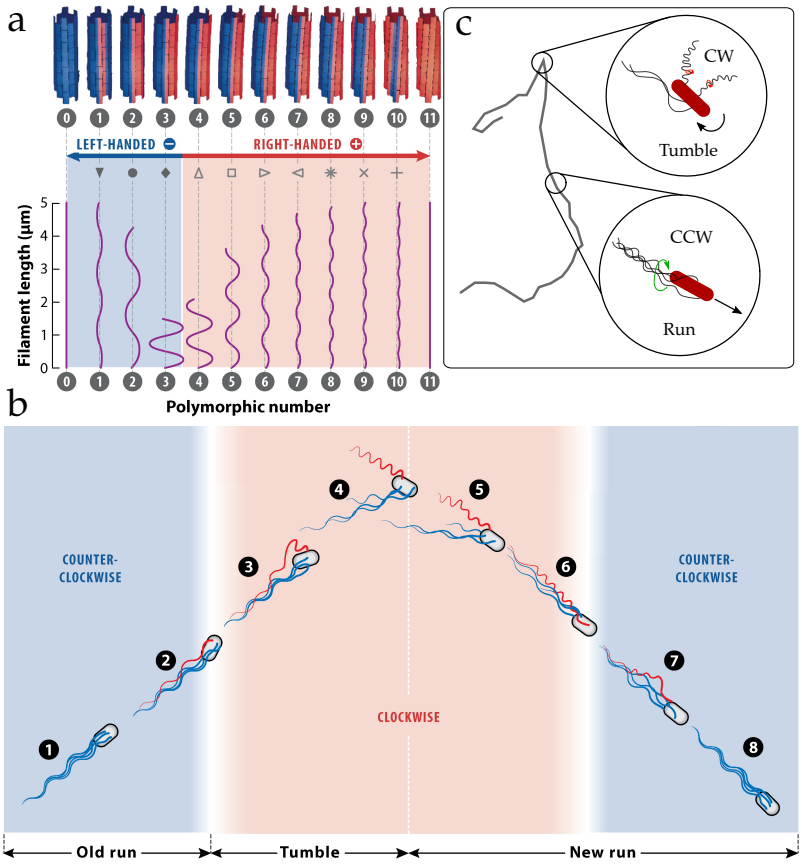

Figure 2.5: (a) Twelve polymorphic shapes of the bacterial filament that have been obtained using Calladine's model for a defined initial length of the filament [40–42]. (b) An ideal sequence of events in a tumble is initiated by CW rotation of a single motor. The lower time line represents the behavior of the cell as determined by the motion of cell body. The common order of polymorphic states expected to be observed during tumbling is semicoiled (3-4), curly 1 (5-6), and normal (7-8) [42–44]. (c) Schematic of the run-tumble motion and turning event along a trajectory.

stuck to the glass. Curly 1 waveform appears to be relatively flexible and often wraps around normal filaments or the bundle. The end of the tumble can be defined when the filaments return to the bundle or the cell starts to move in a new well-defined direction. Bundle consolidation takes about 0.43±0.25 s but cells tend to move in a new well-defined direction before consolidation is complete [44]. Tumbling stages are demonstrated in Figs. 2.5b and c.

2.1.4 Cell biology of *B. subtilis*

B. subtilis is a gram positive and rod-shaped bacterium that is naturally found in soil and gastrointestinal tract of ruminants and humans (see Fig. 2.6). It can form a tough protective endospore allowing it to sustain extreme environmental situations. It is also considered as the best studied gram positive bacterium and a model organism to study bacterial chromosome replication and cell differentiation. The length of *B. subtilis* cells ranges from 4-10 μm and they are heavily flagellated in comparison with *E. coli* as their gram negative counterpart [46]. More than 30 structural proteins participate to synthesize flagella and each flagellum is assembled in three stages. First, the basal body is quickly assembled in less than five minutes post initiation. Then, the hook has to be assembled before the filament that takes 10-20 minutes post

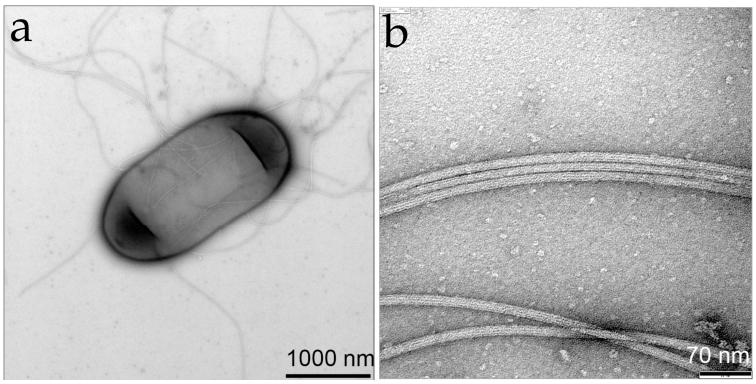

Figure 2.6: Electron microscopy images of a wild type *B. subtilis* cell (a), and its filaments (b). Images have been taken by Florian Altegoer at Philipps University in Marburg.

initiation to assemble flagellar hook. Flagellar filament synthesis capable of supporting motility is rate limited due to polymerization and is started within 15 minutes after fla/che operon[3] induction and completed after approximately another 25-45 minutes of assembly [48].

The strains that were used in this study have been primarily built by Daniel B. Kearns' lab at Indiana university and handed over to us by Gert Bange's lab at Philipps university in Marburg. In the following, the biological properties of these strains will be shortly described, and the interested reader can study the paper by Sarah B. Guttenplan et al. [48]. The flagellar number can be counted indirectly by counting the number of basal bodies using super resolution images of FliM-GFP. Wild type cells WT have an average of 26±6 basal bodies (N=42 cells), and the number of basal bodies generally increases with growing the cell length. *B. subtilis* synthesizes 3-8 times more flagella per cell than *E. coli* and its flagellar number is thought to be controlled by SwrA. The flagellar number per cell seems to decrease and increase with respect to wild type when SwrA is either mutated (ΔswrA) or overexpressed from an artificial P_{hyspank} promoter (swrA^{++}) in a strain encoding the hag_{T209C} filament protein. Single cells of the ΔswrA mutant on average synthesize 9±2 basal bodies and flagellar filaments per cell (N=43 cells), but in contrast to the wild type, the number of basal bodies does not increase proportionally with cell length. In contrary, cells overexpressing SwrA (swrA^{++}) synthesize an average of 41±6 basal bodies (N=42 cells), and the number of basal body appears to be correlated strongly with cell length in comparison with wild type. The average distance of nearest neighbors for all basal bodies is 0.39±0.14 μm (N=42 cells) in the wild type. This distance in SwrA mutant enhances nearly twofold, probably because cells missing SwrA synthesize half the number of basal bodies per wild type cell. However, the twofold over production of basal bodies in cells over expressing SwrA (swrA^{++}) reduces the mean nearest neighbor distance by only ~20%. The obtained minimum distance between basal bodies is greater than expected for a random distribution. Unlike *E. coli* cells that their flagellar distribution is considered as peritrichous with random dispersion on the cell body, well dispersed basal bodies of *B. subtilis* often appear to make spiral or helical patterns on the cell surface. Patterns may emerge either by spontaneous stochastic fluctuations or are imposed by cellular localization systems. Pattering in the case of *B. subtilis* is genetically determined, and FlhF and FlhG have an effect on flagellar positioning instead of controling the number of flagella per cell. In addition

[3]In genetics, an operon is a functioning unit of genomic DNA containing a cluster of genes under the control of a single promoter [47].

to nonrandom distribution of flagella over the cell body of *B. subtilis*, four other noticeable aspects of flagellar pattering are observed in the wild type. First, it is less probable that basal bodies to be synthesized at the poles. Second, basal bodies do not appear on the division septum. Third, basal bodies are distributed in a grid-like pattern. Fourth, basal bodies are symmetrically distributed with respect to the middle of the cell. Indeed, optimum spacing and symmetrical distribution of flagella can be a plan to ensure more stable segregation of flagella during cell division and equal inheritance of a powerful propulsion force [48].

2.2 Low Reynolds number

The dynamics of an incompressible Newtonian fluid is described by the Navier-Stokes equation,

$$\rho\left(\frac{\partial \mathbf{u}}{\partial t} + \mathbf{u}.\nabla\mathbf{u}\right) = -\nabla p + \eta\nabla^2\mathbf{u} + \mathbf{f}, \tag{2.1}$$

where ρ, ∇p, η, and $\mathbf{f}$ respectively stand for density, pressure gradient, dynamic viscosity, and external force per unit volume such as gravity on the body. The flow field $\mathbf{u}$ must satisfy the continuity equation,

$$\nabla.\mathbf{u} = 0. \tag{2.2}$$

The Navier-Stokes equation is the equivalent of Newton's second law for small element of fluid. This equation can be scaled using a characteristic length L, a characteristic velocity U, and a characteristic time $T = L/U$ of the system. After substituting $\mathbf{u} = U\tilde{\mathbf{u}}$, $t = T\tilde{t}$, $\nabla = \tilde{\nabla}/L$, and $\mathbf{f} = |\mathbf{f}|\tilde{\mathbf{f}}$, one can get the dimensionless Navier-Stokes equation,

$$Re\left(\frac{\partial \tilde{\mathbf{u}}}{\partial \tilde{t}} + \tilde{\mathbf{u}}.\tilde{\nabla}\tilde{\mathbf{u}}\right) = -\tilde{\nabla}\tilde{p} + \tilde{\nabla}^2\tilde{\mathbf{u}} + \frac{Re}{Fr^2}\tilde{\mathbf{f}}, \tag{2.3}$$

where Fr is the *Froude number* and is defined as,

$$Fr \equiv \left(\frac{\text{inertial force}}{\text{gravitational force}}\right)^{1/2} = \left(\frac{\rho U^2/L}{\rho g}\right)^{1/2} = \frac{U}{\sqrt{gL}}. \tag{2.4}$$

The dimensionless number Re is the *Reynolds number* and allows for qualitative prediction of the flow regime [49]. The most common interpretation of the Reynolds number in the absence of external force is the ratio of inertial term in the Navier-Stokes equation (left-hand side) to the viscous force per unit volume (right-hand side) [49],

$$Re \equiv \frac{\text{inertial force}}{\text{viscous force}} = \frac{|\rho\mathbf{u}\nabla\mathbf{u}|}{|\eta\nabla^2\mathbf{u}|} \sim \frac{\rho UL}{\eta}. \tag{2.5}$$

The Reynolds number can be interpreted as the ratio of the forces acting on an object independent of the Navier-Stokes equation and described in different ways. Using the dynamic pressure $\sigma_{\text{inertial}} \sim \rho U^2$ in Bernoulli equation of conservation of energy, one can estimate the inertial force acting on an object as $f_{\text{inertial}} \sim \sigma_{\text{inertial}} L^2 = \rho U^2 L^2$. The viscous stress is proportional with shear rate and dynamic viscosity, $\sigma_{\text{viscous}} \sim \eta U/L$, from which one can get a typical viscous force as $f_{\text{viscous}} \sim \sigma_{\text{viscous}} L^2 = \eta UL$. Therefore, Reynolds number can be written as $Re = f_{\text{inertial}}/f_{\text{viscous}}$ and in a low Reynolds number flow the viscous drag is dominated [25].

Another interpretation is given as the ratio of time scales. The time scale for a local velocity perturbation to diffuse away from the body by the viscosity is $t_{\text{diff}} \sim \rho L^2/\eta$,

while it takes $t_{adv} \sim L/U$ for the perturbation to be transported by the flow along the body. Accordingly, $Re = t_{diff}/t_{adv}$ and in low Reynolds number fluid transport is governed by the viscous diffusion [25].

Purcell has also suggested an interpretation of the Reynolds number in his paper [27], where he notes that $\mathcal{F} = \eta^2/\rho$ has the units of force. It is straightforward to see that $Re = f_{viscous}/\mathcal{F}$ and $Re = (f_{inertial}/\mathcal{F})^{1/2}$ by rearrangement of Eq. 2.5. Therefore, any body in an arbitrary size subjected to the force $\mathcal{F}$ will have a Reynolds number of unity and $f_{inertial} = f_{viscous} = \mathcal{F}$. The body will move at low Reynolds number when it experiences a force smaller than $\mathcal{F}$ where the characteristic force is $\mathcal{F} \sim 1$ nN for water [25].

A typical bacterium such as *E. coli* with a body length $L \sim 1$ μm swimming with the velocity $U \sim 10$ μm/s in water ($\rho \sim 10^3$ kg/m^3 and $\eta \sim 10^{-3}$ Pas) experiences the Reynolds number $Re \sim 10^{-5}$. In such a small Reynolds number, it is appropriate to neglect the inertial terms in the Navier-Stokes equation to get the *Stokes equation* [25],

$$-\nabla p + \eta \nabla^2 \mathbf{u} = 0, \qquad \nabla . \mathbf{u} = 0. \tag{2.6}$$

The fluid dynamics in low Reynolds number regime is described by linear and time independent Stokes equation. Linear nature of the equation allows for analytic solution while there is usually no exact solution for the nonlinear Navier-Stokes equation. Stokes equation simply indicates that at every point local pressure gradient is balanced with viscous forces. The time independency of Stokes equation has an interesting consequence that bacteria cannot use appendages moving with time-reversal symmetry to generate thrust [27]. Indeed, the movement in low Reynolds number is very different from our daily experience of animals or human swimming which takes place in high Reynolds number. Inertial forces do not play an important role in low Reynolds regime since any movement is damped by viscous drags. Purcell, for the first time, discussed that a microorganism can only swim by cyclic deformation of its body or by an external appendage in a way that its motion must be time independent and non-reciprocal. This principle is known as *scallop theorem* [27]. In the high Reynolds number the rate of momentum transfer determines the amount of generated thrust force while in the low Reynolds regime the inertia term is irrelevant. However, a scallop can move in the sea by periodically opening and closing its shells with different rates. This is possible since the opening cycle is performed faster than the closing one, and consequently the thrust force generated from opening stroke is higher than the thrust force generated during closing stroke [27].

2.3 Theory of flagellar propulsion

The sequence of body deformations without breaking the symmetry after time reversal cannot generate any net displacement in low Reynolds regime. Therefore, any deformation with only one degree of freedom, such as scallop movement, cannot generate a net displacement in low Reynolds regime as it is always reciprocal. In fact, microorganisms employ deformation of appendages with at least two degrees of freedom in a non-reciprocal way to propel themselves. In this section, the propulsion matrix formalism for a swimming bacterium in low Reynolds regime, which was proposed by Purcell, will be reviewed [27]. Then, *resistive force theory* (RFT) and *slender body theory* (SBT) will be shortly surveyed.

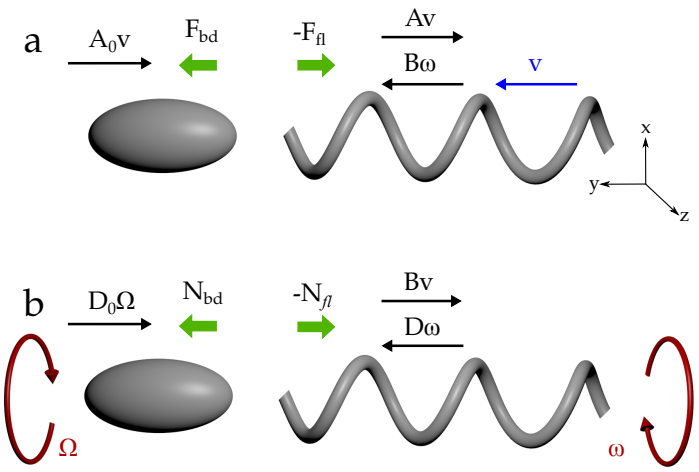

Figure 2.7: Propulsion matrix formalism for the helical filament. (a) The counter clockwise rotating (viewing from the back of cell) left handed helix with angular frequency ω generates the propulsive force $B\omega$ and pushes the helix and body with velocity v. The thrust force is balanced by the opposing translational drag Av of the helix and $A_0 v$ of the cell body. (b) The total moment generated by the rotating filament $D\omega - Bv$ is similarly balanced by the counter rotational drag $D_0\Omega$ of the cell body. Schematics adapted from [6] and [50].

2.3.1 Propulsion matrix

A bacterium uses one or several rotating flagella to swim in aqueous medium. Purcell approximated the bundle of flagella as a rotating, single thick helix that is connected to an elongated cell body. He neglected the interaction between the cell body and bundle of flagella. He considered a swimming bacterium with constant velocity to be force and torque free in the absence of external forces. The thrust force and torque generated by the helix can be written as a linear function of the angular velocity of the helix ω and its translational velocity v due to the linearity of Stokes equation (see Fig. 2.7),

$$-F_{\text{fl}} = Av - B\omega, \tag{2.7}$$

$$N_{\text{fl}} = -Bv + D\omega, \tag{2.8}$$

where A and D are respectively translational and rotational drag coefficients exerted on the helix. The coefficient B couples the translational movement to the rotational movement and implies an interesting physical principle of the model: a translating propeller under the influence of an external force and absence of torque has to rotate, and a rotating propeller under the influence of an external torque and absence of force has to translate [27]. One can alternatively consider B as a measure of the force necessary to stop a rotating helix from translating (Eq. 2.7) or the torque necessary to stop a translating helix from rotating (Eq. 2.8). The torque N_{fl} is generated by the motors that exert the propulsive force F_{fl} on the helix. Propulsion force F_{fl} and velocity v are positive when they point out towards the head of the cell. The sign of N_{fl} and ω obeys the right hand rule for the left handed helix of flagellar filaments. The sign in front of the coefficient B is determined by the orientation of helix [51]. The two above equations can be summarized as

$$\begin{pmatrix} -F_{\text{fl}} \\ N_{\text{fl}} \end{pmatrix} = \begin{pmatrix} A & -B \\ -B & D \end{pmatrix} \begin{pmatrix} v \\ \omega \end{pmatrix}. \tag{2.9}$$

The matrix of coefficients in Eq. 2.9 is known as propulsion or resistance matrix [27]. The elements of propulsion matrix are all positive and depend on the geometrical properties of the propeller such as pitch, radius, and thickness of the helix. These coefficients can be derived using slender body or resistive force theory depending on whether the long range hydrodynamic interactions between individual segments of the helix are included or not. The coefficients will be derived from the resistive force theory and discussed in section 2.3.2. The described propulsion matrix by Purcell can be applied to propellers with different shapes as long as they are asymmetric.

The cell body is independently considered as an elongated ellipsoid which because of the symmetry cannot generate thrust. One can describe the drag force and torque experienced by the body in a similar way to the helix,

$$\begin{aligned} F_{\mathrm{b}} &= -A_0 v, \\ N_{\mathrm{b}} &= -D_0 \Omega, \end{aligned} \tag{2.10}$$

where $A_0 = 4\pi\eta b/(\ln(2b/a) - 1/2)$ is the translational drag coefficient and $D_0 = 16\pi a^2 b/3$ is the rotational drag coefficient [52]. Parameters a and b are the minor and major axis of the ellipsoid, respectively, and η represents the viscosity of medium. The ellipsoid moves along its major axis and Ω is the angular velocity of the body around the same axis. The body of cell usually experiences larger drag due to its size in comparison to helical bundle and therefore, for most cells $\omega > \Omega$ to satisfy the torque free condition. Eqs. 2.10 can be written as a matrix equation to get the propulsion matrix of the cell body,

$$\begin{pmatrix} F_b \\ N_b \end{pmatrix} = \begin{pmatrix} -A_0 & 0 \\ 0 & -D_0 \end{pmatrix} \begin{pmatrix} v \\ \Omega \end{pmatrix} \tag{2.11}$$

The cell body is not self-propeller therefore the coupling coefficient B vanishes and the propulsion matrix becomes diagonal. The body of a self-propelling bacterium at constant velocity v experiences two forces in different directions which have to be equal for the force free condition. The first one is the thrust force $-F_{\mathrm{fl}}$ generated by the flagellar bundle and the second is the viscous drag force of the cell body F_{b} in the opposite direction. The generated torque $-N_{\mathrm{fl}}$ by the bundle counterbalances with the rotational viscous drag of the cell body N_{b}, when it rotates in the opposite direction of the bundle. Using Eqs. 2.7, 2.8, 2.10, and based on these assumptions, we can write the following equations,

$$(A + A_0)v = B\omega, \tag{2.12}$$

$$-Bv + D\omega = D_0\Omega. \tag{2.13}$$

These expressions can be used to experimentally estimate the drag coefficients of the complex helix geometry of the flagellar bundle when a bacterium is fixed in an optical trap and imposed to different flow conditions [43, 51, 53].

2.3.2 Resistive force theory

In this part, it will be explained how an idealized rotating helix can generate propulsive force that is equivalent with giving a theoretical estimation of the coefficients A, B, and D as a function of the geometrical properties of the helical bundle. This theory, for the first time, was presented by Gray and Hancock in 1955 who modeled the swimming of spermatozoa by a wave traveling through the viscous fluid [54, 55]. This model can be applied to a left-handed counter clockwise rotating helix with frequency ω which geometrically is characterized by its length L, radius R, and wavelength λ.

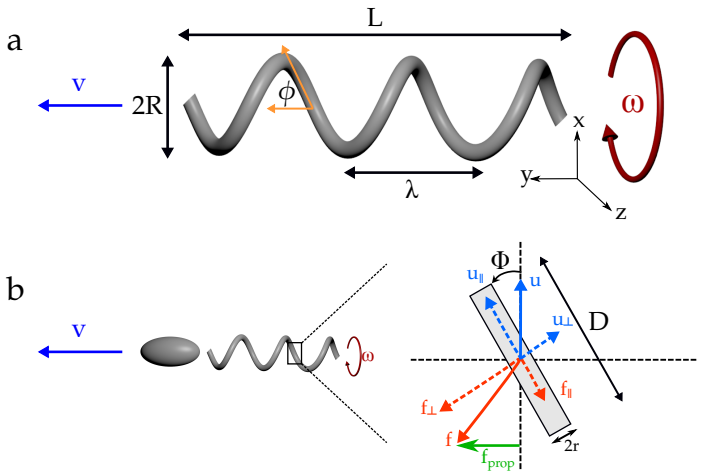

Figure 2.8: Resistive force theory is based on the propulsion by drag. (a) Geometrical properties of the helical filament is schematically depicted. ϕ is the pitch angle of the linear segment with respect to the axial line of the helix. (b) The rotating helix with angular velocity ω can be fragmented into linear cylindrical elements that each one moves with the velocity u perpendicular to the swimming direction. The velocity u can be decomposed into parallel and perpendicular components with respect to the element. Cylindrical element experiences the local drags $f_{\parallel} = -\xi_{\parallel} u_{\parallel}$ and $f_{\perp} = -\xi_{\perp} u_{\perp}$, and due to asymmetric drag ($\xi_{\perp} > \xi_{\parallel}$) a net propulsion force is generated. The total thrust force along the helix can be calculated by summation over the local drag of all individual elements. See the text and [6, 25, 50] for more details.

The helical pitch angle is defined as $\phi = \arctan(2\pi R/\lambda)$ and is shown in Fig. 2.8a along with other parameters of the helix. The helix can be divided into small cylindrical straight elements with radius r and length D larger than r but smaller than λ where r is also the radius of helix filament ($r < D < \lambda$). This theory neglects the long range hydrodynamic interactions between the helix and the cell body and also between the individual elements of the helix. When the helix rotates, the viscous drag force experienced by each element can be decomposed into parallel and perpendicular directions to the cylindrical element. The viscous drag exerted on the element can be written as a linear function of the velocity of an element in the Stokes regime. A typical element of a helix is depicted in Fig. 2.8b and its velocity u is decomposed into components $u_{\parallel}$ and $u_{\perp}$ parallel and perpendicular to the orientation of the cylinder, respectively. The drag force per unit length along the components can be written as $f_{\parallel} = -\xi_{\parallel} u_{\parallel} = -\xi_{\parallel} u \cos\Phi$ and $f_{\perp} = -\xi_{\perp} u_{\perp} = -\xi_{\perp} u \sin\Phi$ where $\xi_{\parallel}$ and $\xi_{\perp}$ represent the drag coefficients of a cylinder when it is pulled parallel or perpendicular to its principal axis through the fluid. The component of this drag force parallel to the axis of the helix and perpendicular to the velocity direction can be obtained by,

$$f_{prop} = (\xi_{\parallel} - \xi_{\perp}) u \sin\Phi \cos\Phi e_y. \tag{2.14}$$

This is the forward thrust force generated by each element of the helix in y direction. The total propulsion force can be obtained by summing the contributions of all elements along the helix (detailed calculations can be found in [56]). There are two sets of tangential and normal drag coefficients commonly used in the literature [57], and both are based on the slender body theory assuming that the effect of small elements are just locally important. Those have been calculated by Gray and Hancock

in 1955 [54],

$$\xi_{\parallel} = \frac{2\pi\eta}{\ln\frac{2D}{r} - \frac{1}{2}}, \tag{2.15}$$

$$\xi_{\perp} = \frac{4\pi\eta}{\ln\frac{2D}{r} + \frac{1}{2}}, \tag{2.16}$$

and more accurate ones that have been suggested by Lighthill in 1975 [58],

$$\xi_{\parallel} = \frac{2\pi\eta}{\ln\frac{0.18D}{r\cos\phi}}, \tag{2.17}$$

$$\xi_{\perp} = \frac{4\pi\eta}{\ln\frac{0.18D}{r\cos\phi} + \frac{1}{2}}. \tag{2.18}$$

There are two fundamental remarks regarding Eq. 2.14 that are essential for propulsion. There is no forward drag for the isotropic element ($\xi_{\parallel} = \xi_{\perp}$), however, in most cases the experienced drag by a cylinder in the perpendicular direction is higher than the parallel direction. Indeed, Gray and Hancock showed that for a very thin cylinder $\xi_{\perp}$ is effectively twice $\xi_{\parallel}$ ($\xi_{\perp}/\xi_{\parallel} \sim 2$) [55, 59]. This property is completely local and declares that with the appropriate geometry and movement, the thrust force can be generated in the direction perpendicular to the movement of element. Additionally, when the helix rotates in a time periodic way, the sign of velocity u changes in opposite sides of the helix and there will be no net propulsive force. Therefore, to generate a net thrust from a periodic movement, both the element velocity u and its orientation angle Φ have to periodically change their sign in time. This means a deformation with given u and Φ following the transformation $u \to -u$ and $\Phi \to \pi - \Phi$ can create a propulsive force with a constant sign while only the periodic transformation $u \to -u$ leads to zero average force. This property is the global condition and states that the periodic movement of the element must be non-reversal in time to generate non zero force on average, which is the expression of the scallop theorem.

Using the local drag coefficients, one can derive the elements of the propulsion matrix by integrating over the helix and obtain them as the following [6],

$$A = \xi_{\perp} L\big(1-\beta^2\big)\left(1+\gamma\frac{\beta^2}{1-\beta^2}\right), \tag{2.19}$$

$$B = \xi_{\perp}\left(\frac{\lambda}{2\pi}\right)\big(1-\beta^2\big)(1-\gamma), \tag{2.20}$$

$$D = \xi_{\perp} L\left(\frac{\lambda}{2\pi}\right)^2\big(1-\beta^2\big)\left(1+\gamma\frac{\beta^2-1}{\beta^2}\right), \tag{2.21}$$

where $\beta = \cos^2\phi$ and γ is the ratio of parallel and perpendicular local drag coefficients ($\gamma = \xi_{\parallel}/\xi_{\perp} < 1$). The angle ϕ stands for the pitch angle of helix as demonstrated in Fig. 2.8. For an isotropic element $\gamma \to 1$ and $B \to 0$ that according to Eq. 2.12 $v \to 0$ and the helix will lose its propulsive property. The helix also cannot generate thrust when $\phi \to 0$ ($\beta \to 1$) or $\phi \to \pi/2$ ($\lambda \to 0$). The details of the derivation of drag coefficients can be found in [56, 58].

2.3.3 Slender body theory

Lighthill modified the drag coefficients and emphasized that RFT can only be used when the body of bacterium can be neglected or is very small [60]. He discussed that

hydrodynamic long range interactions can be ignored if the flagellum generates no additional propulsion. He also argued that collaborative thrust generation by flagellar elements violates the assumption that they do not interact and strongly suggested to apply the more precise calculation of slender body theory (SBT).

Slender body theory is an approximation method which gets the properties of a slender object using the expansions in terms of its slenderness, i.e. the ratio of the width to the length. Lighthill modeled the flagellum by a distribution of point forces, known as stokeslet, dispersed along the centerline of flagellum. He included a distribution of dipole velocity potentials, known as doublets, to satisfy the no slip boundary condition on the flagellar surface. He used dimensionless swimming velocity, torque, and energy to describe the bacterial swimming and obtain self-consistent expressions for the flow field created by the flagellum and the cell body.

Lighthill performed his calculations in three steps: the first step was *zero-thrust limit* where he excluded the cell body and assumed that the helix swims by itself. In this case the helix does not create excess thrust therefore summation of all stokeslets along the swimming direction is zero. In other words, each element of the helix only generates sufficient propulsion to be balanced with its own drag allowing each part to be considered individually as the basic assumption of RFT. In this limit, slender body theory and RFT are equivalent. However, the imposed load to the helix can be balanced by the production of excess propulsion that contains the influence of long range hydrodynamic interactions.

Lighthill included the cell body in the second step. The body experiences a *non-zero thrust* generated by the helix and is pushing forward. The excess load reduces the swimming velocity from zero-thrust value while the frequency of helix rotation is not affected. This is because the load that is imposed by the head will not significantly influence the estimated torque of transverse stokeslets and doublets acting on the helix [56]. It is also assumed that the flow fields produced by the helix and cell body do not interact with each other, which will be corrected in the final step. The drag acting on the ellipsoidal body approximated by a sphere with effective radius a_E in a way that $6\pi\eta a_E = 4\pi\eta b/[\ln(2b/a) - 1/2]$.

In the last step, *long range interactions* between the cell body and the helix were considered additionally. The flow fields created by the cell body and the helix interact with each other and modify the hydrodynamic drags. Consequently, the distribution of stokeslets along the flagellar length is affected and becomes non-uniform. Lighthill used a set of self consistent equations to include the effect of long range interactions and estimate the modified scaled velocity, torque, and energy. SBT is a sophisticated model and its details can be found in [56, 60].

2.4 Theory of random walk

2.4.1 Brownian motion

The erratic movement of a microscopic particle immersed in a fluid is referred to as *Brownian motion*, in honor of Scottish botanist Robert Brown, who observed the continuous random motion of tiny pollen grain under a light microscope [61]. The first conclusive theoretical description was provided by Einstein [62] and Smoluchowski [63] independently using a probabilistic approach. And shortly after, it was rephrased by Langevin [64] in terms of stochastic differential equations. The microscopic reason relies on the rapid collisions of the particles with the solvent molecules that occur at the time scale of the liquid dynamics, typically in order of picoseconds, and at

each incident very small amount of momentum is exchanged [65]. A comprehensive historical review can be found in [66].

Fick studied the inhomogeneous colloidal particles in a suspension in 1855 and concluded that the origin of current is the gradient of density distribution. His observations have been summarized in *Fick's first law* as[52],

$$\mathbf{j}(\mathbf{r}) = -D\nabla n(\mathbf{r}), \tag{2.22}$$

where $\mathbf{j}$ and n are the particle flux and density, respectively. The proportionality constant D is the diffusion coefficient and has the dimension [D]=(length)^2/time. Substituting the Fick's first law into the continuity equation $\partial n/\partial t + \nabla.\mathbf{j} = 0$ will give the *diffusion equation* or *Fick's second law*,

$$\frac{\partial n(\mathbf{r},t)}{\partial t} = D\nabla^2 n(\mathbf{r},t). \tag{2.23}$$

This equation in one dimension can be solved straightforwardly using factorizing ansatz[4]. The general answer in d dimension can be written as,

$$p(\mathbf{r},t) = \frac{n(\mathbf{r},t)}{N} = \frac{e^{-\frac{\mathbf{r}^2}{4Dt}}}{(4\pi Dt)^{d/2}}. \tag{2.24}$$

The solution of diffusion equation is a Gaussian function with the width $\sim \sqrt{Dt}$. The parameter N is the particle number and the quantity $p(\mathbf{r},t)$ can be interpreted as the probability to find a particle in the interval $[\mathbf{r}, \mathbf{r}+d\mathbf{r}]$ because it satisfies normalization condition. One can calculate the *mean square displacement* MSD using the probability density function,

$$\mathrm{MSD}(t) = <\delta\mathbf{r}^2> = 2dDt. \tag{2.25}$$

MSD quantifies how the temporal displacement of a particle evolves from its original position, or physically, how it explores the system. Mean square displacement can be basically a non-linear function of time, MSD $\sim t^\beta$, that in contrast to normal diffusion is known as *anomalous diffusion*. The particle undergoes *subdiffusion* if $0 < \beta < 1$ and it is called *superdiffusion* when $\beta > 1$. The case where the particle moves in a perfect persistent manner $\beta = 2$ which is known as *ballistic motion* [67]. While passive particles experience Brownian motion, microswimmers and self-propeller particles undergo active Brownian motion with a diffusion coefficient larger than an object with the same hydrodynamical size that is called *enhanced diffusion*. The diffusion coefficient is determined by the geometrical shape of passive particle. For a sphere, the coefficient can be obtained using Stokes-Einstein equation,

$$D = \frac{k_\mathrm{B}T}{\gamma} = \frac{k_\mathrm{B}T}{6\pi\eta R}, \tag{2.26}$$

where γ, k_B, T, η, and R are the translational viscous drag, Boltzmann constant, absolute temperature, viscosity, and radius, respectively. In reality, the direction of a particle can also vary apart from the position of its center of mass. This continuous reorientation is called *rotational diffusion*. It happens due to the random kicks of the surrounding molecules of fluid on the particle and can be important for elongated objects [68]. Rotational diffusion is the counterpart of translational diffusion and its

[4] Ansatz is the establishment of the initial equation or value that can be verified later by its results when it is solved.

dimension is the inverse of time and can be calculated as,

$$D_{\mathrm{r}} = \frac{1}{\tau_{\mathrm{r}}} = \frac{k_{\mathrm{B}}T}{8\pi\eta R^3}. \tag{2.27}$$

2.4.2 Bacterial random walk

The simplified movement of active particles such as bacteria can be considered as a random walk consisting of straight segments with the speed $\mathbf{v}(t)$ as running phase. The straight segments are interrupted by instantaneous reorientation events due to tumbling. The reorientations lead to changes in the swimming direction by the angle ϕ generally chosen from a random distribution of turning angles for which one can define the persistence parameter as $\alpha =< \cos\phi >$. The most important assumption is that the duration of each run is independent of the duration of previous run, and consequently, the number of turns in any time interval is governed by Poisson distribution and run time distribution is exponential. Following the arguments of [6, 69] and borrowing a concept from the polymer chemistry, the velocity autocorrelation function can be written as,

$$< \mathbf{v}(t) \cdot \mathbf{v}(0) > = p_0 v^2 + p_1 v^2 \alpha + p_2 v^2 \alpha^2 + \cdots + p_n v^2 \alpha^n + \ldots, \tag{2.28}$$

where p_n is the probability that n turn events happen in time t. The probability to have n turn events within the time t follows Poisson statistics,

$$p_n = \frac{(\lambda t)^n}{n!} e^{-\lambda t}. \tag{2.29}$$

λ is the turning rate or equivalently, the inverse of the average of running time $\tau = \lambda^{-1}$. Inserting p_n in Eq. 2.28 will allow to calculate the summation,

$$< \mathbf{v}(t) \cdot \mathbf{v}(0) > = v^2 e^{-\lambda t(1-\alpha)} = v^2 e^{-t/\tau_{\mathrm{t}}}. \tag{2.30}$$

The correlation time for the straight running path in the presence of tumbling is defined as,

$$\tau_{\mathrm{t}} = \frac{\tau}{1-\alpha}. \tag{2.31}$$

In practice, the path of a swimmer during a run segment is not completely straight but its trajectory orientation is continuously changing due to the process of rotational diffusion. Therefore, the swimmer will lose the direction of its propagation after a certain time even in the absence of sudden turning events. The rotational diffusion can be included in the velocity autocorrelation function by adding a second Poisson process to Eq. 2.28 with a rate $1/\tau_{\mathrm{r}}$. It can be shown that Eq. 2.30 will be consequently modified by an additional factor $e^{-t/\tau_{\mathrm{r}}}$ [70]. The velocity autocorrelation function including the characteristic time scale of rotational diffusion $\tau_{\mathrm{r}} = 1/(d-1)D_{\mathrm{r}}$ can be written as the following,

$$< \mathbf{v}(t) \cdot \mathbf{v}(0) > = v^2 e^{-\left(\lambda(1-\alpha)+(d-1)D_{\mathrm{r}}\right)t} = v^2 e^{-t/\tau_{\mathrm{e}}}. \tag{2.32}$$

The characteristic time scale for a swimmer can be generally considered as a combination of two time scales of turning events and rotational diffusion, $1/\tau_{\mathrm{e}} = 1/\tau_{\mathrm{t}} + 1/\tau_{\mathrm{r}}$, and one can write it as,

$$\frac{1}{\tau_{\mathrm{e}}} = \lambda(1-\alpha) + (d-1)D_{\mathrm{r}}. \tag{2.33}$$

By double integration over $< \mathbf{v}(t).\mathbf{v}(t') >$ one can get an explicit expression for the mean square displacement independent of the dimension of the space [71],

$$< (\mathbf{r}(t) - \mathbf{r}(0)^2) > = 2v^2\tau_e^2\Big(\frac{t}{\tau_e} - 1 + e^{-\frac{t}{\tau_e}}\Big). \tag{2.34}$$

A swimmer moves in a direct way in time scale τ_e before its orientation is lost. This phase of mean square displacement curve is in fact *ballistic regime* and later on the movement of swimmer becomes random and it enters the *diffusive regime*. Eq. 2.34 can describe both phases in the asymptotic case: it will be reduced to MSD $\sim v^2t^2$ for the times very smaller than characteristic time and it can be written as MSD $\sim 2v^2\tau_e t$ in the long time limit. One can get an explicit diffusion coefficient as a function of run time, persistence parameter, and rotational diffusion comparing $2v^2\tau_e t$ with MSD of random walk and inserting the value of τ_e,

$$D = \frac{v^2\tau_e}{d} = \frac{v^2\tau}{d\big(1 - \alpha + (d-1)D_r\tau\big)}. \tag{2.35}$$

However, the diffusion coefficient can be directly calculated by finding the fit parameters to the MSD curve in Eq. 2.34 without dealing with rotational diffusion and run-tumble analysis. Alternatively, it can be determined using Eq. 2.35 and inserting experimental parameters [72].

2.4.3 Langevin equation

In 1908 Langevin introduced the concept of the equation of motion of a random variable and became the founder of the subject of the stochastic differential equation by his formulation [66]. He began by simply rewriting the equation for motion of the Brownian particle based on the Newton's law under the assumption that the particle experiences two forces: (i) a viscous drag $-\gamma\dot{\mathbf{r}}(t)$ due to the dynamical friction experienced by the particle, and (ii) a rapidly fluctuating force $\mathbf{F}(t)$ due to the interaction of the liquid molecules with the particle which is called white noise. This is the residual force applied by the surrounding when the frictional force has been reduced. Therefore, the equation of motion according to Newton's second law for a particle of mass m will be [66],

$$m\frac{d^2\mathbf{r}(t)}{dt^2} = -\gamma\frac{d\mathbf{r}(t)}{dt} + \mathbf{F}(t), \tag{2.36}$$

the friction term is assumed to be governed by Stokes' drag. The fluctuating part $\mathbf{F}(t)$ is independent of position and its temporal average vanishes. It is also assumed that $\mathbf{F}(t)$ varies very rapidly compared to the change of $\mathbf{r}(t)$ which indicates that each collision is instantaneous. This quick change can be demonstrated by

$$< \mathbf{F}(t) \cdot \mathbf{F}(t') > = 2\gamma k_B T\delta(t - t'), \tag{2.37}$$

where $\delta(t)$ is the Dirac delta function and $2\gamma k_B T$ is the spectral density arising from the fluctuation-dissipation theorem. This theorem expresses that the energy lost due to friction and energy gain due to stochastic force should be compensated on average [73]. Langevin multiplied Eq. 2.36 by $\mathbf{r}(t)$ to solve it and get the mean square displacement. He also used the following expressions to simplify the resulting equation further,

$$\dot{\mathbf{r}} \cdot \mathbf{r} = \frac{1}{2}\frac{dr^2}{dt}, \quad \ddot{\mathbf{r}} \cdot \mathbf{r} = \frac{1}{2}\frac{d}{dt}\Big(\frac{dr^2}{dt}\Big) - \dot{r}^2. \tag{2.38}$$

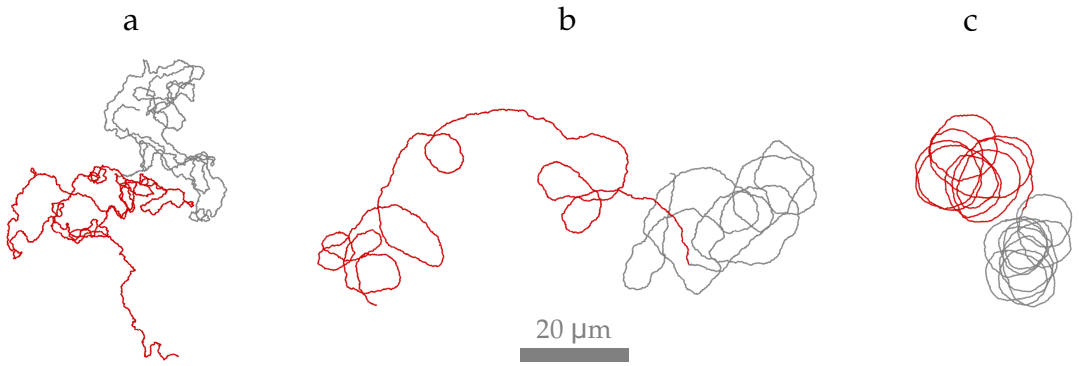

Figure 2.9: Counterbalance between the angular velocity of chiral motion, rotational, and translational diffusion can modify the trajectories in Eqs. 2.44. Sample trajectories of active chiral particles with $\Omega = 5$ rad/s, $v = 30$ μm/s, and radius R for (a) 0.25 μm, (b) 0.5 μm, and (c) 1 μm have been simulated.

He took the average values of the both sides of the equation and the term containing fluctuating force disappeared due to his assumption. The term mr^2 was replaced with dk_BT according to equipartition theorem and the following equation obtained,

$$\frac{m}{2}\frac{d}{dt}\Big(\frac{d<r^2>}{dt}\Big) + \frac{\gamma}{2}\frac{d<r^2>}{dt} = dk_BT. \tag{2.39}$$

This equation can be solved by changing $d<r^2>/dt = u$ and the answer can be written as,

$$\frac{d<r^2>}{dt} = Ce^{-\frac{\gamma}{m}} + 2d\frac{k_BT}{\gamma}, \tag{2.40}$$

where C is the integration constant and can be obtained as $C = -2dk_BT/\gamma$ using the fact $d<r^2>/dt = 2<\dot{\mathbf{r}}\cdot\mathbf{r}>$ and assumption $\mathbf{r}(0) = 0$. The final solution can be found after integration over time,

$$<(\mathbf{r}(t) - \mathbf{r}(0)^2)> = \frac{2dmk_BT}{\gamma^2}\Big(\frac{\gamma}{m}t - 1 + e^{-\frac{\gamma t}{m}}\Big). \tag{2.41}$$

This equation has been also obtained by Uhlenbeck-Ornstein [74] as a theoretical MSD formula for a passive Brownian particle where the time scale is the momentum relaxation time $\tau_e = m/\gamma$ of the particle. Eq. 2.34 is in fact the generalized form of Uhlenbeck-Ornstein equation for the MSD of active particles. One can get the diffusion coefficient $D = k_BT/\gamma$ after comparing Eq. 2.41 with Eq. 2.25 in the long time limit.

The motion of a Brownian particle with coordinate $\mathbf{r}$ and velocity $\mathbf{v}$ can be rewritten as following considering Eq. 2.37 and the Langevin equation,

$$m\frac{d\mathbf{v}(t)}{dt} = -\gamma\mathbf{v}(t) + \sqrt{2\gamma k_BT}\boldsymbol{\xi}(t), \tag{2.42}$$

where the random function $\boldsymbol{\xi}(t)$ is assumed to be a Gaussian white noise with $<\boldsymbol{\xi}(t)>= 0$ and $<\xi_i(t)\xi_j(t')>= \delta_{ij}\delta(t-t')$. The time dependency of $\mathbf{v}$ can be neglected in the overdamped limit where γ is large. It means the velocity $\mathbf{v}$ can be considered as (quasi)stationary in the time scales that $\mathbf{r}$ changes. The Langevin

equation can be transformed into the following form in this limit [73],

$$\boldsymbol{v}(t) = \frac{d\boldsymbol{r}(t)}{dt} = \sqrt{2D}\boldsymbol{\xi}(t). \tag{2.43}$$

Here, the velocity remains constant while the direction can be altered by the noise. In the most general case, one can consider the motion of a self-propeller chiral particle with the velocity v as its direction can be modified by the rotational diffusion D_r or angular velocity Ω due to a torque acting on it. In this condition, the following set of Langevin equations can describe the motion in two dimensions [18, 75],

$$\begin{aligned} \frac{d\phi(t)}{dt} &= \Omega + \sqrt{2D_\mathrm{r}}\xi_\phi, \\ \frac{dx(t)}{dt} &= v\cos\phi(t) + \sqrt{2D}\xi_\mathrm{x}, \\ \frac{dy(t)}{dt} &= v\sin\phi(t) + \sqrt{2D}\xi_\mathrm{y}. \end{aligned} \tag{2.44}$$

One can discretize this set of equations by replacing ξ_i with $\zeta_i/\sqrt{\Delta t}$ where ζ_i is an uncorrelated random number taken from a standard Gaussian distribution with zero mean and standard deviation one [75]. The discretized equations can be used to simulate the motion of active particles as some examples are presented in Fig. 2.9.

2.5 Particle image velocimetry

It is understandable how the observation of moving objects has motivated the first experiments to use simple tools and setups available in nature. A similar experience can be obtained by following the path of a floating piece of wood downstream in the river, although it is restricted to qualitative impressions about the flow. The first promoter of such an experiment was Ludwig Prandtl who designed and employed flow visualization techniques in a water tunnel to study aspects of unsteady flows behind wings. The flow is qualitatively visualized by distributing mica particle suspension on the surface of the water [76]. The quantitative method that has been developed to map entire flow fields instantaneously is called particle image velocimetry (PIV), and it can be used as an ideal tool for biologically important flows due to its nonintrusive character and restricted disturbances [77].

Two dimensional PIV in principle requires a flow seeded with particles and a plane within the flow that is illuminated by means of a laser (light sheet) and imaged using a camera. Successive images are analyzed to find the displacement of groups of particles and consequently vector flow field. Additional parameters can be derived from vector field after post processing [76, 78]. These parts shortly will be explained in the following.

The fluid should be seeded by small buoyant particles to visualize the flow. The typical size of particles for fluid flow applications ranges from 5 to 200 μm depending on the speed of flow and camera magnification. Small particles follow the liquid flows faithfully while larger ones can efficiently scatter light. Therefore, a compromise in most applications has to be found. Seeding is challenging in low speed gas flows due to relatively high density difference [76]. Illumination in PIV setup is usually provided by a narrow sheet of laser light to define the plane of investigation. The small thickness of sheet suppresses blurry imaged particles just below or above the focused plane. While continuously emitting lasers as well as pulsating ones can be used for illumination, pulsating lasers are more appropriate to be used with tiny

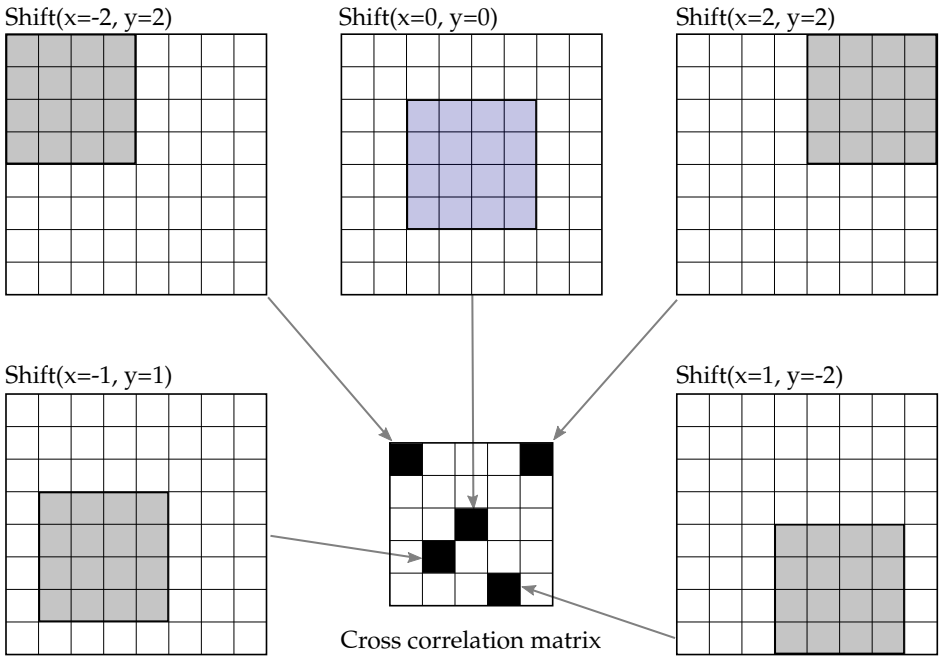

Figure 2.10: Construction of a typical correlation matrix is represented by direct cross correlation (DCC). Images are shifted over each other to find the best pattern match and build the corresponding correlation matrix. The peak position in the correlation matrix shows the displacement. The image has been adopted from [76].

tracer particles because their high power improves their light scattering efficiency. The illuminated plane is imaged by a camera that its optical axis is perpendicular to the plane to record the whole plane in focus. High speed video in combination with a PIV analysis system is called *time resolved PIV*. A high resolution image usually results in a high resolution vector field. However, some analytical methods such as discrete window offsetting [79] and recursive local correlation [80] can compensate the low resolution of the recording system. Interrogation windows or sub-images have to be selected to initiate analyzing a pair of successively recorded PIV images. The velocity vector can be calculated after finding the cross correlation matrix of interrogation windows and their corresponding displacement peak. These procedures should be repeated for all sub-images to obtain the velocity field of whole image. The highest probability for calculating precise correlation function can be achieved when the interrogation window contains 8-10 particles. Standard particle image velocimetry is employed in the case of medium density of particles where the individual images can be detected. However, it is not possible to distinguish image pairs by visually inspecting the recorded sequence. It is not even feasible to identify individual particles in the case of high particle density where they overlap and form speckle. The term for this situation is called *Laser Speckle Velocimetry* (LSV). This term has been used for medium particle density as well as in the beginning of technique development as the evaluation methods were similar in both cases [76]. The cross correlation of window pairs is in principle a statistical pattern matching technique that tries to map the particle pattern between two consecutive interrogation window. This statistical technique is implemented using the discrete cross correlation function [81],

$$R(x,y) = \sum_{i=-K}^{K} \sum_{j=-L}^{L} I(i,j) I'(i+x, j+y). \tag{2.45}$$

I and I' are the intensity values of interrogation windows where I' is larger than I to find all the moving particles in the larger sample. The window I linearly shifted around, in the window I' without extending over its edges, i.e., moving the images over one another to find the best pattern match. The correlation matrix has the size of $(2M + 1) \times (2N + 1)$ after applying this operation for a range of shifts $-M < x < +M$, $-N < y < +N$. The peak in correlation matrix is usually larger than one pixel, and therefore all pixel information of the peak can be used to find the peak location with sub-pixel accuracy using methods such as centroiding, Gaussian, and parabolic curve fitting [78]. The location of the intensity peak shows the most probable displacement. The way that the correlation matrix can be constructed is schematically shown in Fig. 2.10.

Correlation analysis can be performed using Direct Cross Correlation[5] (DCC) or Fast Fourier Transformation (FFT) method. Both approaches have some advantages as well as drawbacks, e.g., FFT needs to have the same format for input sub-images, but it is faster than DCC. The second interrogation window in DCC can be chosen larger than the first one and the result is more reliable than FFT. To compensate the limitations of FFT method, repair routines such as several passes of window offsetting are employed to get a rough estimate of the particle displacement in the first cycle and use it to find the accurate displacement in the second cycle onwards [78, 82]. The neighbor interrogation windows usually overlap to get more velocity information out of the images. The vector field of automated PIV analysis often includes erroneous vectors because of imperfections in the input images mainly due to the local effects. Automated validation methods are usually based on comparing every vector with its neighbors and using statistical or fluid dynamical parameters to differentiate between correct and incorrect vectors. The empty spaces of erroneous vectors are filled by two dimensional interpolation to have continuous local derivatives and gradient parameters.

[5]It is also known as convolution filtering and particle image pattern matching.

3

Single Cell Swimming

Contents

3.1 Literature survey

A peritrichously flagellated bacterium such as *E. coli* undergoes an alternating sequence of active runs and tumbles controlled by the rotational state of each flagellum [83]. It has been recently figured out that the complex dynamics of bundle disruption during tumbling leads to a slow motility phase with a weak propulsion [84]. The run and tumble dynamics of bacteria enable them to modify their direction, and it is known to be highly advantageous to enhance search efficiency and allowing for an optimal navigation towards nutrients or away from unfavorable regions [85].

Boundary element method has been recently used to study the swimming of multi-flagellated bacteria [86]. The authors reported that flagella can lock into a bundle and act as a single helix when they come into close contact and synchronize. This approximately increases the angular velocity of the bundle by 60% while the swimming velocity remains roughly constant. Synchronization time depends on the

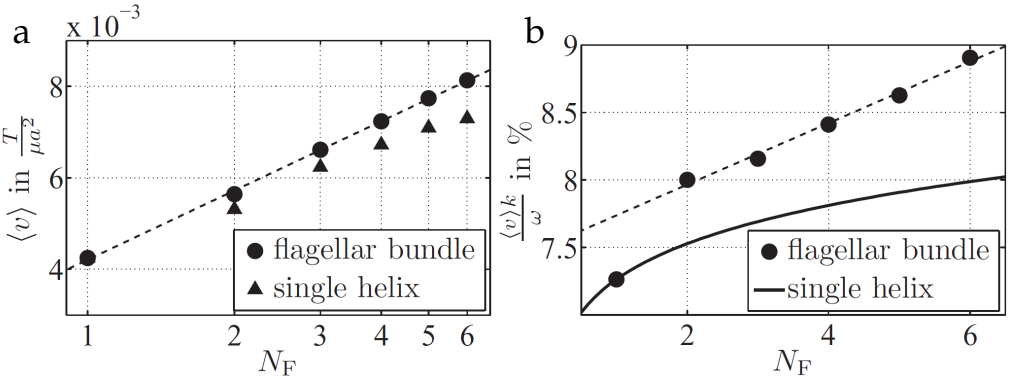

Figure 3.1: Comparing simulation results of a bacterium with flagellar bundle and analytical results of an ellipsoid attached to a single helix with equivalent filament radius. (a) Speed, and (b) efficiency of the flagellar propulsion as a function of number of flagella. Graphs have been taken from [86].

initial phase difference between flagella and takes about one to five flagellum rotation. Bundled flagella propel the cell at a peak velocity with maximum consumption of energy which indicates the flagella are forced to make a bundle by hydrodynamic interaction rather than an attempt to minimize energy consumption. As Reigh et al. numerically concluded [87], these authors described how a multi-flagellated bacterium gains a small advantage in terms of swimming speed in comparison to a bacterium with one single helix as can be seen in Fig. 3.1a. The other interesting parameter that has been reported is the ratio of swimming velocity to the velocity of wave propagating along the helix which is defined as $< v > k/\omega$ and refers to how far a cell moves during one flagellar rotation or the efficiency of flagellar propulsion. This ratio roughly scales linearly with the number of flagella for multi-flagellated bacterium while the simulation yields a lower value for single helix in Fig. 3.1b, i.e., bundled flagella from propulsive perspective is more efficient than a single helix. Bacteria become less efficient with more flagella from an energetic point of view (the energy efficiency is defined as the ratio of energy rate which is used for swimming to the rate at which work is transferred to the fluid). Therefore, energy efficiency is evidently something that bacteria dedicate less priority to rather than motility [86]. It has been shown in [88] that the body rotation is sufficient to wrap the filaments into a bundle even in the absence of the flow field generated by individual flagella. The bundling time in the presence of the body follows the scaling law $t_{\text{bun}} \sim \mu N_{\text{f}}^{-0.5} T^{-1}$ where μ, N_{f}, and T are viscosity, number of flagella, and torque, respectively. The bundling time in the absence of body is proportional with $N_{\text{f}}^{-1.5}$, but in general by considering the prefactors the body rotation gives an advantage in bundling speed. However, the bundle formation can be accelerated by modifying the applied torque rather than changing the number of flagella [86, 87].

Mears et al. mapped the state of single flagellum of *E. coli* to whole cell swimming behavior using an optical trap [89]. Before this study, some theoretical models tried to describe this mapping, e.g., by 'voting' mechanism in which cells tumble only when the majority of flagella rotate CW [17, 90–93]. Turner et al. reported that CW rotation of a single flagellum is sufficient to 'veto' a run by observing fluorescently labeled flagella during individual tumbles [44]. Refined versions of the veto model have been recently developed [94, 95] based on careful slow motion observation of tumbles [43]. As an alternative mechanism for inter-flagellar correlation observed by Terasawa et al. [96], Hu et al. [97] suggested that hydrodynamic interactions between

nearby flagella could also lead to correlation in their rotational direction. According to their model, flagellar switching rates in a cell with single flagellum will be different from than those in multi-flagellated cells, while this prediction does not achieve by Mears and coworkers. They found that the wild type cells with multiple flagella systematically deviate from the prediction of veto model. In the context of veto model, the cells behave in a way that they have smaller number of flagella than what they actually have. Their results suggest that while a single CW rotating flagellum is sufficient to induce tumble, flagella are coupled as well and may switch together in a correlated manner [89]. They used the flagellar number as a fitting parameter for wild type data to formulate a generalized veto model. This model describes the mapping between CW bias (CB[1]) and tumble bias (TB[2]) for wild type and chemotaxis mutant CheY* in which there is no inter-flagellar correlation. Data points from individual cells of both genotypes all collapse on a master curve $1\text{–}TB=(1\text{–}CB)^{N_{\text{eff}}}$ when using $N_{\text{eff}}=1.27\times N_{\text{flag}}^{0.5}$ from fits to the wild type data and actual flagellar number N_{flag} for CheY* cells (Fig. 3 in [89]). Mears in his PhD thesis also studied the relation between the flagellar activity and bacterial swimming [98]. He connected flagellar number to some swimming parameters in the optical trap and indicated that run time, tumble time, body and flagellar rotation rate are not correlated with the number of flagella. His measurements also revealed that there is no correlation between the cell length and body rotation rate while the number of flagella and flagellar rotation rate are positively correlated with the cell length. He performed limited experiments on the swimming cells and reported that the swimming speed decreases in the populations with a lower average number of flagella per cell.

Li used cephalexin to suppress the division of *E. coli* cells and inspect elongated filamentous bacteria [50]. He indicated that the number of flagella per unit length of the body is approximately constant up to 8 μm. However, in contrast to [51], he found that increased cell length reduces swimming speed as well as body and bundle rotation rate (table 5.3 in [50]). He reported the run and tumble duration of two different strains of *B. subtilis* cells in a two dimensional chamber around 1.8 and 0.7 second, respectively. He has also attempted to break the flagella of *B. subtilis* cells and change their flagellar number by two different levels of shearing exerted by syringing. He has found that the swimming speed decreases with increasing the level of shearing.

Turner et al. observed that the average angular change in the swimming direction upon tumbling increases as a function of the number of flagella leaving the bundle [44]. Vladimirov et al. showed when this effect is incorporated into a theoretical model of bacterial chemotaxis, the chemotactic drift is nearly doubled [94]. The classical method of tethering along with inspecting free cells of *E. coli* have been used to measure the torques and forces on the body and bundle in the both cases using resistive force theory [43]. The torque generated by an isolated filament estimated to be ~400 pNnm which was significantly lower than the measures of the motor torque at that time. The generated torque of a flagellar bundle including several filaments is just ~700 pNnm which is surprisingly small. A noticeable fraction of the torque supplied by several motors driving the bundle is dissipated through the internal friction within the bundle or between the bundle and the cell wall, and therefore, additional filaments might not add much to the cell's speed.

Optical tweezers has been also employed to study single cells, measure the force required to hold a bacterium in the optical trap, and determine the propulsion matrix of the body and bundle [51]. It has been found that the body rotation

[1]CB = 1-CCW Bias = 1-the fraction of time that each flagellum spends rotating CCW
[2]TB = 1-Run Bias = 1-time all motors spin CCW/all time

rate decreases whereas the flagellar rotation rate increases as the body elongates. Approximately half of the translational drag on the bacteria is due to the flagellar bundle while the rotational drag of the bundle is very smaller than that of the cell body. The translational drag coefficient is independent of cell size but the rotational drag coefficient of the bundle increases linearly with cell size. The propulsion matrix elements of the bundle strongly depend on the pitch length, e.g., the rotational drag coefficient is proportional with the square of the pitch length. This result implies that the primary size dependence of the rotational drag coefficient is through the pitch length of the bundle. One can accordingly expect a linear growth of the square of pitch length with the cell size. It has been also reported that around 15% of the rotatory power is used to rotate the cell body and just ~1.3% is used to push the cell forward while the rest is dissipated as heat [51].

3.2 Motivation

Many bacteria employ flexible helical flagella to move in their surrounding environment. The flagellar number varies dramatically among species. Studies during the past decades have been mainly devoted to *E. coli* which has up to eight flagella whereas the flagellar number of some bacterial species is typically higher. While only one single flagellum is sufficient to swim in the liquid medium, it is not completely clear why some bacteria synthesize more flagella. Peritrichous cells with several flagella on their surface are more persistent than cells with single flagellum at one pole who can simply swim back and forth. It is assumed that peritrichous bacteria have better chemotactic efficiency [43]. In spite of the progresses in unraveling the mechanism behind bundle formation and disruption [43, 51, 89, 96, 97, 99, 100] and its relation to the chemotactic signaling network [85, 94, 95], it is poorly understood how the number of flagella influences the fundamental properties of bacterial motility such as speed, tumbling, and dispersion. So far, it has been observed that the torque and thus the swimming speed [43] and the fraction of time spent in run or tumble phase [89] of peritrichously flagellated bacteria remain roughly independent of the flagellar number N_{f}. Recent numerical studies also predict that the swimming speed is only slightly affected by N_{f}, assuming that just a single bundle is formed [86, 87]. A fundamental question from an evolutionary point of view is to know which criteria a bacterium adopts to govern its flagellar number. Here, for the first time, we experimentally and numerically study the motility of swimming bacteria over a wide range of flagellar number to clarify how the choice of N_{f} can influence run and tumble dynamics and search efficiency.

3.3 Methods

3.3.1 Cell preparation

The properties of studied strains of *B. subtilis* bacteria can be found in section 2.1.4. Their corresponding number of flagella as the most crucial parameter is summarized in table 3.1.

Table 3.1: Name of the strains with corresponding number of flagella.

Name	ΔswrA	WT	swrA
Number of flagella	9±2	26±6	41±6

The first step of cell preparation for the experiment was streaking 20 μl of the melted cryo-culture on an LB-agar plate that had been made by solidifying an autoclaved solution of premixed LB powder (10 g/l Tryptone, 5 g/l Yeast extract, 5 g/l Nacl, LB Broth L3022, Sigma-Aldrich) and 2% agar in Milli-Q water. The plate was stored in the incubator at 37 °C for one night. Afterwards, it was kept at room temperature and used for about one week. A few colonies of bacteria from the plate were stirred in the LB medium by an inoculation loop and grown in the incubator to prepare an overnight culture. The culture was diluted to OD_{600} ~0.1 in the next morning and grown for two more hours in a Falcon tube to reach the exponential phase in the optical density range of ~0.5 and 0.8. Then, swrA strain was induced by 1 mM IPTG (Isopropyl β-D-thiogalactoside I6758, Sigma-Aldrich) solution to synthesize more flagella as explained in section 2.1.4. The optical density of cells in the exponential phase was adjusted to 0.5 and then diluted approximately 15 folds in the fresh LB medium that had been already purified by 0.4 μm syringe filter. We added 0.005% of PVP-40 (Polyvinylpyrrolidones, Sigma-Aldrich) solution in the suspension of ΔswrA strain before the experiments [101] to prevent cells from sticking to the glass surface. Tracking chambers were the superposition of a cover slip (VWR, 20×20 mm, thickness NO. 1) on a microscope slide (Carl Roth GmbH, Karlsruhe, 76×26 mm) separated by a thin layer of silicone grease (GE Bayer Silicones Baysilone, medium viscosity) as the spacer. The glass surfaces were carefully cleaned by 70% ethanol solution due to the sensitivity of dark field microscopy to stains and dust particles. The height of quasi two dimensional chambers could be adjusted to some extent by applying some pressure to the edges of cover slip and was between 30 and 50 μm. Two lateral sides of the chamber were precisely sealed by silicone grease after filling the cavity with bacterial suspension. *B. subtilis* is an aerobic bacteria, and a reduction of motility is expected in a closed chamber due to oxygen depletion [102–105]. Although we could not realize a significant aging of cells in the closed cavities most of the times, each sample was used for about five minutes after sealing by silicone grease.

3.3.2 Imaging

Dark field microscopy is widely used for imaging of transparent specimens. We exploited a homemade dark field setup using an inverted Nikon Eclipse TE2000-s microscope for tracking of swimming cells. This technique enhances the contrast in the samples that are not imaged well using common bright field microscopy. There is a beam stop before the condenser in dark field illumination that produces a hollow cylinder of light. The condenser directs a cone of light into the specimen at very oblique angles at all azimuths in a way that the first order wavefronts do not directly enter the objective lens. The light passing through the specimen interacts with optical discontinuities (e.g., the border of cell membrane or internal organelles) and enables this faint rays to enter the objective. Therefore, only the scattered light reaches the objective lens and forms a bright image on a black background. The objects out of the focal plane can also have contributions to the image by scattering the light that leads to a reduction of contrast and blurry sample detail. This artifact can be enhanced by the dust and stains in the imaging chamber to contribute to the final image significantly. Furthermore, thin adherent cells usually redirect a very weak signal into the objective, while thick tissues suffer from scattering too much light, reducing the practicality of the technique. It is essential for the objective aperture to be smaller than the inner aperture of the illuminating light (i.e., the shadow of beam stop has to be thoroughly casted over the objective). Nevertheless, objectives with an integrated variable iris diaphragm are able to prevent the indirect light even if it

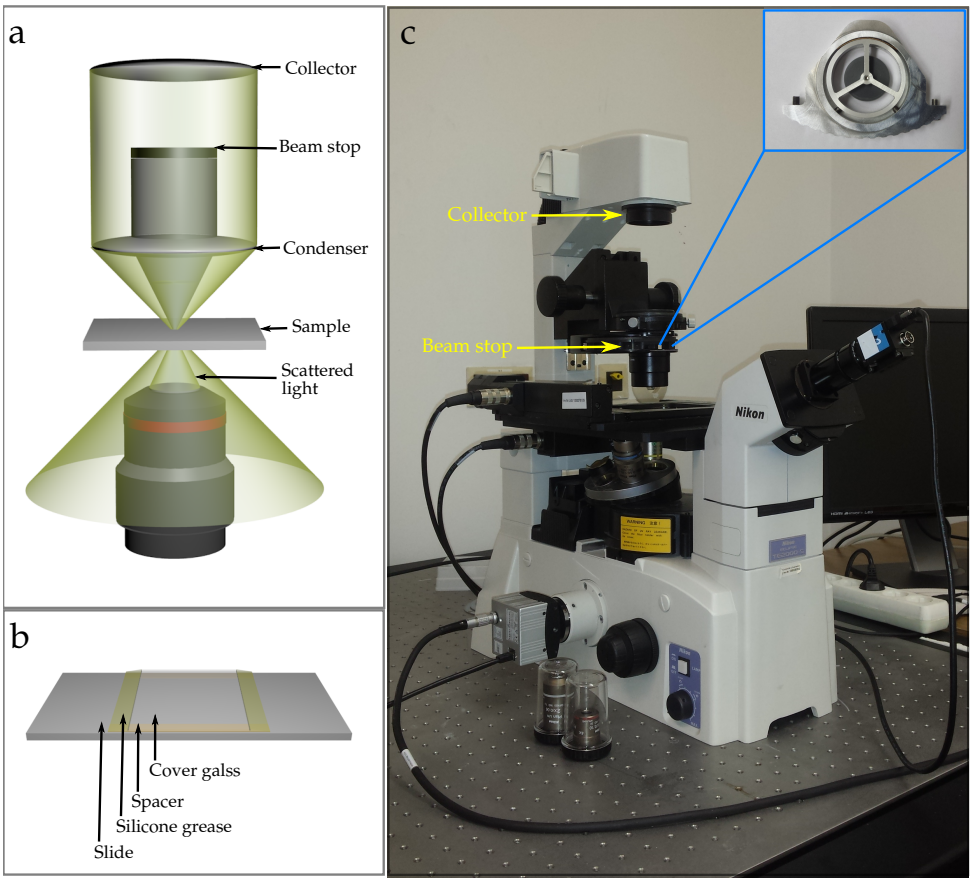

Figure 3.2: (a) Configuration of the dark field illumination. (b) Schematic picture of a typical sample. (c) The beam stop was mounted in the phase ring that is shown in the image. The inset image shows a home-made beam stop which was used in the experiments.

falls into the aperture cone of the objective. These iris diaphragms allow the use of very high aperture lenses for dark field illumination [106]. The arrangement of the dark field illumination components, schematic picture of a sample, and a beam stop is shown in Fig. 3.2. We applied a Nikon 4x, N.A. 0.2 objective to achieve a larger field of view. For each sample, sequences of images were recorded for two minutes with 60 Hz frame rate by a Point Grey FL3-U3-88s2cc CMOS camera. The size of image frame was 2048×1080 pixel and the pixel calibration was 0.77 μm. The experiments were repeated three times by different cultures for each strain.

3.3.3 Tracking

Initial trajectories were extracted by a customized Matlab tracking script after image acquisition. The most basic method for segmentation is setting a threshold after smoothing the image. The magnitude of the first derivative or sign of the second derivative can also be applied for edge finding and bulb detection while both of them enhance the noise level hence need some noise removing filters. The advanced methods like Marr-Hildreth are not only based on the simple filtering but also take into account the image characteristics and other information such as the scaling and noise as well. This can be beneficial since intensity changes along the edge are not independent of the image scale. Sudden intensity change will cause a zero crossing of the second derivative. Marr-Hildreth method combines Gaussian filtering with Laplacian for the edge detection to swipe away the noise from the image, therefore, it is also known as

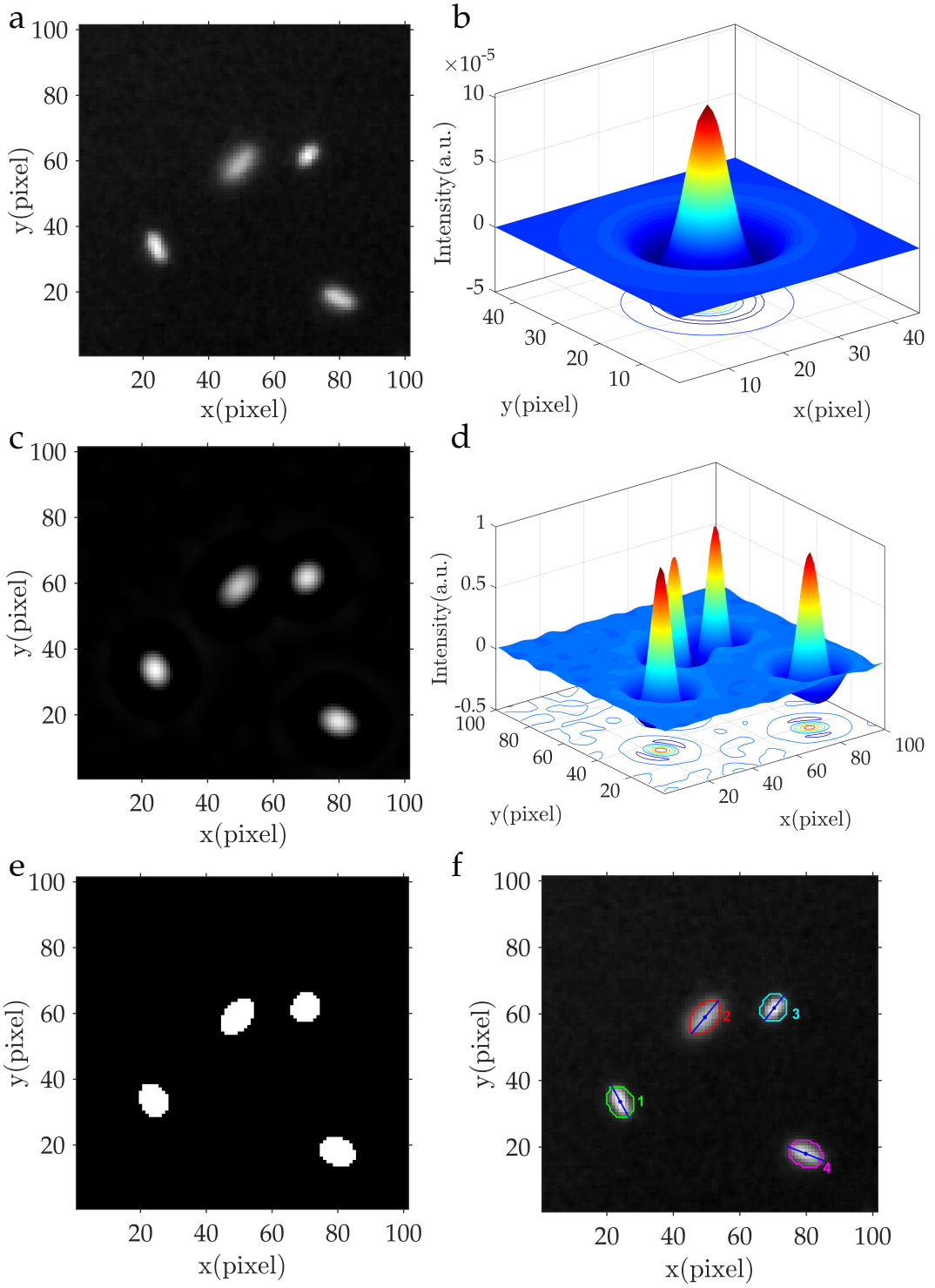

Figure 3.3: Steps that are taken for cell tracking. (a) A raw image of the dark field microscopy. (b) Laplacian of Gaussian (LoG) filter with the width σ=4.3 pixels. (c) The defined filter was applied twice on the image and normalized by dividing by the maximum pixel value. (d) The intensity profile after masking by LoG filter. (e) The binary image after filling the holes. (f) Perimeter and center of mass of the detected regions overlaid on the initial image.

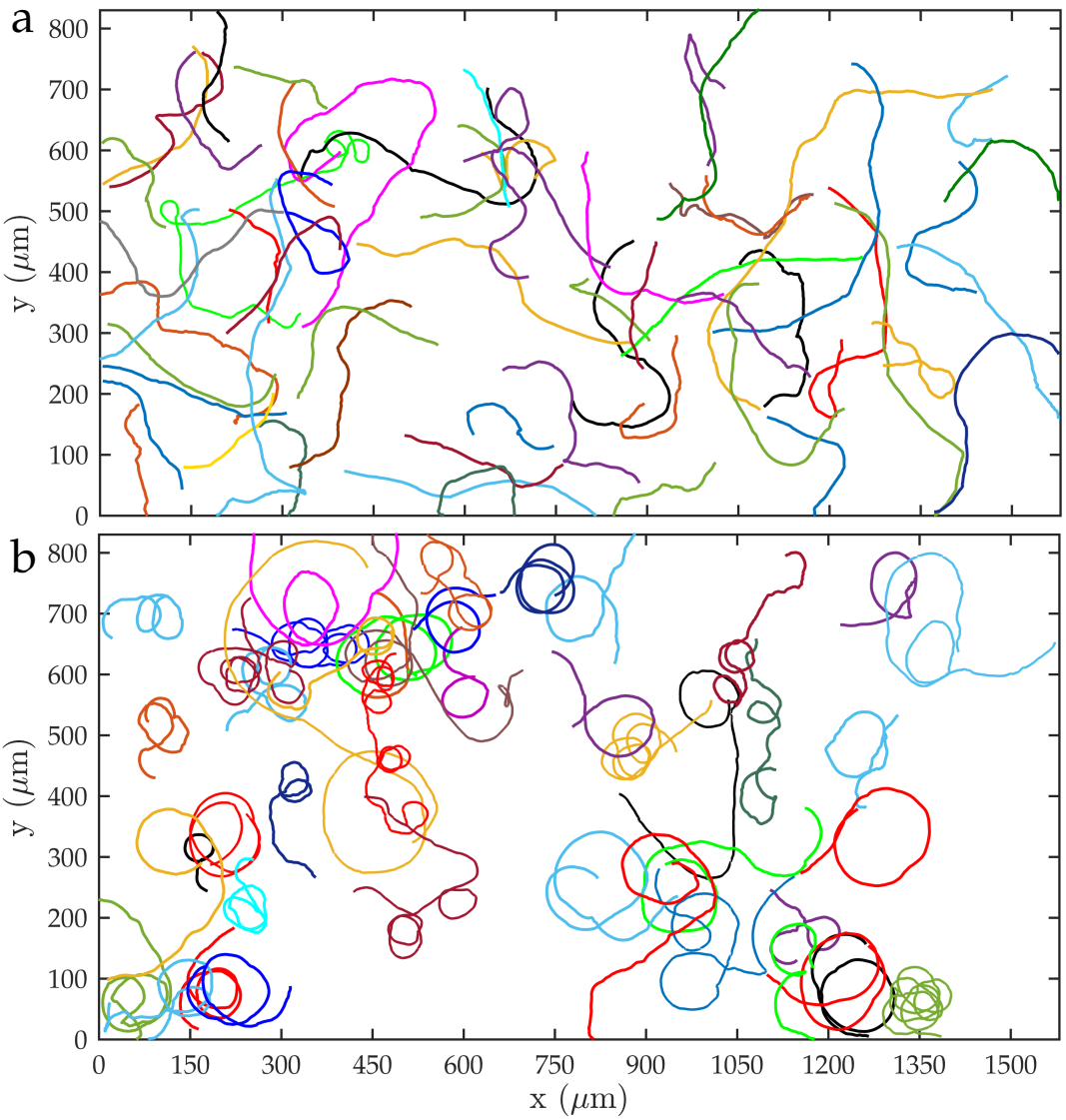

Figure 3.4: (a) Illustrative trajectories of a sample that was used for the run-tumble analysis. (b) Circular trajectories that were excluded from the same sample in (a).

Laplacian of Gaussian (LoG). Since LoG is a linear filter, two constituent filters, i.e., Laplacian and Gaussian can be applied separately [107].

It was realized during preprocessing of the images that using LoG filter twice gives better results. Since the size of Gaussian mask was very small in comparison to the image size, it was computationally faster to apply the mask of double LoG filter on the image instead of twice applying the same filter on the image, i.e., image was masked by $(h*h)*I$ where h was rotationally symmetric Laplacian of Gaussian filter. The standard deviation σ of the Gaussian filter was several pixels that was the order of magnitude of the diameter of bacteria. A raw image of the dark field microscopy is illustrated in Fig. 3.3a. A Gaussian filter with a typical width of σ=4.3 pixels is shown in Fig. 3.3b and applied by a symmetric boundary condition to the raw image. The image was normalized by dividing by the maximum pixel value and converting to the binary image using predefined thresholds. Then, the holes inside the closed peripheries were filled in the binary image, and the properties of isolated regions such as area, eccentricity, major axis length, orientation, and position of the center of mass were determined. The centers of mass of regions in the binary images were determined

based on the location and intensity of pixels. Also, regions with the area smaller than σ^2 or larger than $20\sigma^2$ were discarded in this stage. The bacteria detection procedure step by step is shown in Fig. 3.3. The distance of detected cells in each frame was measured from all cells in the previous frame and the path of closest cells connected to each other. A trajectory was cut off when the displacement of cell exceeded the predefined threshold.

3.3.4 Trajectory analysis

Tracking of cells in a quasi two dimensional chamber leads to the projected trajectories with the specified positions by x and y components in the coordinate system. A moving triangle with a width of 17 points was applied to smooth the data and decrease the noise. Instantaneous velocity of a cell $\mathbf{v}(t)$ at each frame was calculated by discrete derivative of the position vector with the time resolution of 0.0167 second. Instantaneous swimming direction was measured with respect to the x axis using the four-quadrant arctangent of the velocity components. Samples were further analyzed if the distribution of all swimming directions was approximately uniform. The corresponding angular velocity $\omega(t)$ was defined as the rate of changing velocity direction $\theta(t)$ between two consecutive frames. The sequence of subtracted angles was unwrapped to suppress the phase jumps before the calculation of angular velocity.

Several types of trajectories were discarded before statistical analysis which the main ones are as the following. Preliminary experiments revealed that the run duration was in the order of seconds. More noticeably, the cells swam in a very persistent manner. Therefore, it was essential to have temporally long enough trajectories to ensure that they will enter into the diffusive regime. About two thirds of all detected objects had temporal length shorter than 7 seconds and were accordingly removed. The mean speed minus double standard deviation was set as the minimum acceptable speed. Tracks which their displacements were less than minimum speed multiplied by minimum temporal length were discarded to remove the stuck and dead floating cells. The trajectories associated with the cell bodies longer than the mean length of all detected objects plus one standard deviation were ignored as the cells in late exponential phase or chain cells before devision. These cells swam in an abnormal way that leads to large amplitude sinusoidal trajectories in which simple analysis was not feasible. All trajectories were visually inspected after initial selection and extraordinary, circular, and highly curved ones were manually omitted due to the probable interaction with the walls of relatively shallow chamber [108, 109]. Some of the trajectories in one sample that were used for run-tumble analysis or removed due to their circular trajectories are represented in Figs. 3.4a and b, respectively.

The tumble detection algorithms in the literature are all based on the qualitative description that during a tumbling event a drop in the speed $v(t)$ has to be accompanied with an abrupt change in the swimming direction, i.e., a rise in the magnitude of angular velocity $\omega(t)$ [9, 110]. We employed the quantitative criteria of [111] with adopted parameters to distinguish the tumbling events as following. First, all local minima (maxima) of v (ω) in the time series were determined. Each minimum (maximum) is surrounded by two maxima (minima) located at t_1 and t_2. The depth Δv of the minimum or the height $\Delta\omega$ of the maximum can be defined as,

$$\Delta v = \max[v(t_1) - v(t_{\min}), v(t_2) - v(t_{\min})], \tag{3.1}$$

$$\Delta\omega = \max[\omega(t_{\max}) - \omega(t_1), \omega(t_{\max}) - \omega(t_2)]. \tag{3.2}$$

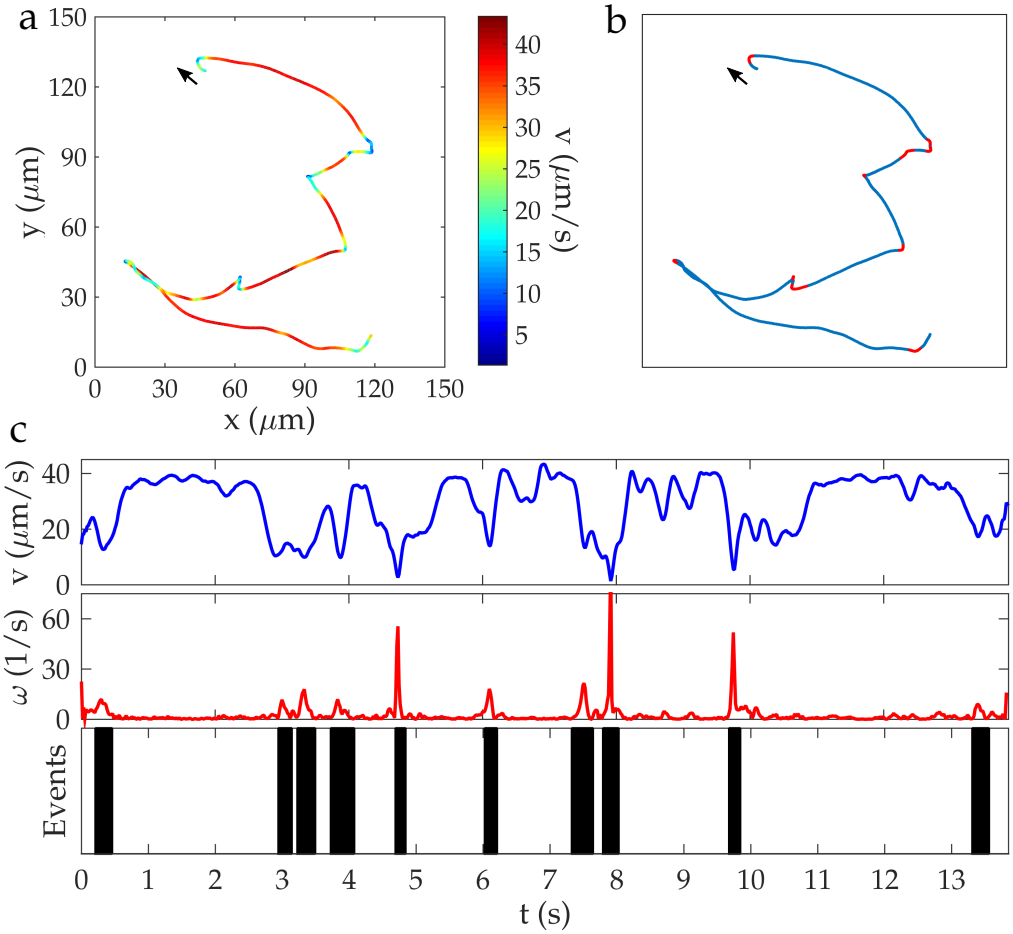

Figure 3.5: Tumble detection algorithm. (a) A sample trajectory with the instantaneous speed as the color code. (b) Detected tumbling events are indicated by the red color. (c) Representation of signal of speed v, magnitude of the angular velocity ω, and detected events.

Two criteria were imposed on the speed and angular velocity to identify tumbling events. If $\Delta v/v(t_{\min})\geq 0.7$, there could be a tumbling event at those times t around $t_{\min}$ where the local velocity $v(t)-v(t_{\min})\leq 0.2\Delta v$. The local maximum of ω might similarly indicate a tumbling event if the total directional change during the time interval t_2-t_1 sufficiently exceeded directional change due to passive rotational diffusion, i.e.,

$$\Sigma|\Delta\theta| \geq 2\sqrt{2D_{\mathrm{r}}(t_2-t_1)}, \tag{3.3}$$

where D_{r}=0.1 rad^2/s is the rotational diffusion of a passive sphere with the radius of one micron. The corresponding tumbling period consisted of those times t around $t_{\max}$ where $\omega(t_{\max})-\omega(t)\leq\Delta\omega$. Imposing both conditions at the same time to find the tumbling events ensures that the reduction of speed is accompanied by a change in the direction of motion. The parameter that has been used to find the minimum (maximum) in the speed (angular velocity) was adjusted in a way to find the most of tumbling events when visually compared with the experimental data. Successive tumblings without any time delay between them were connected to each other. The same parameters were used for all strains. To measure the turning angle after tumbling, for the sake of precision, a line is fitted to four consecutive points of the trajectory before and after the event and the angle between them was considered as the turning angle. A typical trajectory along with corresponding speed and angular velocity signals

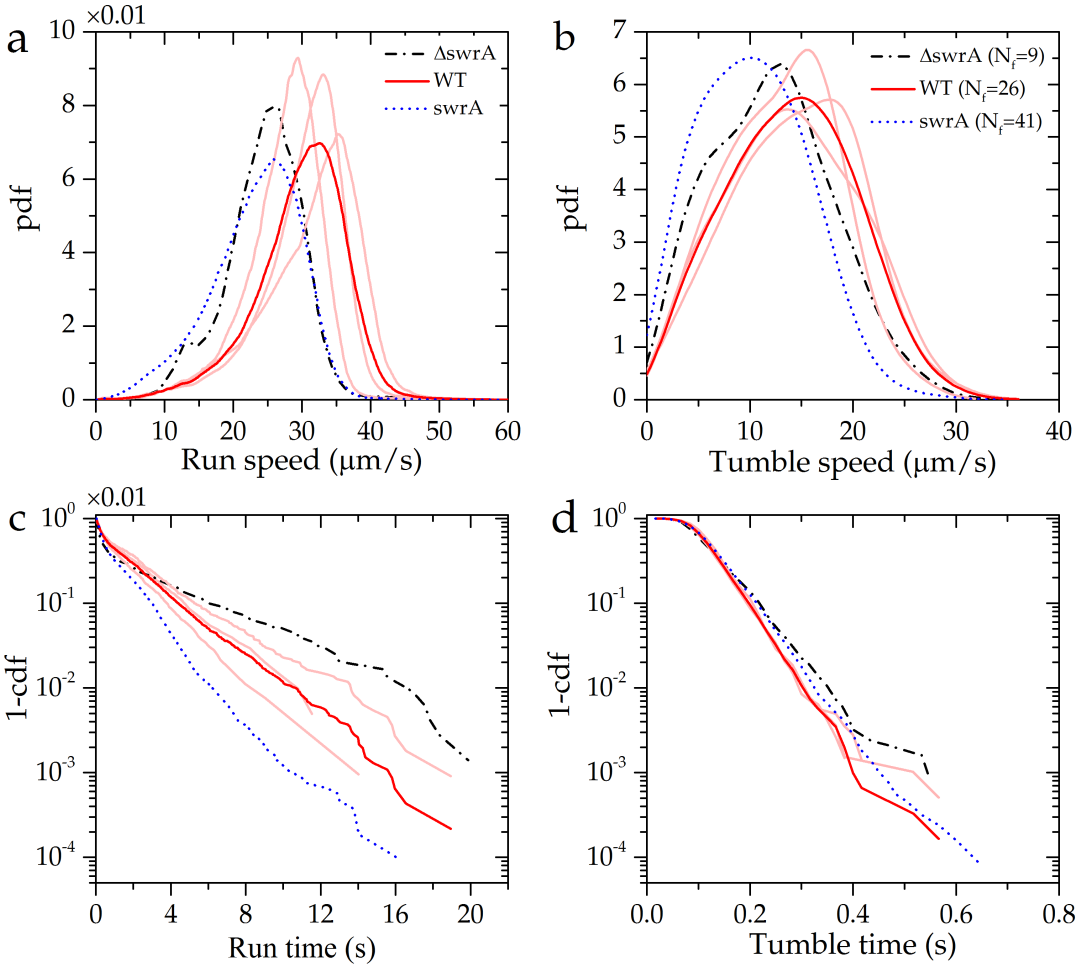

Figure 3.6: (a) The probability distribution of the run speed. The bright red curves represent the distributions for three different cultures of WT strain. (b) The probability distribution of the tumble speed. (c) The probability distribution of observing a complete run time longer than a given duration t where cdf is the cumulative density function. Including the incomplete run segments in the beginning and end of the trajectories enhances the exponential tail of distributions. (d) The probability distribution of observing a tumble time longer than a given duration t.

and detected tumbling intervals are represented in Fig. 3.5.

The flagellar bundle does not usually align with the main axis of the cell body, and consequently, the cell does not swim in the direction of body axis that is known as wobbling. We could not distinguish between the head and tail of the cell body in the dark field images without considering swimming direction. Therefore, to measure the wobbling angle, the angle between the cell body and swimming direction, it was assumed that the absolute value of the wobbling angle is always an acute angle, i.e., bundle always forms at the rear of cell body.

The mean square displacements of the trajectories were calculated using $\Delta r(\tau)^2 = \langle[(r(t+\tau) - r(\tau))^2]\rangle$ where [] and $\langle\rangle$ stand for the time and ensemble average, respectively, and τ is the lag time. Diffusion coefficients were obtained using the discussions that have been introduced in section 2.4.2. The rotational diffusion coefficients were measured by fitting $\Delta\theta(\tau)^2$=$2D_r\tau$ to the rotational mean square displacement RMSD of the run segments of the trajectories where the fit interval was the average run time. One should keep in mind that by considering the running parts, the significant effect of large directional change due to tumbling on D_r is excluded from the

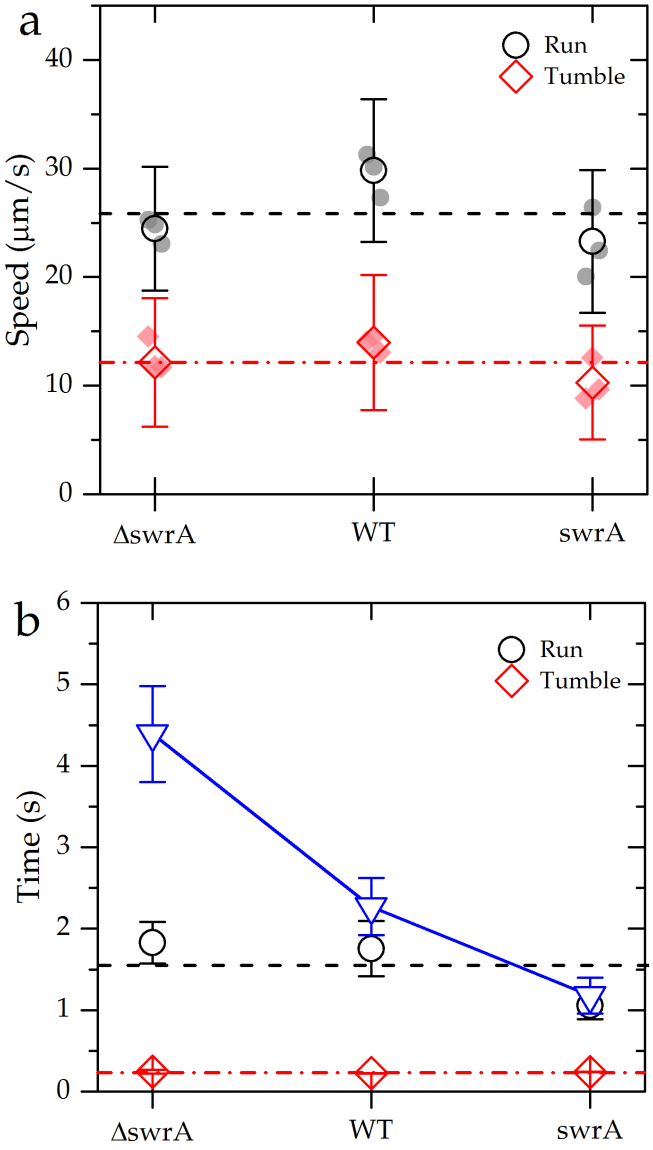

Figure 3.7: (a) The mean run and tumble speed for different strains. Solid symbols indicate the results for different cultures of each strain. (b) The average run and tumble time. Triangles are run time including the incomplete segments in the beginning and end of the trajectories (censored data gives similar results).

results. $\Delta\theta(\tau)^2=\langle[(\theta(t+\tau)-\theta(\tau))^2]\rangle$ is the angular counterpart of MSD where $\theta(t)$ is the velocity direction.

3.4 Results and discussion

3.4.1 Run and tumble

Upon detection of tumbling events, one can measure different quantities for run and tumble segments. According to the results that are shown in Figs. 3.6a and b, the tumble speed is smaller than the run speed but it is not negligible. A closer look at the probability distributions of the instantaneous speeds reveals that even a distribution of a given strain differs from one culture to another due to biological heterogeneity. Speed distributions are not perfect Gaussian functions and are skewed towards faster

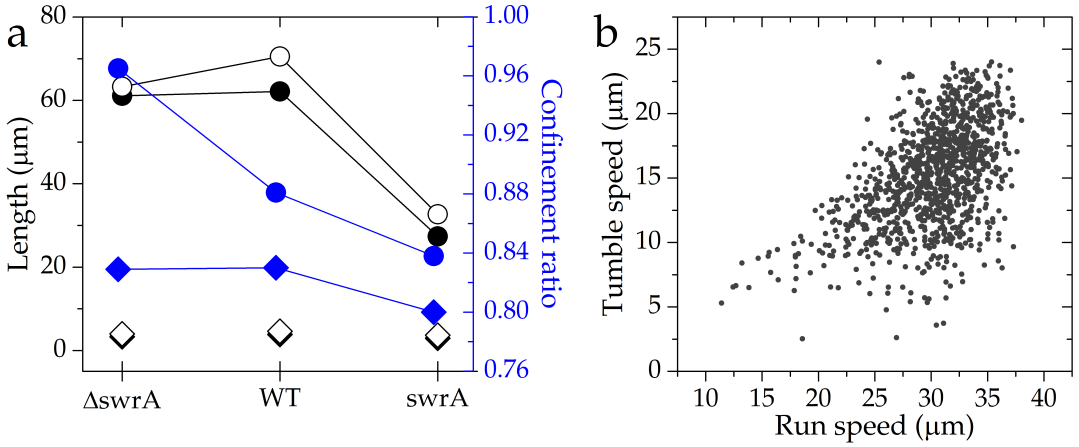

Figure 3.8: (a) Trajectory length in space and confinement ratio during run (tumble) periods are represented by circles (diamonds). Solid and hollow black symbols indicate displacement and total trajectory length, respectively. (b) Tumble speed is correlated with run speed (r=0.5), and it can be approximated as half of the run speed.

(slower) speeds in running (tumbling) phase. The heterogeneity of cultures indeed arises from single cell level and for each cell a 'personality' can be considered, e.g., some cells can perform slow random motion [110]. This type of motion increases the temporal length of the trajectory and consequently leads to a dominant contribution in the speed distribution. There is a weak anti-correlation between the speed and temporal length of trajectory despite the removing of slow swimming cells in initial trajectory selection procedure. By approximating the bundle as a single helix [25, 86], simple models based on the resistive force theory predict a weak (logarithmic) growth of run speed with N_f, though experiments have shown that hydrodynamic dissipation along the cell body considerably reduces the effect [43]. Logarithmic dependency of the speed on N_f arises from the functionality of the helical drag coefficient of helix thickness which is of logarithmic order. The logarithm suggests a limitation of the number of flagella in particular from the energy efficiency point of view [86]. The assumption of single bundle formation does not hold according to our observations of fluorescently labeled flagella as well as several reports in the literature [50, 112, 113]. Multiple bundles can form at the same time during the run phase in which the diversity of their locations and interactions makes the prediction of the propulsive force and swimming speed highly complex. The formation of multiple bundles will be discussed in the next chapter. The tails of the probability distributions of run and tumble time in Fig. 3.6c and d are exponential with a N_f dependent slope. Exponential decays confirm that the switching events between two states of motility happen spontaneously and can be described by Markovian processes.

The average speeds in both run and tumble phases show no systematic dependence on the number of flagella N_f (Fig. 3.7a). The average run and tumble times are plotted in Fig. 3.7b to show whether and to what extent the flagellar number influences the switching frequencies between the run and tumble phases. It appears that the mean tumble time and thus the ability of restoring the run phase is not influenced by N_f. Given the mean tumble time (~0.2 s) and speed (~12 μm/s), one finds that the displacement in the tumbling phase is of the order of the cell length, i.e. a few micrometers (see also Fig. 3.8a). However, such a swimmer with the run speed of ~30 μm/s in an aqueous medium with the viscosity of water is expected to stop after only ~0.6 μs and sliding approximately 0.1 Å if the pushing force suddenly stops [27]. This observation suggests that in contrast to the common belief in the literature the

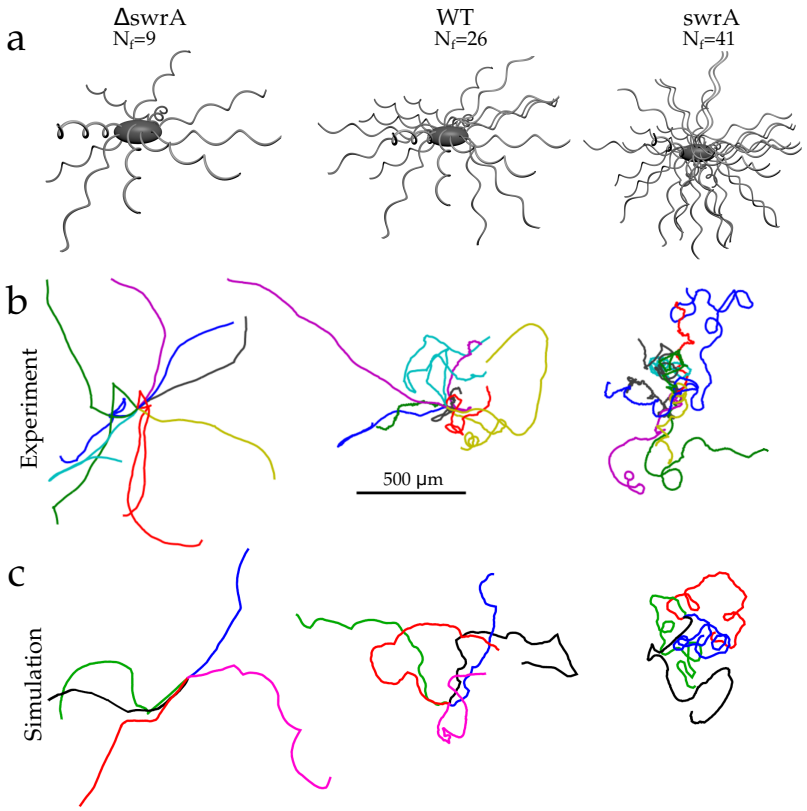

Figure 3.9: (a) Schematic illustration of three strains of *B. subtilis* with different number of flagella. (b) Several projected trajectories of quasi two dimensional experiments are randomly chosen for each strain and their beginning points translated to the same place. (c) Simulated trajectories are obtained using the extracted parameters from the experimental data.

bundles are not fully disrupted in the tumbling phase, thus, the bacterium is partially propelled. The mean run times depend on the flagellar number (censored data of the first and last incomplete periods or directly including them in the statistics amplifies the effect as triangles indicate in Fig. 3.7b). Increasing the flagellar number enhances the probability of switching from running to tumbling. This supports the 'veto' model for bundle disruption [44, 95] which proposes that clockwise rotation of a single or a few flagella less than $N_f/2$ is sufficient to disperse the bundle. Angular velocity ω for both running and tumbling intervals slightly increases with the flagellar number. The average of angular velocity for tumbling is around 4.5 times larger than running. Angular velocity for tumbling segments rises from 5.47 rad/s in ΔswrA strain to 6.65 rad/s in swrA strain.

The tumble speed is highly correlated with the run speed (see Fig. 3.8b) due to the dependence of both speeds on motor speed. It has been recently reported that the tumble speed is ~2/3 of the run speed [84] while our result shows that the tumble speed is around half of the run speed. The tumbling is an active event, not a Brownian motion and its speed is not negligible in contrast to common belief, which suggests it can be included in mathematical models as a non-instantaneous event. The end to end distance (displacement) and the total length of the trajectory during the run and tumble periods are represented in Fig. 3.8a. The so-called confinement ratio $\tilde{l}$ that is defined by dividing the displacement by the total length of the trajectory segment, is also measured [114]. This parameter shows the persistency of the segments. It tends to one for run periods of the cells with a fewer flagellar number indicating their approximate ballistic motion. In fact, the curvatures of the trajectories in

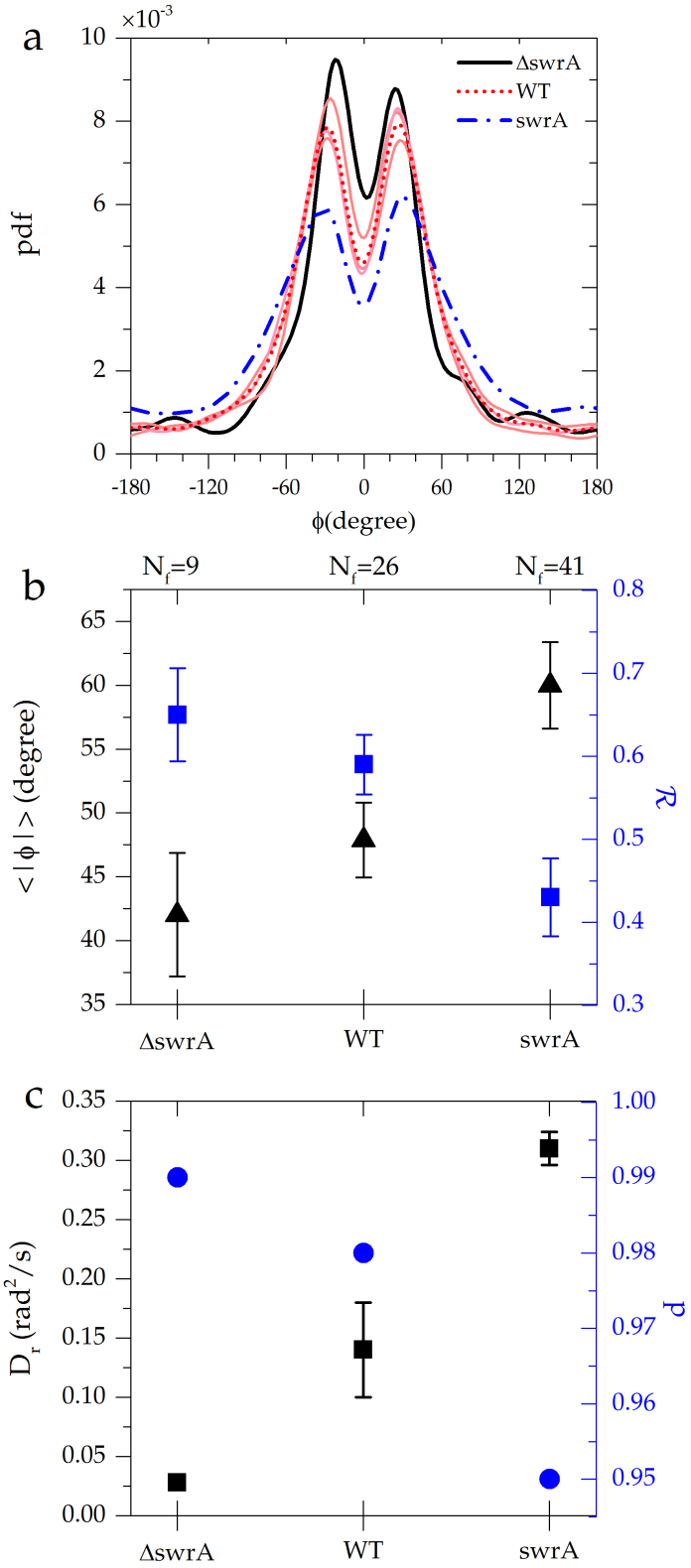

Figure 3.10: (a) The probability density function of the turning angle $R(\phi)$. (b) The average turning angle $< |\phi| >$ and tumbling persistency $\mathcal{R} = < \cos\phi >$ for different strains. (c) The rotational diffusion coefficient D_r and directional persistency of the run phase p.

Fig. 3.9 strongly depend on the flagellar number. The paths are less curved with decreasing N_f which may originate either from the small changes in their direction

due to tumbling or from having a larger persistence length in the run phase. To characterize the running persistency, it is notable that each run trajectory comprises a set of recorded positions of the bacterium and one can extract the local direction of motion. Thus, the directional change θ along the trajectory results in the distribution of directional changes $P(\theta)$. The persistency p of the run phase can be obtained as the Fourier transform of $P(\theta)$, i.e. $p = \int_{-\pi}^{\pi} d\theta e^{i\theta} P(\theta) = < \cos\theta >$ [115, 116]. Alternatively, the curvature of the trajectories can be characterized by calculating the RMSD and rotational diffusion coefficient of the trajectories. Another important parameter of run-tumble dynamics that is affected by the number of flagella is the turning angle between two successive run phases as defined in section 3.3.4. The turning angle distribution $R(\phi)$ in Fig. 3.10a follows left-right symmetry and develops a peak for all strains. However, the peak, and more clearly, the mean of $R(|\phi|)$ shift towards larger angles with increasing N_f as can be seen in Fig. 3.10. Similar to the curvature of run periods, one can use the Fourier transform of $R(\phi)$, i.e. $\mathcal{R} = \int_{-\pi}^{\pi} d\phi e^{i\phi} R(\phi) = < \cos\phi >$, as a measure of directional change between consecutive run phases. $\mathcal{R}$ ranges between

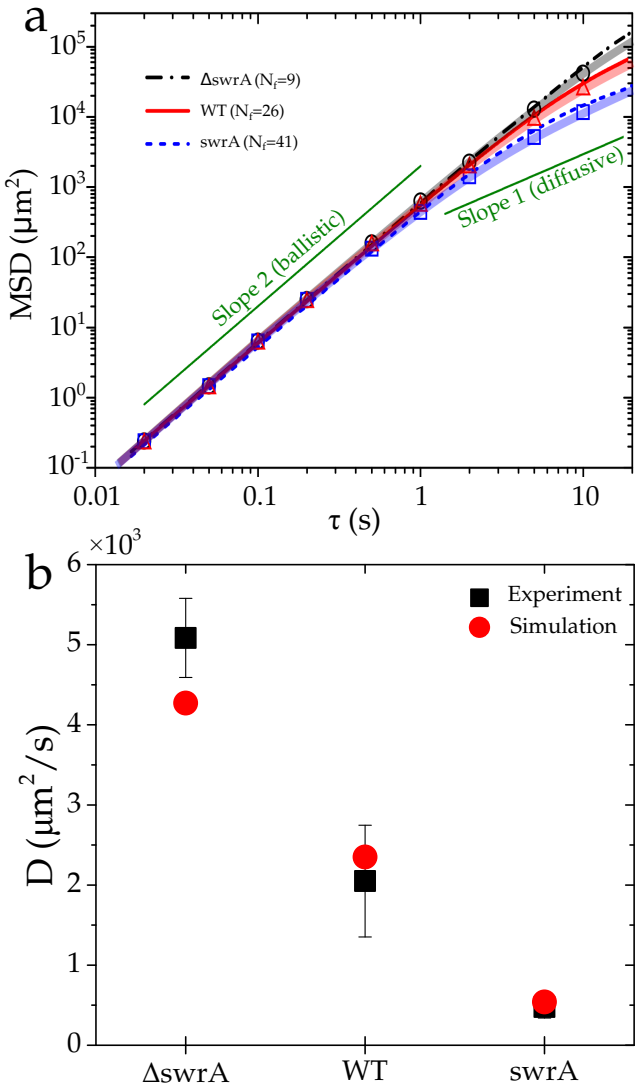

Figure 3.11: (a) Temporal evolution of the mean square displacement for different strains obtained from experiments (thin solid lines), analytical model (thick bright color), and simulations (symbols). (b) The asymptotic diffusion coefficient D for different strains. The analytic predictions (circles) are compared to the experimental results (squares).

-1 and 1, with 1, 0, and -1 denoting 0°, 90°, and 180° turning, respectively. Indeed, $\mathcal{R}$ is correlated with the tumble time and speed [117] as well as the strength of the torque exerted on the cell body during the reformation of the bundle [43]. Since the speed and time in the tumbling phase are not considerably affected by N_f, we attribute the reduction of $\mathcal{R}$ with increasing N_f to experiencing a larger torque during bundle reformation at higher flagellar numbers [43].

The mean square displacement is measured in Fig. 3.11a for different strains. According to our findings, the strains with lower flagellar number have less curved run trajectories, switch less frequently from run to tumble phase, and experience a smaller turning angle between successive run phases. Consequently, the transition from a persistent motion to the asymptotic diffusive dynamics is expected to occur at longer times for smaller flagellar number which is confirmed by the experimental results of the mean square displacement curve. The asymptotic diffusion coefficient D is also a decreasing function of the flagellar number (see Fig. 3.11b). These results indicate that it is more advantageous to have fewer flagella for increasing the long distance transport. The strain with more flagella spends a larger fraction of time in the tumbling state and has a shorter persistence length when swimming. The tumbling events also appear not to be purely random motion and should exhibit a directional persistency. To verify this idea, we calculated the confinement ratio of each tumbling segments of the trajectory $\tilde{l}_{\text{tumble}}$. We found out that the probability density function of $\tilde{l}_{\text{tumble}}$ develops a sharp peak at ~0.9 indicating that most of the tumbling segments of the trajectories are nearly straight during the relatively short periods of tumbling (see Fig. 3.12a).

3.4.2 Fourier z-transform model

Considering the non-negligible tumble speeds, a stochastic coarse grained model for a two-state random walk with spontaneous switchings between two states of motility has been developed by Dr. M. Reza Shaebani. We first confirm the approach by comparing the analytical prediction with experimental results. Then, we use the model and numerically explored phase space of the run and tumble statistical parameters to get

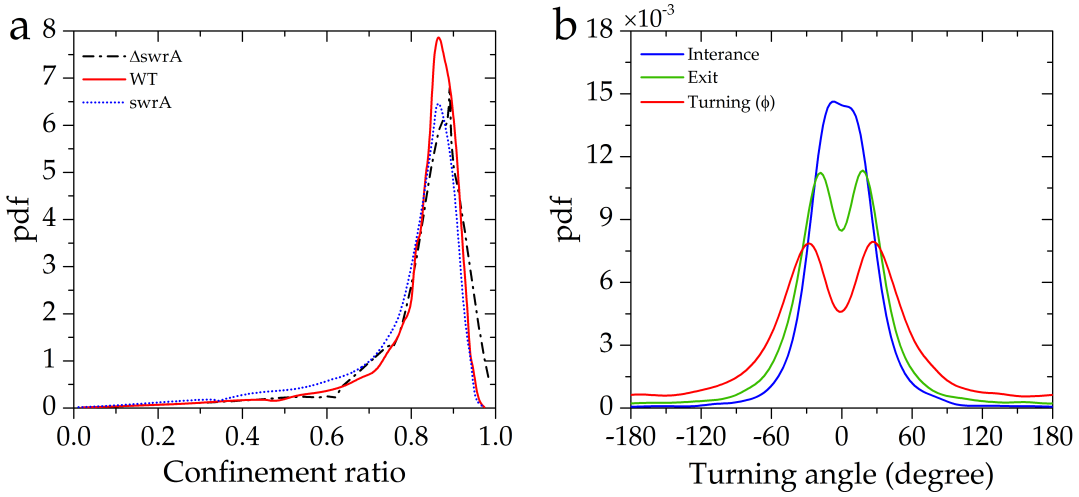

Figure 3.12: (a) Probability distribution of dimensionless confinement ratio for tumbling segments reflecting the bending of segments. (b) The distribution of angles between the run trajectory before (after) tumbling and the straight line connecting the beginning and end of tumble that is nominated as entrance (exit) angle. Turning angle ϕ is the angle between the two run segments. Data shown is for WT strain.

further insight into the impact of flagellar number on bacterial motility. Furthermore, the simulations based on the two-state model reveal a non-monotonic dependence of the mean first passage time on number of flagella.

To obtain an analytical perception by including only the most dominant characteristics of the bacterial motility pattern into the model, we introduce a random walk approach in which the walker experiences two phases of motion: (i) running with the mean speed v_{R} and persistency p, and (ii) tumbling with the mean speed v_{T}. The switching probabilities from run to tumble and vice versa are considered to be asymmetric and denoted by $f_{\mathrm{R}\to\mathrm{T}}$ and $f_{\mathrm{T}\to\mathrm{R}}$, respectively. Assumption of constant switching probabilities leads to exponential distributions for the residence times in each state which is in agreement with experimental observations. In the run phase, a persistent random walk in the continuous space is considered to be characterized by its speed v_{R} and the directional persistency p, quantifying the curvature of the run trajectories. We approximated the tumbling segments as straight lines based on the results of confinement ratio for these periods. According to the experimental observations and with the aim of reduction of parameters, we assumed the tumbling lines are along the last direction of motion in the run phase (see Figs. 3.12b and 3.13a). Therefore, the turning angle ϕ between two successive runs will be equivalent with the angle between the straight line of tumbling and direction of motion in the next run

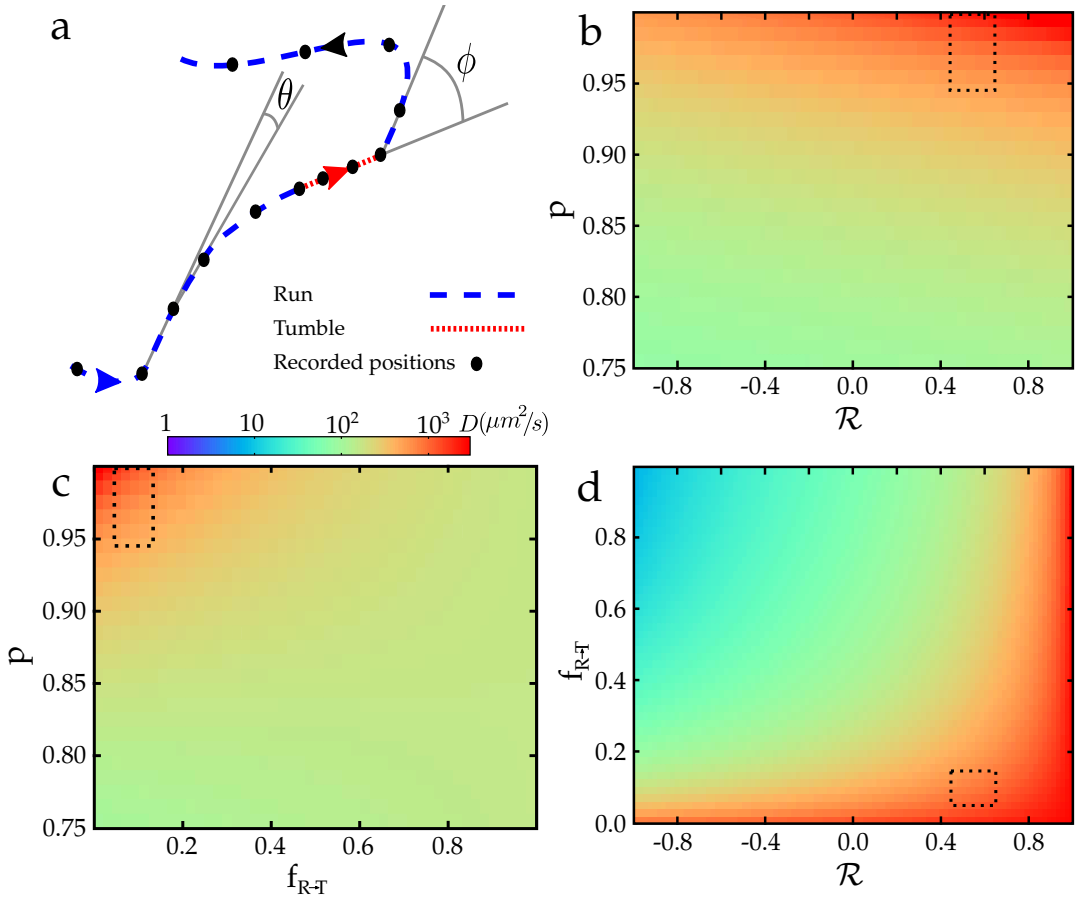

Figure 3.13: (a) A typical sample trajectory of *B. subtilis* with run and tumble dynamics as used in the model. (b-d) The heatmap of asymptotic diffusion coefficient in three dimensional phase space of $\mathcal{R}$, p, and $f_{\mathrm{R}\to\mathrm{T}}$. The cross section of three dimensional phase diagram belongs to (b) $f_{\mathrm{R}\to\mathrm{T}}$=0.05, (c) $\mathcal{R}$= $<\cos\phi>$ =0.56, and (d) p= $<\cos\theta>$= 0.97. The dotted rectangles indicate the accessible range of parameters in the experiments with *B. subtilis*.

and will be used to calculate $\mathcal{R}$ to quantify directional persistency due to tumbling events. Denoting the time steps between two consecutive frames by Δt, we describe the process in discrete time by introducing the probability densities $P_t^{\mathrm{R}}(x, y|\gamma)$ and $P_t^{\mathrm{T}}(x, y|\gamma)$ to find the walker at position (x, y) along the direction γ at time t in the run and tumble phases, respectively. The dynamical evolution is defined by the following set of master equations

$$\begin{aligned} P^{\mathrm{R}}_{t+\Delta t}(x,y|\gamma) &= (1-f_{\mathrm{R}\to\mathrm{T}})\int_{-\pi}^{\pi} d\beta P(\gamma-\beta)P_t^{\mathrm{R}}(x-v_{\mathrm{R}}\Delta t\cos\gamma, y-v_{\mathrm{R}}\Delta t\sin\gamma|\beta) \\ &\quad + f_{\mathrm{T}\to\mathrm{R}}\int_{-\pi}^{\pi} d\beta R(\gamma-\beta)P_t^{\mathrm{T}}(x-v_{\mathrm{R}}\Delta t\cos\gamma, y-v_{\mathrm{R}}\Delta t\sin\gamma|\beta) \\ P^{\mathrm{T}}_{t+\Delta t}(x,y|\gamma) &= (1-f_{\mathrm{T}\to\mathrm{R}})P_t^{\mathrm{T}}(x-v_{\mathrm{T}}\Delta t\cos\gamma, y-v_{\mathrm{T}}\Delta t\sin\gamma|\gamma) \\ &\quad + f_{\mathrm{R}\to\mathrm{T}}P_t^{\mathrm{R}}(x-v_{\mathrm{T}}\Delta t\cos\gamma, y-v_{\mathrm{T}}\Delta t\sin\gamma|\gamma). \end{aligned} \tag{3.4}$$

By the two terms on the right hand side of each equation, we take into account the possibilities of being at each of two states in the previous step. On the right hand side of the second equation, the possibilities of moving along a straight line or switching from running to tumbling are included. By means of Fourier z-transform technique, we obtain exact analytical expression for temporal evolution of arbitrary moments of displacement (see appendix A).

The values extracted from experiments are given in table 3.2 (for the calculation of p we chose Δt=1/6 s). These data have been used as the input of the model and the time evolution of the mean square displacement predicted and plotted for different strains in Fig. 3.11a. We also performed extensive Monte Carlo simulations of a stochastic process with the same parameter values. The model recovers the MSDs of all strains over the whole range of time despite all the simplifications. By introducing $A\equiv 2\frac{f_{\mathrm{R}\to\mathrm{T}}}{f_{\mathrm{T}\to\mathrm{R}}}v_{\mathrm{T}}^2 - f_{\mathrm{T}\to\mathrm{R}}v_{\mathrm{R}}^2$ and $B\equiv 2f_{\mathrm{R}\to\mathrm{T}}^2\mathcal{R}v_{\mathrm{T}}^2 + 2f_{\mathrm{T}\to\mathrm{R}}^2 v_{\mathrm{R}}^2$, we obtain the following expression for the asymptotic diffusion coefficient,

$$D = \frac{1}{4}\frac{\Delta t}{f_{\mathrm{T}\to\mathrm{R}}+f_{\mathrm{R}\to\mathrm{T}}}\left[A + \frac{B + 2f_{\mathrm{T}\to\mathrm{R}}f_{\mathrm{R}\to\mathrm{T}}(1+\mathcal{R})v_{\mathrm{R}}v_{\mathrm{T}}}{f_{\mathrm{T}\to\mathrm{R}}\left[1-p-f_{\mathrm{R}\to\mathrm{T}}(\mathcal{R}-p)\right]}\right]. \tag{3.5}$$

The measured diffusion coefficients for different strains are in good agreement with the analytical predictions. Eq. 3.5 reduces to the asymptotic diffusion coefficient of a single state persistent random walker for $f_{\mathrm{R}\to\mathrm{T}}$=0 and $f_{\mathrm{T}\to\mathrm{R}}$=1 [118].

Table 3.2: Parameter values extracted from experiments.

Strain	$v_{\mathrm{R}}(\mu m/s)$	$v_{\mathrm{T}}(\mu m/s)$	$<t_{\mathrm{R}}(s)>$	$<t_{\mathrm{T}}(s)>$	p	$\mathcal{R}$
ΔswrA	24.5	12.1	4.39	0.244	0.99	0.65
WT	29.8	14.0	2.27	0.224	0.98	0.59
swrA	23.3	10.3	1.18	0.240	0.95	0.43

We can numerically explore the full phase space of the dominant parameters although it is not feasible to systematically adjust the exact flagellar number in experiments. We fixed the speeds v_{R}, v_{T}, and the switching probability $f_{\mathrm{T}\to\mathrm{R}}$ at their average experimental values since they do not vary significantly with N_{f}. This allows us to reduce the degrees of freedom to three important parameters, i.e., the persistency of tumbling $\mathcal{R}$, the directional persistency of run p, and the switching probability $f_{\mathrm{R}\to\mathrm{T}}$. Figs. 3.13b-d show two dimensional profiles of diffusion coefficient in the ($\mathcal{R}$, p, $f_{\mathrm{R}\to\mathrm{T}}$) phase space indicating how diffusion coefficient varies against these parameters. Restricting the parameter values to the accessible range in experiments with *B. subtilis*

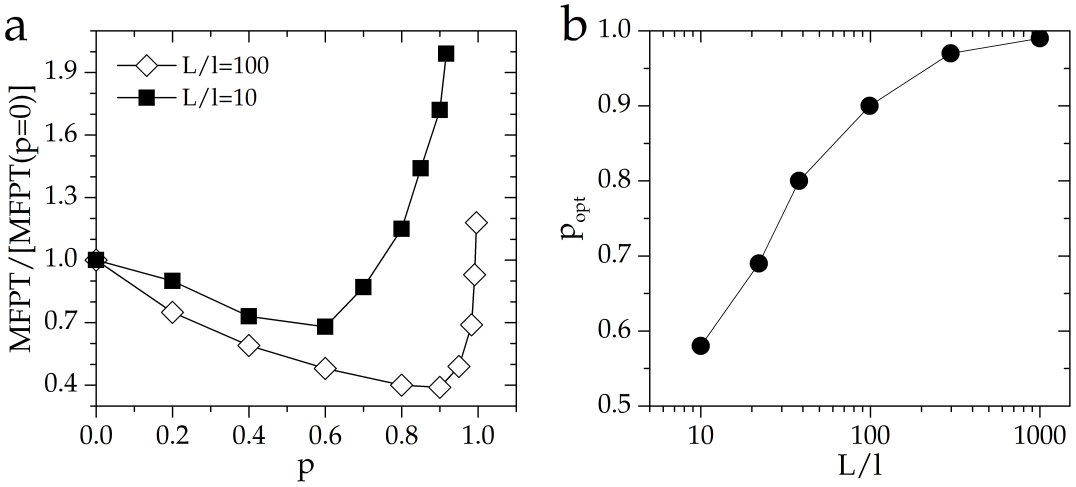

Figure 3.14: (a) Mean first passage time scaled by MFPT at p=0 versus the directional persistency p of the run phase. (b) Optimal persistency p_{opt}, where MFPT drops to a minimum, as a function of the effective system size L/l.

reveals that diffusion coefficient and long distance transport are mainly influenced by the variation of run phase persistency p. By fixing the two other degrees of freedom at their average experimental values and calculating the changes in the asymptotic diffusion coefficient when the third parameter varies within the accessible range in the experiments, we get $D_{\mathrm{max}}/D_{\mathrm{min}}$=1.2, 1.8, and 3.6 for varying $\mathcal{R}$, $f_{\mathrm{R}\to\mathrm{T}}$, and p, respectively.

Search efficiency

We studied the mean first passage time (MFPT) of a two-state persistent random walk in confinement by means of Monte Carlo simulations. The MFPT is defined as the mean time taken by the random walker to reach a particular position in the system for the first time. We simply considered a random walk on a cubic lattice with periodic boundary conditions and all run and tumble parameters except p, as it is the most sensitive factor depending on N_{f}, are fixed at their mean experimental values. The walker is assumed to search for a hidden target during both states of its motility. It appears that the MFPT is a nonmonotonic function of p and has a minimum that depends on cubic lattice size (Fig. 3.14a). One can conclude from the monotonic dependence of p on N_{f} in Fig. 3.10c that the search efficiency is optimized at intermediate values of N_{f}. The efficient persistency grows with increasing L/l in Fig. 3.14b where L indicates the size of the confinement and l is the reaction range of the searcher. Therefore, the optimal number of flagella $N_{\mathrm{f}}^{\mathrm{opt}}$ shifts towards smaller values with increasing effective system size. Experimental measurements revealed that having very few flagella enhances the efficiency of long distance transport and results in fast spreading that is reflected in higher translational diffusion coefficient. Increasing the flagellar number raises the probability of switching from running to tumbling and also decreases the persistency in the run phase. Additionally, switching from tumbling to running is accompanied by a larger directional change for the bacterium with more flagella. Consequently, the overall orientation varies more if there are many flagella. This promotes slow dynamics and can be advantageous for the processes which require localization such as the formation of biofilms. However, the flagellar number of wild type *B. subtilis* is in the middle of the range where the global search efficiency could be optimized according to the simulation results.

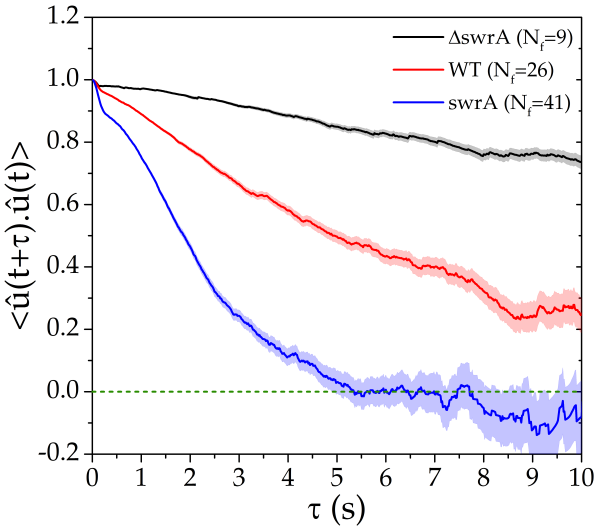

Figure 3.15: Autocorrelation of direction for velocities of different strains in linear scale. Shaded area indicate the standard error of the mean.

Intermittent random walks are known to be beneficial for search efficiency in confined geometries [119–121]. When slow diffusion periods are interrupted by fast migrating ballistic flights, it has been shown that there is an optimal ratio between the excursion times in the two states which results in a global minimum of the search time [119]. The optimal choice depends on the system size and the reaction range of the searcher. Mean first passage time of a single state persistent random walk to find a target also admits a minimum as a function of the persistency [122]. In a general two-state random walk with tumbling and persistent run phases, further complexity arises due to the interplay between the directional persistency p of the run phase, the switching probabilities $f_{\mathrm{R}\to\mathrm{T}}$ and $f_{\mathrm{T}\to\mathrm{R}}$ between run and tumble, the size of the confinement, and the characteristics of the bacterial chemotaxis system (e.g., the reaction range). Nevertheless, the experimental findings reveal that the change of flagellar number of *B. subtilis* influences the dynamics and the search time mainly by affecting the run phase persistency p. If the flagellar number of wild type *B. subtilis* has been evolved to just optimize the search efficiency, simulation results suggest that in the most convenient case they should live in environments with a typical size of the order of few hundreds larger than the reaction radius of the bacterium. The size of such an environment will be less than a millimeter for a reaction radius comparable to the typical size of *B. subtilis* that is a few microns.

3.4.3 Lovely-Dahlquist model

Lovely-Dahlquist introduced a model for the active diffusion of bacteria [69] based on the observations which had been already reported by Howard Berg [9]. Their calculations were summarized in section 2.4.2, and here it will be compared with experimental results. We calculated the autocorrelation in direction in Fig. 3.15 for the run segments using $< \hat{u}(t+\tau).\hat{u}(t) >$ where $\hat{u}$ is the unit vector in the direction of velocity and τ indicates the lag time. Autocorrelation function drops exponentially and the characteristic decay time alternatively represents the inverse of rotational diffusion coefficient. These characteristic times for different strains are in a good agreement with the inverse of rotational diffusion coefficients that have been obtained by RMSD (see Fig. 3.16a). Fitting Eq. 2.34 to the mean square displacement curve gives two parameters. One of them is the speed of motion in the ballistic phase

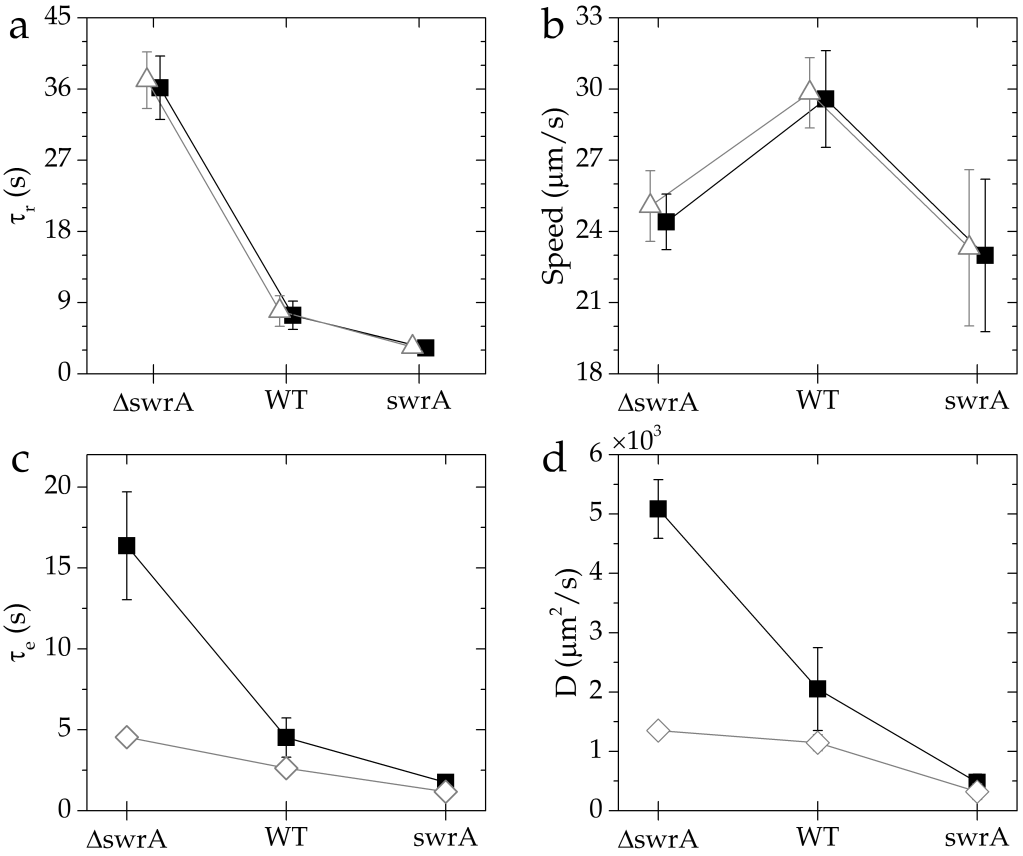

Figure 3.16: Comparison of different parameters obtained by distinct approaches. (a) Inverse of D_r calculated by RMSD (square) and time scale of the exponential fit to autocorrelation of direction (triangle). (b) Directly measured run speed through the experiments (triangle) and the speed of ballistic motion obtained by Eq. 2.34 (square). (c) Effective time scale, and (d) diffusion coefficient measured using MSD curve (square) and by substitution of independent swimming parameters in Lovely-Dahlquist model (diamond).

which is compared with directly measured run speeds through the experiments in Fig. 3.16b. The other one is an effective time scale indicating how long it takes for the swimmer to lose its moving direction. In fact, there are two well known characteristic times in the system: (i) inverse of the rotational diffusion, and (ii) run time that is interrupted by the turning due to tumbling. The effective time scale is $1/\tau_{\text{eff}}=D_r+(1-\mathcal{R})/t_R$ where $\mathcal{R}=<\cos\phi>$ and t_R represents run time. The effective time scale of the combined process was obtained assuming rotational diffusion and tumbling as two independent Poisson processes [69]. The process with longer time scale has the dominant impact on the cell persistency while the one with shorter time can randomize the movement in a better way. Component time scales play an equal role in persistency and randomization when they have the same order of magnitude. The corresponding time scale of the rotational diffusion coefficient of ΔswrA strain is one order of magnitude larger than characteristic time of the run duration, and therefore, cell persistency is mainly due to small rotational diffusion, while tumbling contributes more to randomizing motion. The time scales for the other strains are in the same order of magnitude. The measured effective time scale τ_{eff}, using directly extracted D_r, t_R, and $\mathcal{R}$ from the experiments are lower than the values which obtained by a fit to MSD curve while the trend is the same. As it can be seen in Fig. 3.16c, this underestimation is increasing with the persistency of strains.

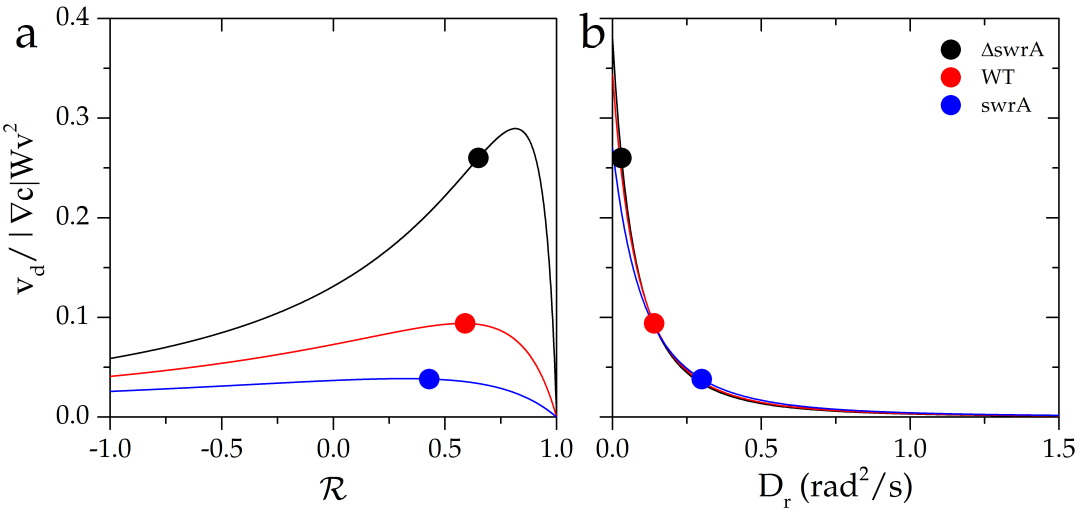

Figure 3.17: Dimensionless drift velocity as a function of (a) persistency of tumbling, and (b) rotational diffusion, assuming equal swimming speed and average run time 1.5 s for all strains.

One of the central assumptions made by Lovely-Dahlquist to combine the time scales by summing their inverse to get the effective time scale was that the component time scales are independent Poisson process, i.e., rotational diffusion and tumbling are uncorrelated. This condition cannot be hold generally because the tumble can be modeled by an active rotational diffusion process characterized by a diffusion coefficient and diffusion time [117]. In a homogeneous medium or shallow gradient, the reorientation of tumbling bacteria is well described by a rotational diffusion process in which the orientation decays exponentially with tumble duration. Therefore, it is possible to consider a rotational diffusion coefficient during tumbles of the order of few rad^2/s to describe this active reorientation process. The diffusion coefficients which were directly calculated by a fit to MSD curve and using Eq. 2.35 are compared in Fig. 3.16d. The diffusion coefficients are also underestimated due to smaller values of effective time scales. The other possible reason that Lovely-Dahlquist model cannot precisely predict the diffusion coefficient is that tumbles have been considered as instantaneous events and excluded from their model. However, our measurements illustrated that tumble speed is nearly half the run speed which suggests that it can have a non-negotiable impact on cell diffusion.

3.4.4 Chemotaxis

A taxis is an inherent behavioral reaction. It is considered as the movement of a cell in response to a stimulus such as chemicals or special frequency of light. Chemotaxis is the movement of an organism in response to a chemical stimulus to direct its movement according to certain chemicals in its environment. This is especially important for bacteria to find nutrients, for example amino acids or glucose, by swimming towards the highest concentration of nutrient molecules or to escape from poisons.

A bacterium is considered which experiences a gradient of chemoattractant with a concentration of c. To direct the rather random run and tumble movement along the gradient, the genetic chemotactic pathway of the cell extends the run times if the cell swims upward the concentration ∇c [9]. Also, it has been recently shown that cells can bias their turning angle towards the high concentration of nutrients [123]. The short response signal of *E. coli* to chemoattractant is measured as a fraction of time that a tethered flagellum to the surface rotates CCW [124]. The response function after

stimulation has an exponential ramp which remains over the baseline for ~1 s, then it falls below and finally approaches the baseline after ~4 s. The following response function $H(t)$ has been introduced inspired by the shape of curve for the fraction of CCW rotation,

$$H(t) = W\lambda e^{-\lambda t}\Big(1 - \frac{\lambda t}{2} - (\frac{\lambda t}{2})^2\Big), \qquad t \geq 0 \tag{3.6}$$

where the constant W is normalization factor and has the dimension of volume [125–127]. This response function has been used to linearly connect the biased tumbling frequency $\lambda(t)$ of a bacterium to the concentration of chemicals that it feels along its path,

$$\lambda(t) = \lambda\bigg(1 - \int_{-\infty}^{t} dt' c(t') H(t - t')\bigg), \tag{3.7}$$

where λ is the tumbling frequency in a homogeneous medium. The chemotactic drift velocity of bacteria in the presence of small gradient $|\nabla c|$ is defined as $\mathbf{v}_\mathrm{d} = \lim_{t\to\infty} < \mathbf{r}(t) - \mathbf{r}(0) > /t$. The hydrodynamic limit provides expressions for the chemotactic sensitivity χ=$v_\mathrm{d}/|\nabla c|$ and bacterial diffusivity D. Using the response function from Eq. 3.6, the drift velocity can be written as the following [127],

$$v_\mathrm{d} = |\nabla c| W v^2 \frac{\lambda^2[\lambda(5 - 2\mathcal{R}) + 4D_\mathrm{r}](1 - \mathcal{R})}{6[2D_\mathrm{r} + \lambda(1 - \mathcal{R})][2D_\mathrm{r} + \lambda(2 - \mathcal{R})]^3}. \tag{3.8}$$

We aim to briefly compare the impact of turning angle and rotational diffusion on chemotactic efficiency and get some insights into biased swimming using analytical predictions. To this end, the dimensionless quantity $v_\mathrm{d}/|\nabla c| W v^2$ is plotted in Fig. 3.17 as a function of $\mathcal{R}$ and D_r assuming the same speed and average run time of 1.5 s for all strains. Circular symbols indicate dimensionless v_d that has been obtained by substitution of experimental values in Eq. 3.8. Fig. 3.17a represents the dimensionless drift velocity for different strains with corresponding rotational diffusion coefficients. The curve for ΔswrA strain with a few flagella for a specific $\mathcal{R}$ is always above the other curves independent of the value one chooses for the persistence parameter $\mathcal{R}$. Therefore, the strain with a lower flagellar number has better chemotactic efficiency if we assume that all strains experience similar changes in the run time and turning angle around their current value when there is a chemical gradient. The drift velocity for the strain ΔswrA can rise up to a maximum value since chemotaxis leads to more persistence movement [123]. The interesting point about Fig. 3.17a is the peak in drift velocity which is more pronounced for ΔswrA strain at $\mathcal{R}$~0.8. The drift velocity suddenly drops after the sharp peak that indicates bacteria with high run persistency and small turning angle cannot effectively adjust their swimming direction. The strain with a few flagella can maximize its drift velocity with a slight variation of turning angle. Dimensionless drift velocity as a function of rotational diffusion coefficient is shown in Fig. 3.17b for the strains with different persistence parameter $\mathcal{R}$. The curves approximately coincide on each other that implies the variation of turning angle in the experiments cannot significantly influence the drift velocity.

It is already known in the presence of chemicals individual bacteria can vary their run time [9] and turning angle [123], while the impact of rotational diffusion and its relevance to the flagellar number have not been analytically and experimentally discussed in the literature. The increased distance between the curves in Fig. 3.17a and the abrupt rise in the drift velocity with decreasing rotational diffusion in Fig. 3.17b suggest that bacteria can more effectively regulate their chemotactic efficiency by modifying the persistency during the run phase. In this respect, ΔswrA strain can have the best response to chemical gradients if all strains similarly adjust their swimming

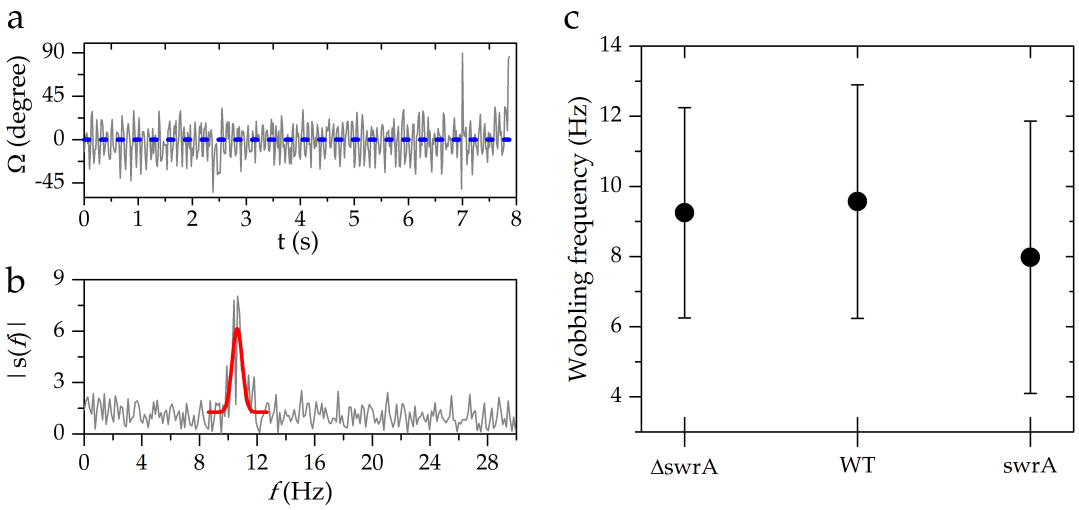

Figure 3.18: (a) Exemplary temporal signal of the projected wobbling angle on the observation plane that oscillates around zero corresponding to the velocity direction. (b) Amplitude of the fast Fourier transformation of the signal in (a) and Gaussian fit around the global peak. (c) Average wobbling angle for different strains with the standard deviation as the error bar.

parameters. This can not necessarily be the case due to the reports showing that involving more flagella in tumble can enlarge the turning angle [43, 94] which leads to higher drift velocity. Thus, it seems that along with modification of run time and turning angle, the variation of rotational diffusion can also be an efficient way of increasing chemotactic performance of individual cells. We note that the discussed search in section 3.4.2 which was efficient for the intermediate number of flagella in a special system size of the homogeneous environment is termed 'exploring', where the bacteria are looking for nutrient resources [72]. It is also known as 'blind' or 'uniform' search (see section 3.4.2). Bacteria need to effectively survey both short and large distances to have an optimum search efficiency. Chemotaxis is 'exploiting', i.e., bacteria can sense where the nutrients are and aim to reach them by biasing their movement towards the resources. In this sense, it is more beneficial to swim persistently as we discussed in the case of strain with a few flagella.

3.4.5 Wobbling

The bundle of a swimming bacterium is not usually aligned with the orientation of the cell body. The body spins around the bundle axis, parallel to the velocity direction, to keep the torque free condition. Thus, the projection of the cell body on the observation plane oscillates around the velocity vector. The angle between the cell body and velocity vector is called *wobbling angle*. The time evolution of wobbling angle $\Omega(t)$ for run phases can be measured for each cell. Run phase is typically short due to the exponential distribution of run time. Sampling rate of the recorded images was 60 Hz and consequently Nyquist frequency will be 30 Hz. This allows us to estimate the wobbling frequency by the amplitude of fast Fourier transformation (FFT) of wobbling angle. To this end, only the long trajectories were used that tumble detection algorithm could not find any event along them. The total numbers of these smooth swimming cells for ΔswrA, WT, and swrA strain were 643, 307, and 175, respectively. A Gaussian function was fitted to the highest peak of the spectrum of each trajectory to find the corresponding frequency precisely. The size of fit interval in the vicinity of peak was selected based on the temporal length of trajectory and its minimum length

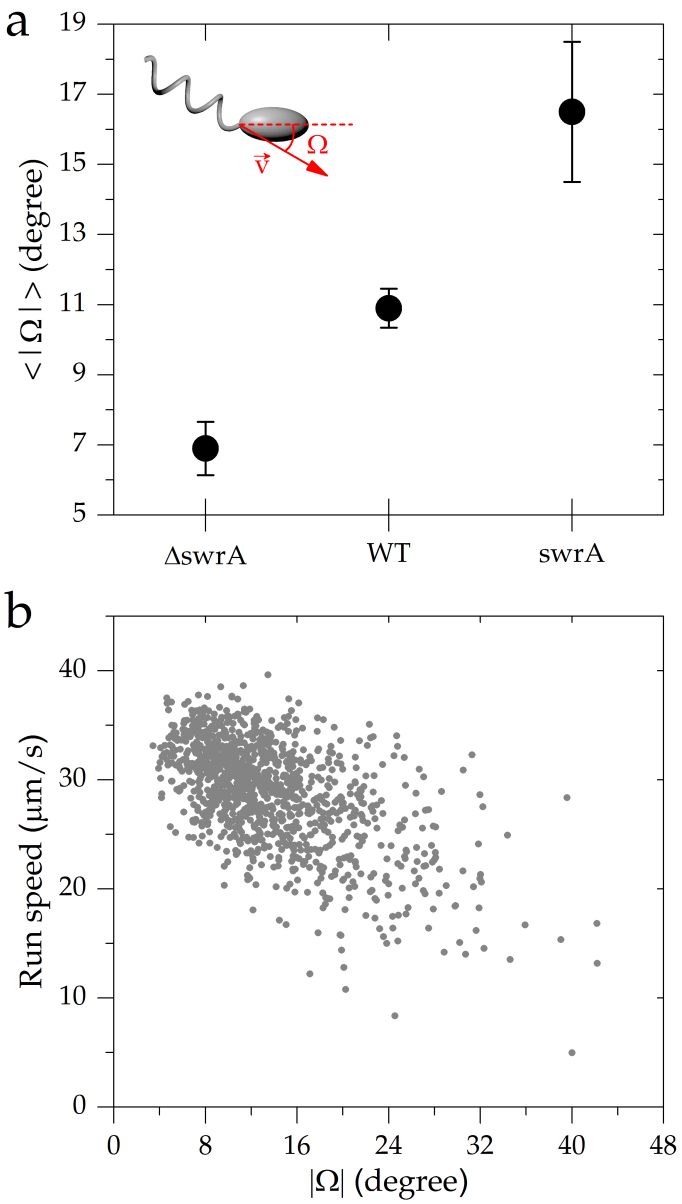

Figure 3.19: (a) The average of absolute wobbling angle increases with the number of flagella (the inset image schematically shows wobbling angle). (b) The run speed anti-correlated with the absolute value of wobbling angle for all strains. Illustrative data belongs to the wild type strain.

was 28 points. Signals with peaks near the borders were rejected because there were not enough points to fit a Gaussian function. The oscillation of wobbling angle of a wild type cell and its corresponding fast Fourier transformation amplitude are shown in Figs. 3.18a and 3.18b, respectively. The average wobbling frequency for ΔswrA and WT strain is ~9 Hz while for swrA strain is ~8 Hz (Fig. 3.18c). The FFT amplitude of several signals lacked a dominant peak that together with the heterogeneity of cells reduce the precision of measurements. However, there is no significant difference in the range of standard deviations as error bars. The wobbling frequency is in the range of reported values for *B. subtilis* [128] and *E. coli* [98].

The average wobbling angle increases with the number of flagella which originates from the distinct geometrical arrangement of bundles in different strains (Fig. 3.19a). The bundle properties will be discussed in the next chapter that is dedicated to the

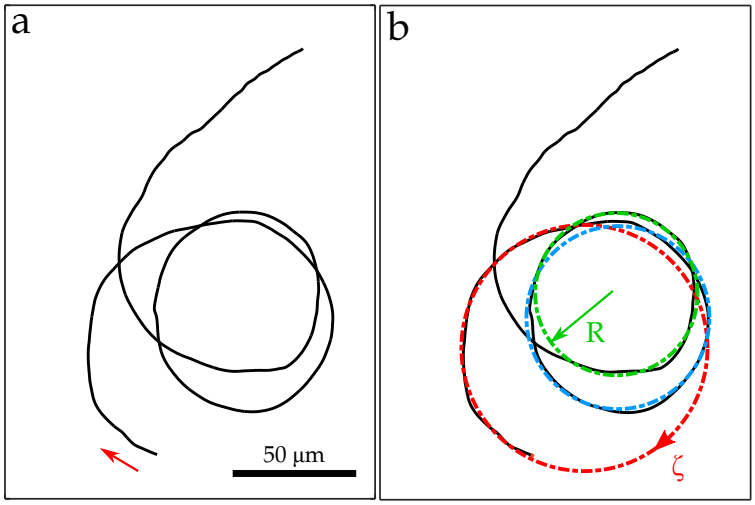

Figure 3.20: (a) Illustration of a clockwise circular trajectory. (b) Some representative fitted circles to the trajectory are demonstrated. The angular velocity of the circular motion is shown by ξ.

fluorescent staining of flagella. The wobbling angle of ΔswrA strain is on average ~7° and increases to ~17° in swrA strain that is in the range of reported value for *E. coli* cells [129]. Furthermore, the cells with larger average wobbling angle swim slower during the run phase as it can be seen in Fig. 3.19b. The frictional drag coefficient for a prolate (oblate) ellipsoid moving in random directions can be calculated by $1/f=1/f_1+1/f_2+1/f_3$ where f_i refers to the drag coefficient along the principal axis [52, 130, 131]. The average drag coefficient for an ellipsoid can be easily obtained as $f=6\pi\eta b/\ln(2b/a)$ where a and b are the minor and major axis of the ellipsoid (see section 2.3.1). The cell body sweeps a cone with a fixed apex angle around the velocity direction as central axis in three dimensions despite the oscillation of projected wobbling angle. It is energetically beneficial for cells to reduce the apex angle of the cone and consequently friction during the run phase. The average wobbling angle of each cell does not normally exceed an upper limit thus the body orientation is not completely random. However, there are some population of cells possessing larger wobbling angle and slower swimming speed. The drag coefficient in transversal direction is larger than longitudinal direction for a prolate ellipsoid with the aspect ratio larger than ~2.24 that is satisfied in *B. subtilis* cells. Therefore, the drag coefficient will be inversely proportional to speed considering the equal propulsion force and nearly constant swimming speed (sections 2.3.1 and 2.3.2). This argument at least qualitatively justifies the anti-correlation between the wobbling angle and run speed. In practice, the bundle has dominant contribution in the translational drag, and propulsion force can also be different between the strains.

3.4.6 Swimming in a circle

Swimming in the vicinity of a surface has several consequences including circular trajectories [132], trapping, accumulation of cells [101, 133], and increasing run time [110]. We excluded circular and highly curved tracks after visual inspection of all trajectories to get rid of surface effects (Fig. 3.4b). Here, we aim to quantitatively study these trajectories. An exemplary circular trajectory together with fitted circles is shown in Fig. 3.20.

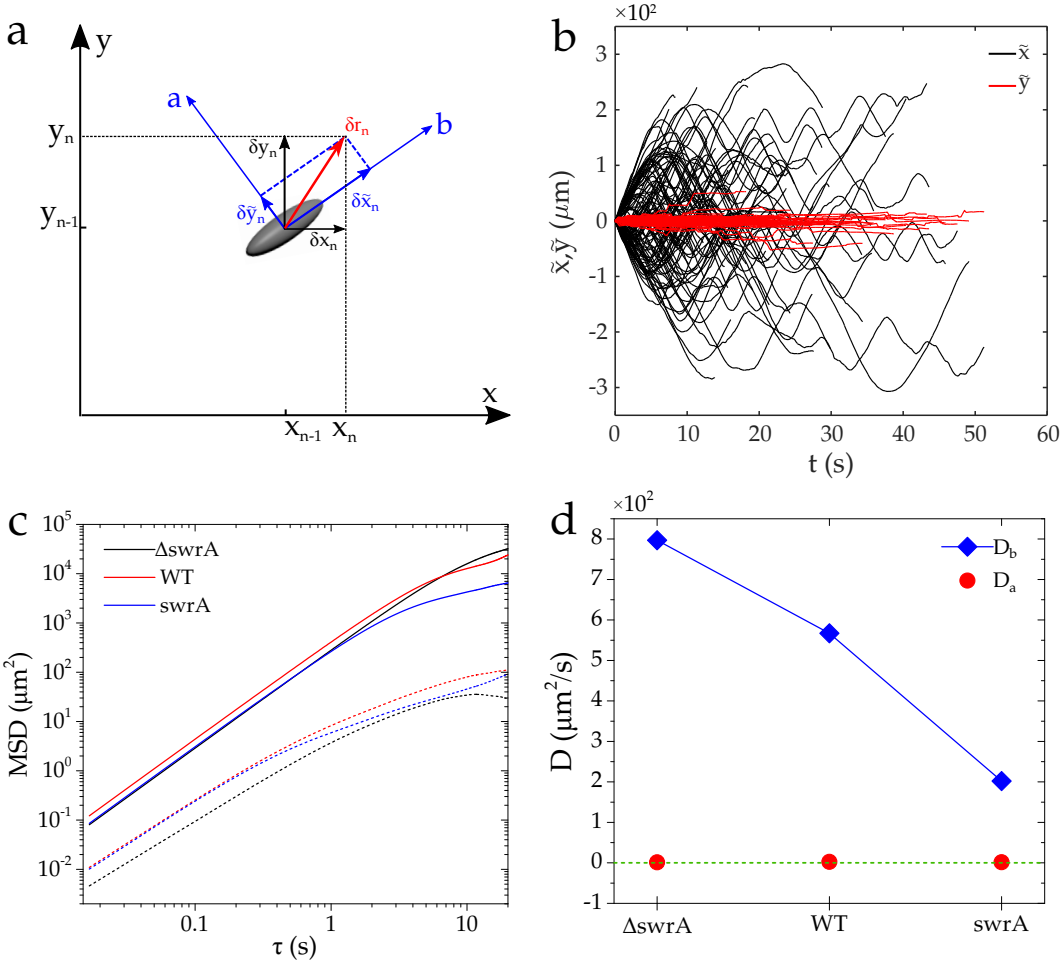

Figure 3.21: (a) Schematic diagram of decomposition of the velocity vector in the lab-frame and body-frame. (b) Temporal evolution of the total displacement components $\tilde{x}$ and $\tilde{y}$ in the body-frame. (c) Decomposed MSDs in the body-frame. Solid (dotted) curve indicates parallel (perpendicular) direction. (d) Components of the diffusion coefficient in the body-frame. The component D_a (D_b) represents perpendicular (parallel) direction.

Using the wobbling angle, the displacement of cell can be decomposed into components parallel and perpendicular to the body major axis in the co-moving coordinate system with the cell body that is indicated by $\delta\tilde{x}$ and $\delta\tilde{y}$ (see Fig. 3.21a for a schematic representation). The components of displacement in the lab-frame are specified by δx and δy. One can calculate the total displacement in the body-frame coordinate by summation over all steps of displacement, i.e. $\tilde{x}(t_n)=\Sigma_{k=1}^{n}\delta\tilde{x}_k$, and consequently construct the body-frame displacement for trajectories of duration t at starting time τ_0 by $\Delta\tilde{x}(t)=\tilde{x}(t+\tau_0)-\tilde{x}(\tau_0)$. Mean square displacement in the body-frame can be measured similar to the lab-frame using $<[(\Delta\tilde{x}(t))^2]>=2tD_{\parallel}$ and $<[(\Delta\tilde{y}(t))^2]>=2tD_{\perp}$ where $D_{\parallel}$ and $D_{\perp}$ stand for the parallel and perpendicular components of diffusion coefficient to the orientation of the cell body, respectively [134]. Displacements, MSDs, and diffusion coefficients in the body-frame are illustrated in Figs. 3.21b-d. The perpendicular diffusion coefficient $D_{\perp}$ is very small and negligible in comparison to the parallel counterpart $D_{\parallel}$ due to the wobbling of the body. Parallel diffusion coefficient $D_{\parallel}$ in the body-frame exhibits the same trend as the free swimming cells and decreases with increasing flagellar number while the values are smaller because of circular or highly curved trajectories.

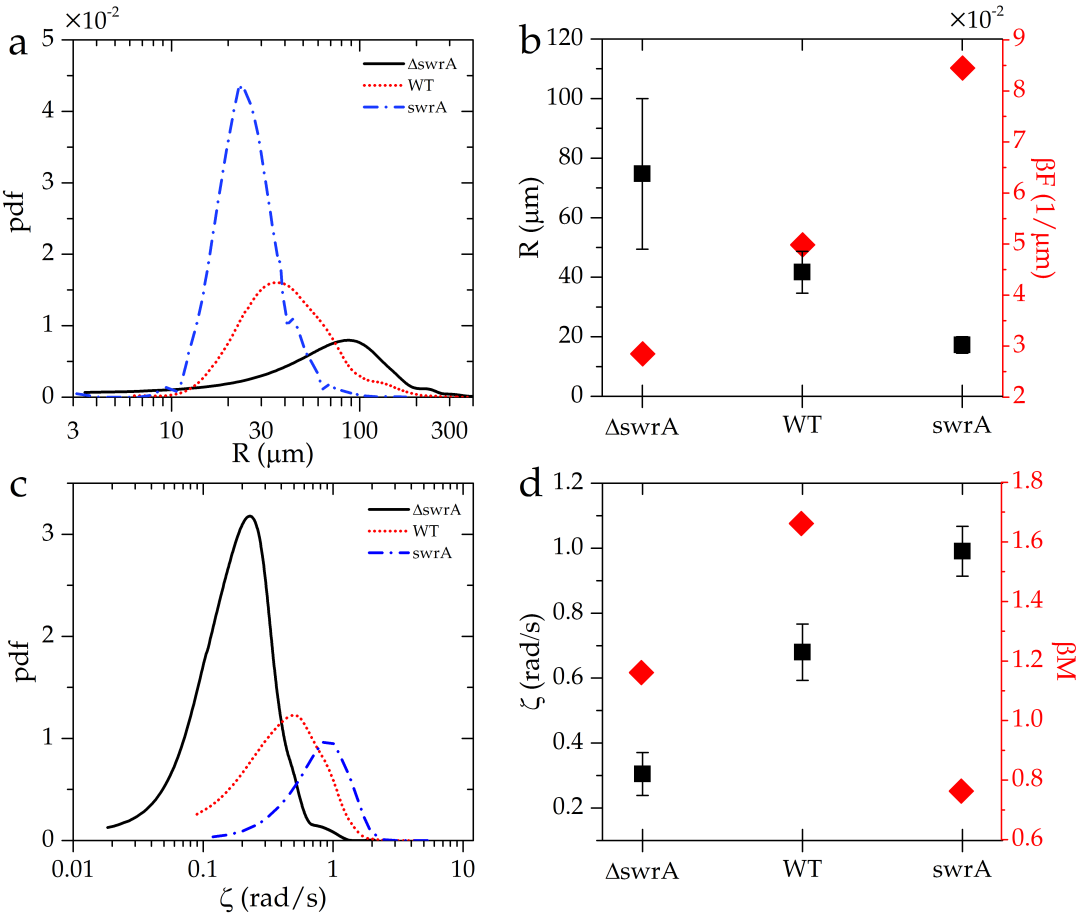

Figure 3.22: (a) Distributions of the radii of curvatures are shown for circular trajectories in semilogarithmic scale. (b) Average radius of curvature R and scaled propulsion force βF for different strains. (c) Distributions of the angular frequencies for the circular tracks in semilogarithmic scale. (d) Average angular frequencies ζ and dimensionless torque βM for different strains are estimated.

The curvature of the path depends on the specific number of points which are used for the measurement although the trend is always the same due to the reflection of rotational diffusion of the strains. Therefore, a semi automated customized Matlab script was used to fit a circle to parts of the trajectory which are determined by the user. The radii of circles are not noticeably influenced by the small variations along the path and are much more robust than the curvature. Other intended quantities such as the cell length and average speed in the intervals can be measured as well. The chirality of the circular motion depends on the slip length of the surface [135, 136]. Chirality has been reported to be clockwise above a solid surface [108, 137] and counter clockwise near the liquid-air interface [138]. Considering a circular motion and using the radius and translational velocity, one can calculate the angular frequency ζ=v/R for the curved parts of the path. The distributions of radii and the average radius for different strains are plotted in Figs. 3.22a and b. The distribution broadens and its peak moves towards larger values for the cells with lower flagellar number. The average radius decreases with increasing the number of flagella. The distribution of angular frequencies and their average are illustrated in Figs. 3.22c and d. Angular frequency ζ increases with the flagellar number in contrast to the radius R due to approximately equal translational velocity. To get an approximate insight into the torques and forces excreted on a bacterium when it swims in a circle, the solutions

from equations of motion in the noise free conditions are utilized [139],

$$R = \frac{D_{\parallel} F}{D_{\mathrm{r}} M}, \tag{3.9}$$

$$\zeta = \beta D_{\mathrm{r}} M. \tag{3.10}$$

The parameter F is an effective self-propulsion force directed along the cell body orientation and M is a torque in the direction perpendicular to the plane of motion. The system temperature T is included in the equations via $\beta = 1/k_{\mathrm{B}}T$. Using these equations and directly obtained quantities from the circular motion, we can estimate a dimensionless torque $\beta M = \zeta / D_{\mathrm{r}}$ and afterwards scaled force $\beta F = \zeta R / D_{\parallel}$ as are indicated in Figs. 3.22b and d. The dimension of βF is the inverse length and because the only important length scale in the system is radii of circular paths, βF increases with the flagellar number, indicating larger effective propulsion force for the strain with more flagella. This enhanced propulsion force does not lead to higher velocity at least in swrA strain because wobbling angle and effective cell aspect ratio including bundles (section 4.4.3 in the next chapter) rise at the same time, and hence drag force increases accordingly. The dimensionless torque does not vary in a monotonic way with the number of flagella and is maximum for the wild type strain.

Moreover, the radii of circles weakly correlate with the cell length and there is a loose anti-correlation between the cell length and speed in both circular and random trajectories.

3.4.7 Correlations

In this part, I briefly discuss the dependence of different swimming parameters to each other for wild type strain as a reference and present some of the results as graphs.

It is likely that slower cells remain in the field of view for a longer time and accordingly, play dominant contribution in the statistics. There is still anti-correlation between the temporal length and speed of the trajectories (Pearson correlation coefficient $r = -0.22$) although cells which were slower than mean speed minus double standard deviation were removed from the analysis. The residual anti-correlation could be due to the longer swimming of slower cells in the focal plane. Average cell speed and its angular velocity in both run and tumble phases are anti-correlated (Fig. 3.23a). Angular velocity was obtained based on the variation of velocity direction, and thus rapid changes of swimming direction reduce propulsion speed. Rotational diffusion decreases with increasing run speed because it was also measured based on the velocity directions (see Fig. 3.23b). This correlation is weaker than the one between the angular velocity and speed of the run phase. The absolute turning angle reduces with increasing tumbling velocity meaning that cells need to slow down sufficiently for efficient reorientation (Fig. 3.23c). Tumbling demands bundle disassociation or at least some flagella desynchronization and separation from the bundle. Separated flagella exert a torque on the cell body and realign it depending on the cell size, the number of detached filaments from the bundle, and spatial arrangement of flagella on the cell body. Separation of more filaments from the bundle leads to a larger reorientation [43] and consequently a dramatic decrease of the tumble speed. Turning angle is strongly correlated with the angular velocity of tumbling phase (Fig. 3.23d).

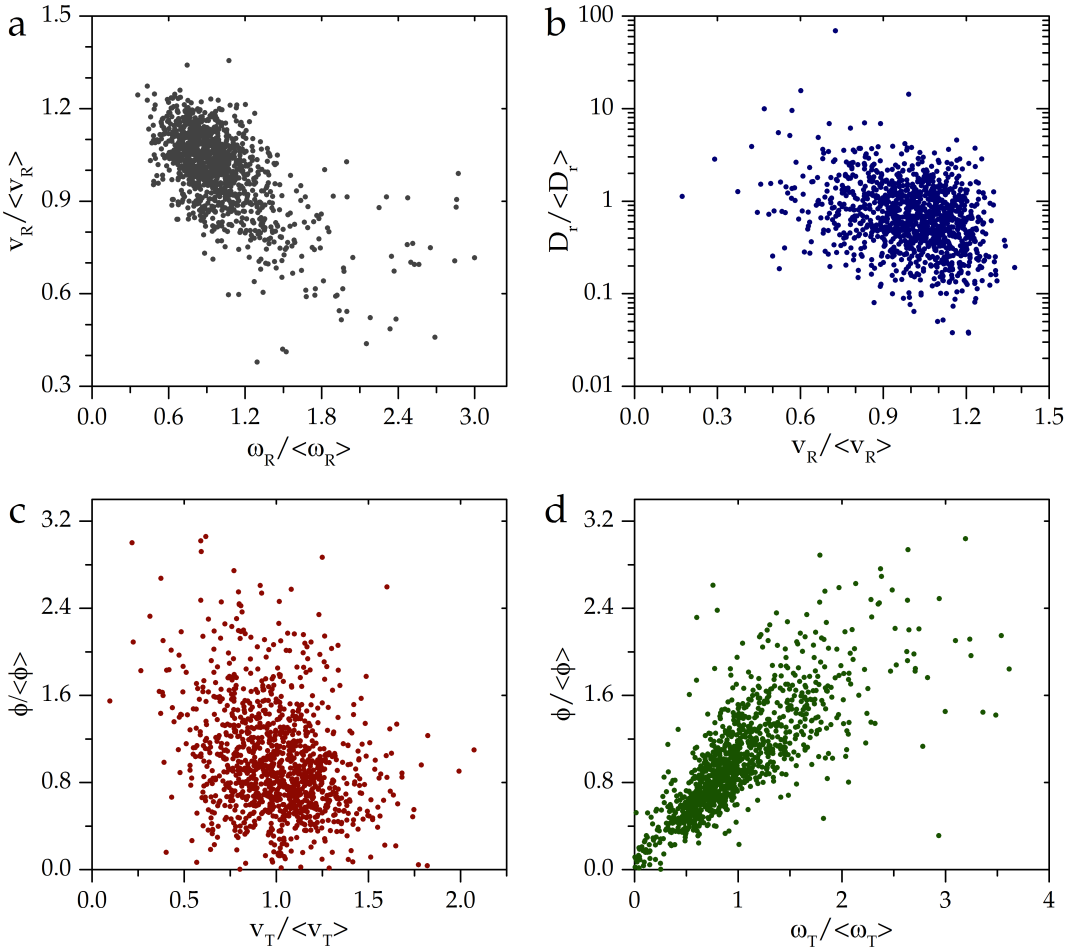

Figure 3.23: (a-d) Illustrative graphs of correlation between various swimming parameters. v_R (v_T) is run (tumble) speed and ω_R (ω_T) is run (tumble) angular velocity. D_r represents rotational diffusion of the run phases. All quantities are normalized to their average value, and we note that the graph in (b) is in semilogarithmic scale for better visualization. Pearson correlation coefficients for (a-d) are r=-0.57, -0.17, -0.27, 0.77, respectively.

3.5 Summary

To summarize, we found out that with increasing flagellar number there is no trend in the swimming speed while all angular quantities including rotational diffusion, turning angle after tumbling, and wobbling angle increase. The average time a bacterium spends for the tumbling is independent of its flagellar number. The run time decreases with the number of flagella supporting the 'veto model' for tumbling which states that one single flagellum or few flagella (less than half of the flagellar number) can be enough to induce a tumbling event. These tendencies all act in the same direction, and increase the persistency of motion during the run phases and tumbling events. Consequently, translational diffusion of the cells decreases with the number of flagella. The tumble speed is highly correlated with the run speed, and it can be approximated as half the run speed. The significant value of the tumble speed motivated us to develop a two-state random walk model, which in contrast to the standard models in the literature, incorporates the time of the tumbling events as well. The model was used to reproduce the MSDs. Then, the phase spaces of the translational diffusion in the planes of practically relevant parameters, i.e., rotational diffusion, turning angle, and run time, were obtained. We realized that the most crucial quantity which can

largely modify the transportation efficiency is rotational diffusion in the range of our experimental parameters. We performed Monte Carlo simulations of the random searchers, and calculated the mean first passage time as a function of the persistency during the run phases or rotational diffusion. Each corresponding curve develops a minimum depending on the size of the search environment. If optimizing the search efficiency was the primary goal of evolution, the flagellar number of the wild type cells has been optimized for the environments which their size are in the order of few millimeters. Moreover, having too many flagella is advantageous for the local search and slow spreading processes such as biofilm formation which needs initial attachment of the cells to the surface, while fewer flagella are beneficial for long distance search and fast spreading. In this sense, wild type with an intermediate number of flagella can have the optimum global search efficiency in short and long distances. The radii of the circular trajectories interacting with the surface also decrease by increasing flagellar number.

4

Flagella and Bundle Visualization

Contents

4.1 Literature survey

Detailed study of the bacterial motility was complicated due to the difficulty of seeing individual flagella which are too thin to be resolved by the light microscopy. The movement of flagella, as the main organelles of motility in live bacteria, was first observed by Ehrenberg who studied species with large flagellar bundles such as *C. okenii* [140]. Reichert used dark field condensers with high numerical aperture to see the motion of flagellar bundles of even smaller bacteria [141]. However, the initial examinations of the flagella were mostly limited to the immotile cells and were aimed to investigate the arrangement, shape, and geometrical properties of the filaments using the methods such as electron microscopy [142, 143]. The first description of the polymorphic transformation was reported by Pijper who noted that wavelengths of the flagellar bundles could vary by a factor of two with the overall length of the bundle remaining constant [144]. The term *biplicity* was suggested for this doubling phenomenon. Macnab used dark field microscope along with short-arc xenon or mercury lamps of high surface brightness as a light source to observe moving flagella including single filaments on completely motile cells. He established our current

understanding of the transition between runs and tumbles [145–147]. Polymorphic transformations of isolated flagellar filaments that at one end were rigidly attached to the glass slide and exposed to the flow of viscous medium have been also studied using the dark filed technique [148]. Laser dark field microscopy has been developed to analyze motor function in more details by measuring the high speed rotation of single flagellum at low load with a temporal resolution higher than one millisecond [149]. This technique has been applied in another study to estimate the bacterial swimming speed and rotation rate of the bundled flagella simultaneously [150]. A serious difficulty with dark field microscopy with intact cells is the flare from the cell body obscuring the view over distances of several micrometers. Grossart employed fluorescent protein stain 'NanoOrange' for visualization of bacterial flagella [151]. The NanoOrange reagent can be bound to hydrophobic regions of proteins and substantially enhance fluorescence while the unbound reagent is essentially non-fluorescent. Turner et al. have also introduced a simple procedure for fluorescent labeling *E. coli* bacteria and their filaments that allows to observe their motion in real time [44]. They tried different dyes and obtained the average flagellar length ~6.2 μm for different dyes. The shape of flagella, e.g. pitch length, on an organism can be modified to some extent by environmental conditions such as temperature, pH value, and colloidal content of the medium, and it can undergo distinct mutational variation [142, 144]. The degree of curvature of the flagella in some studies has been considered to be significant due to the appearance of only one or two curves regardless of the filament length [142]. Pijper realized different kinds of bacteria have their own pitch length ranging from 0.6 to 5.058 μm while the distribution over the various species does not indicate an obvious pattern or correlation with the other characteristics [144]. Reichert estimated the pitch length of screw-like flagella of *S. typhi* as 2.5 μm, *P. vulgaris* as 2 μm, and *Sarcinas* as 3 μm, occasionally 2 μm or even 1.8 μm [141]. Weibull shook-off the flagella of *P. vulgaris* and *B. subtilis* with ammonium sulphate and described the helices by a period of 2 and 2.5 μm, respectively [152]. Macnab observed the early motility of *E. coli* and *B. subtilis* with the normal flagella and declared the curly form appears during tumbling [147]. He also observed a coiled form with the helical diameter 1.6 μm and the pitch length approximately 0.5 μm in the case of *E. coli*. The pitch length and helical diameter of the left handed flagella of *Salmonella* have been measured as 2.34 μm and 0.42 μm [153]. It had been traditionally assumed peritrichous bacteria can make single bundle as they swim [3] before the observations of Martin Li who for the first time in his thesis qualitatively studied filamentous cells of *E. coli* and *B. subtilis* [50, 113]. He revealed peritrichous bacteria with lots of flagella can simultaneously form several bundles. His observations were later confirmed by boundary element method simulation of swimming cells, where the authors argued that the experimentally observed pitch length larger than 4 μm in the wiggling trajectories of *B. subtilis* cells can be justified by formation of several bundles [112].

4.2 Motivation

The dynamics of swimming with several bundles have not been well understood so far, while the spinning bundles are accepted as the main appendages of most microorganisms to propel themselves in low Reynolds number regime [3]. Our understanding of the multiple bundles is only limited to the qualitative description of swimming *B. subtilis* and filamentous *E. coli* cells [50]. The critical question is how the number of bundles statistically changes, and how it can be linked to the flagellar number of a bacterium. It is also not known how the configuration of bundles can generally

modify the cell geometry, and consequently what the impact is on swimming dynamics. Moreover, shedding some light on the mechanism leading to the formation of multiple bundles and quantitative characterization of the bundle arrangements can arise some fascinating questions regarding the interaction of bundles and their stability in various configurations. *B. subtilis* cells are longer than *E. coli* and generally have at least around two folds more flagella than their gram negative counterpart, *E. coli*, that makes it complicated to study the dynamics of their bundle formation.

4.3 Methods

4.3.1 Fluorescent staining of flagella

To get an insight into the dynamics of swimming cells that were studied in the previous chapter, the flagellar properties and dynamics of bundles of the same strains have been investigated here. Fluorescent staining of the flagella in *B. subtilis* requires the presence of hag_{T209C} modified filaments [154] in which the native *hag* gene exchanged with hag_{T209C}. Blair et al. genetically modified one of the non-essential exposed amino acids on the outer sub-domain present on the surface of the flagellin protein. The side chain (residue) of the mutated amino acid ($amyE$::$Phag$–hag_{T209C}) was particularly assigned as the target for special site for the binding of fluorescent dye molecules. Binding of the dye molecules is enough to observe the entire length of the flagella because of the high density of exposed residues on the flagellin peptide chain [50, 154]. T209 to C mutation can be obtained by quick-exchange mutagenesis [155]. We followed the protocol that was used for the swimming assays to prepare the overnight cultures (see 3.3.1). The overnight culture was diluted to OD_{600}~0.1 in the morning and grown for around two more hours to reach the optical density of ~1. After dilution, swrA strain was induced by 1 mM IPTG solution to increase the number of flagella. The dye was prepared by solving 1 mg AlexaFlour®568 C5-maleimide in 200 μl DMSO (dimethyl sulfoxide). We centrifuged 1 ml of the cell culture at 8000g for one minute and gently washed it three times in PBS (phosphate-buffered saline) pH 7.4 (1X) to remove the thiol-rich material from the medium with which the dye might react. The pellet was resuspended in 200 μl PBS and then 5 μl dye solution was added. The suspension was thoroughly mixed and incubated in the dark at room temperature for 20 minutes and washed three times again in PBS buffer. The washing after staining was to remove excess unbound dye and reduce the background light. Cells were re-energized by half hour outgrowth in LB at 37 °C to observe motile cells.

4.3.2 Microscopy

Fluorescence imaging implies to the observation of fluorescent signals emitted by samples that were labeled with the fluorescent dyes or by the fluorescent proteins themselves. In fluorescence imaging, the sample is only illuminated with the excitation light of the target wavelength, with the aim of viewing only the fluorescent signal emitted by the sample. Emitted light has longer wavelength than excitation light that is known as *Stokes shift*. This shift enables one to separate the absorption spectrum from the emitted spectrum. Emitted light by a source such as a mercury or xenon lamp has an extremely broad wavelength range. The *mirror unit* consisting of excitation filter, dichroic mirror, and emission filter is employed to choose light in a specific wavelength range. Excitation filter limits the illumination from the light source. Out of a broad spectrum, it only permits the light in an optimum excitation wavelength range for the fluorescent dye to pass through. Dichroic mirror reflects the

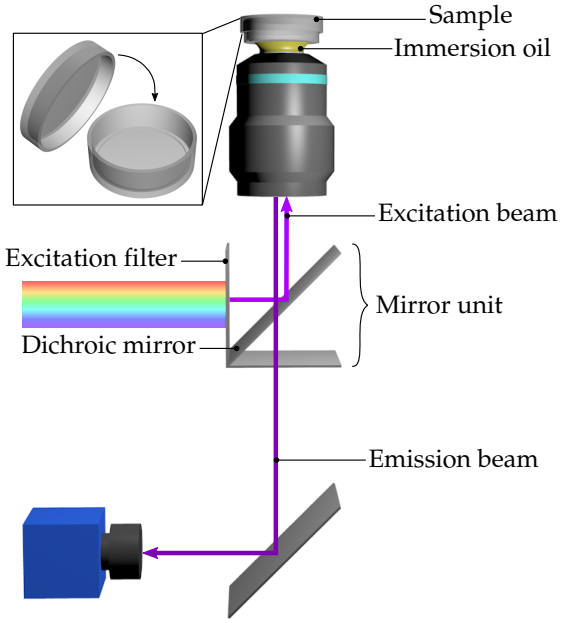

Figure 4.1: Schematic representation of the individual components and arrangement of a fluorescent setup. The central part of a fluorescence microscope is the mirror unit which chooses the light in demanding wavelengths. The inset image shows a FluoroDish which was used as the chamber.

light with wavelengths shorter than a specified wavelength towards the objective while allowing longer wavelengths, e.g. excitation light, to pass through and be transmitted. Emission filter completely blocks any unwanted residual excitation light permitting the passage of only desired longer emission wavelength from the sample. The entire fluorescence process is periodical until the fluorophore is irreversibly destroyed in the excited state that is known as *photobleaching*. Fluorescence image qualities can be compromised by the background signals either from endogenous sample constituents, i.e., autofluorescence, or from unbound and non-specific reagents. Schematic of the fluorescence imaging configuration along with its components are presented in Fig. 4.1 [156].

Confocal fluorescence microscopy offers several advantages over conventional wide field imaging including the ability to control the depth of field, reduction of the background information away from the focal plane, and the capability to collect serial optical sections from the thick specimens. The principle of confocal approach is exploiting spatial filtering techniques to discard out of the focus light and glare in the specimens whose thickness exceeds the immediate plane of focus. This objective can be achieved by means of adding a spatial pinhole located at the confocal plane of the lens to remove the out of focus light [157]. The confocal fluorescence microscopy has been also examined for the bundle visualization although it was not suitable due to rather high dynamics of motile cells.

Fluorescence microscopy samples were prepared by pipetting 30 μl of the stained bacterial suspension into a FluoroDish FD35-100. The droplet was covered by a circular cover glass (VWR, diameter 22 mm, thickness NO. 1.5) and the lid of the container was closed. The approximate height of the bacterial film was 80 μm. A Nikon Eclipse Ti microscope equipped with a Nikon N Plan Apo λ 60x, N.A. 1.4 oil immersion objective was utilized for the wide field fluorescence microscopy. The dye was excited by a mercury pre-centered fiber illuminator (Nikon INTENSILIGHT C-HGFIE) and images were acquired using Hamamatsu ORCA-Flash 4.0 camera with

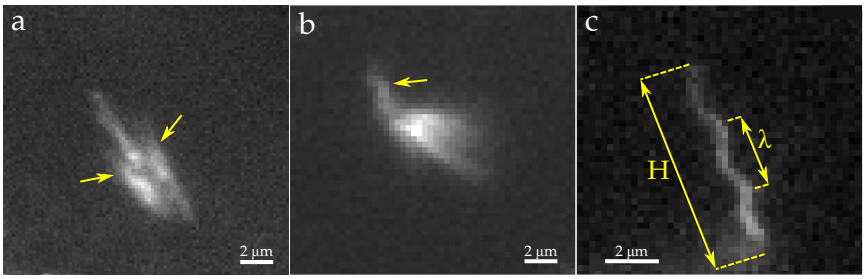

Figure 4.2: (a) Examples of short bundles are indicated by arrows which could not make separate effective bundles. (b) Some flagella can detach from the main bundles during the swimming. (c) Representative stationary filament that was used for the measurement of flagellar characteristic lengths.

25 or 30 ms exposure time and 2×2 or 4×4 binning. The pixel size of the camera without binning was 0.11 μm. The mirror unit was consisted of TxRed HC filter set (manufactured by Semrock). Videos were recorded around the middle of sample in the vicinity of glass surface where the cells spend longer time and the cell density is higher [101, 110].

4.3.3 Data analysis

The recorded videos in nd2 format were manually analyzed using Fiji software. All frames of each data set were reviewed and the intended quantities were measured when two bundles had been located on the observation plane. The measurements were repeated for at least five different frames for each data point. We studied 30 cells for each of ΔswrA and swrA strain and 35 cells for the wild type strain in total. Moreover, labeled bundles were tracked by TrackMate plugin of Fiji to get the approximate running speeds after careful elimination of the tumbling intervals. The trajectories were smoothed using a moving triangle with the width of 17 points before the calculation of speeds. Temporal length of the trajectories was typically short and rarely exceeded a few seconds due to the restricted field of view.

4.4 Results and discussion

4.4.1 Multiple bundle arrangements

The bundle formation mechanism of *B. subtilis* bacteria with peritrichous flagellar arrangement is traditionally assumed to be similar to *E. coli* whereas its swimming dynamics has not been understood well. Swimming bacillus cells with one long bundle at the rear of body can have several bunch of short flagella. These flagella extend a few microns beside the cells body and are likely broken filaments due to the imposed shear by pipetting. Filaments within these bundles are often not long enough to form separate bundles and just encompass the main bundle as it can be seen in Fig. 4.2a. Thus, they do not have significant contribution in the cell propulsion. There are sometimes a few filaments out of the bundles, as it is shown in Fig. 4.2b. This was observed more frequently in the regular arrangement of bundles. We could not determine the helicity or rotation direction of these filaments due to insufficient temporal and spatial resolution of images but we suggest these filaments rotate CW according to the reports in the literature [43]. The striking feature of the dynamics of swimming bacillus is the formation of different bundles during the run phase (see Fig. 4.3). When the side flagella become a little longer, they can make two distinct

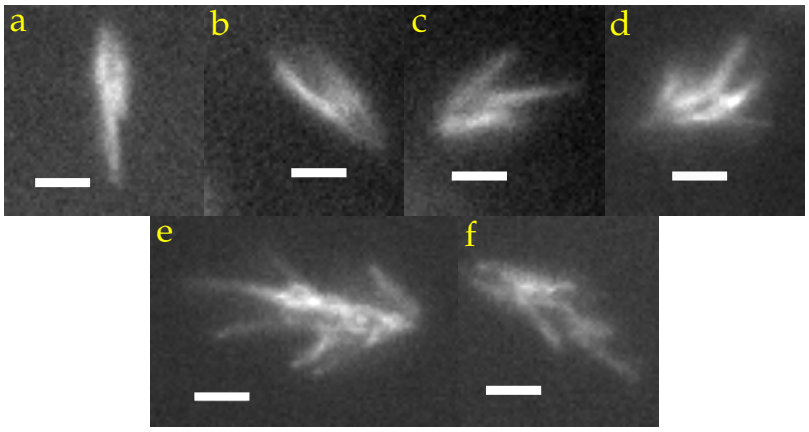

Figure 4.3: (a-d) Swimming wild type *B. subtilis* cells with different bundle arrangements varying from one to four bundles, respectively. (e-f) Long cells make several lateral bundles apart from the ones at the rear of the cell. Arrangement of the lateral bundles are sometimes asymmetric. These exemplary images belong to the Δswra strain. Scale bars are 3.5 μm.

bundles which are shorter than the main bundle along the cell body. Configurations with two, four, and even more bundles have been also observed. Individual rotating bundles in most of the configurations can symmetrically sweep a cone-like shape but sometimes their length or width are slightly different, especially due to the broken flagella or bending the distal end of the bundle out of the observation plane. Cells with longer body length frequently make more than four bundles which are almost always asymmetric with several lateral bundles (Fig. 4.3e and f). It qualitatively seems that these cells swim slightly faster due to their larger directional persistency. Due to the dispersion of flagella over the surface of the bacterium and extension of the multiple bundles outward of the body, we could roughly estimate the cell orientation even though the cell body was not stained in our experiments. The irregular arrangements of bundles were excluded from quantitative characterization since they are abnormal, and furthermore, it is not feasible to measure the specific geometrical parameters that will be defined in the following section.

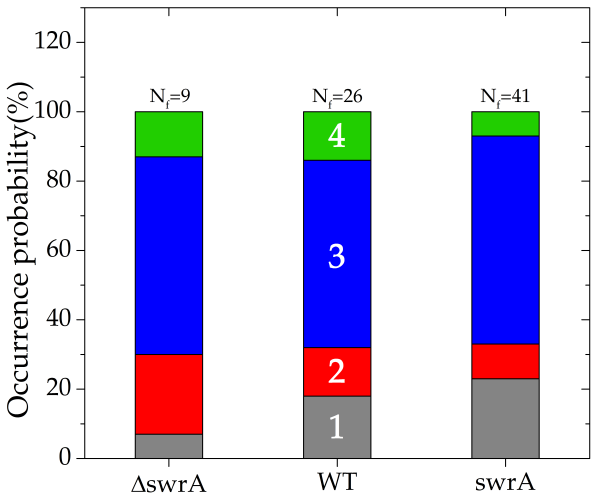

Figure 4.4: Percentage of the probabilities of making multiple bundles for each strain. Formation of three bundles appears as the most probable case regardless of the number of flagella. There is no significant difference between the strains according to the outcomes of the t-test in which their p-values are larger than 0.2.

Li in his thesis reported that Cefalexin treated long filamentous *E. coli* cells have more flagella than cells with the normal size, and they make numerous bundles during swimming [50]. He assigned the formation of several bundles to the number of flagella while he could not distinguish significant correlation between the number of flagella and bundles. In contrast, it appears from our experiments that the number of bundles should be attributed to the cell length instead of flagellar number as it was qualitatively observed in the cells with more than four bundles. The most probable number of bundles that cells can make is three bundles independent of the flagellar number. In fact, more than 50% of investigated cells for each strain have three bundles. Around ~20% of examined WT and swrA cells only make one bundle that is higher than the cells with least number of flagella. The effective size of WT and swrA cells is larger due to the abundance of flagella on the cell body and likely their flagella experience more shear during preparation that increases number of broken flagella and the possibility of single bundle formation. The percentage of probabilities of making several bundles for each strain is illustrated in Fig. 4.4. According to the results of t-test with the significance level of 0.05, there is no difference between the probabilities of multiple bundles formation among the strains. Interestingly, it was also observed that the number of bundles every bacterium can make is not restricted, and likely depends on the position and amount of the CW rotating filaments departed from the bundles. Series of snapshots of a bacterium which could adopt distinct bundle configurations is depicted in Fig. 4.5 with 0.17 s time lag between the frames. The bacterium which is indicated by an arrow swims with double bundles in frames a-e, tumbles between frames f-i which takes around 0.6 s, and then returns to the run phase with a single bundle after rather large turn. It seems that the number of bundles is only a geometrical issue and bacteria make multiple bundles when they cannot incorporate all of their numerous flagella in the same bundle as they have several lateral bundles in long cells. Moreover, the flexibility of filament, hook, and

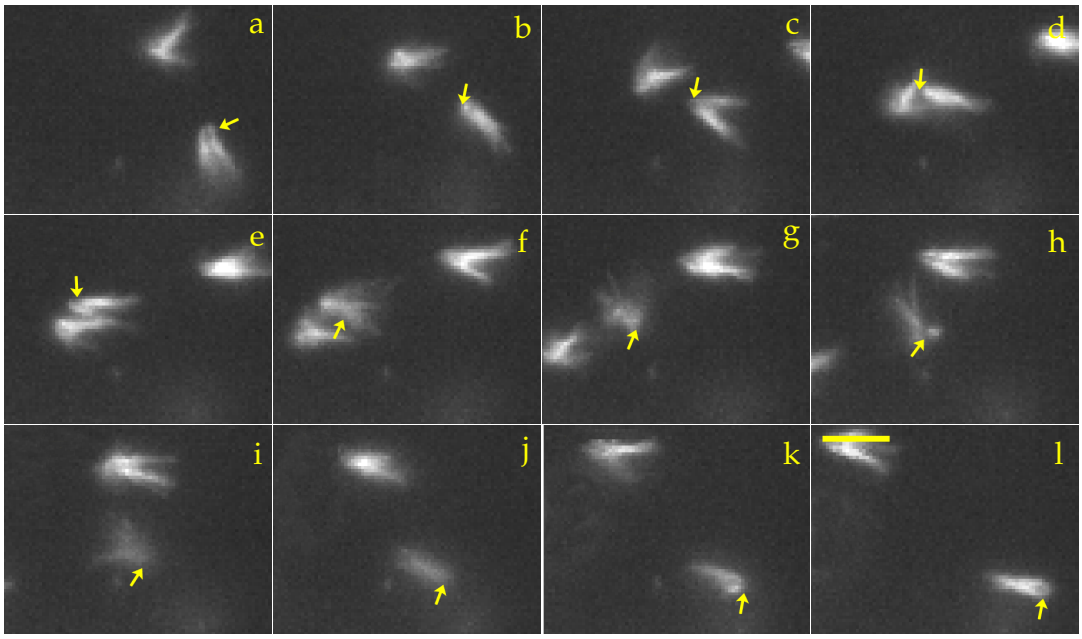

Figure 4.5: Snapshots of a bacterium switching from double bundles to single bundle. (a-e) The bacterium that is indicated by an arrow runs by means of double bundles. (f-i) It tumbles and turns in a sharp angle when its bundles disperse. (j-l) New run is started with a single bundle. The scale bar for all frames is 4 μm. The time lag between the frames is 0.17 s.

also the torque generated by the motors can influence the number of bundles. Here, it is assumed all the mutants have similar motor and flagellar properties.

4.4.2 Bundle and flagella properties

The simplest view of bundles is when only two bundles are placed on the observation plane as can be seen in Fig. 4.6a. We measured several quantities in this condition for bundles including their length and width. The measured parameters are schematically drawn in Fig. 4.6b. The length of the bundle l was measured from the distal ends of the bundles to the approximate middle of overlapped area by the bundles. The width of the bundle w for cases with multiple bundles was measured at the rear of overlapped region where the bundles extend outwards of the body. The width of single bundle was measured in the middle of bundle since the body was not distinguishable in most of the situations (see Fig. 4.6b). The distributions of bundle width have two peaks where the peaks with larger width belong to the cells with one bundle as it can be seen in Fig. 4.7a. The cell body in the middle of a single bundle probably prohibits the formation of a tight bundle although the contribution of more flagella in the single bundle can also lead to a wider bundle. The average bundle width is ~1.64 μm that is

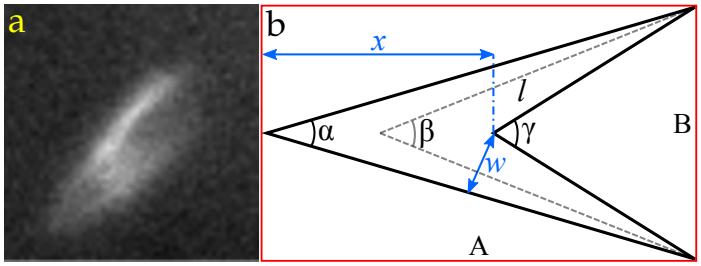

Figure 4.6: (a) Illustrative image of bundles as they are on the observation plane. (b) Schematic sketch of the bundles and the parameters that were extracted from the experiments.

roughly two folds larger than the width of the cell body and represents a very loose bundle. It appears that the bundle widths in ΔswrA and WT strain are almost the same despite the higher flagellar number of wild type cells. But the bundles broaden by placing extra flagella in swrA strain. One should keep in mind that not only the number of incorporating flagella in the bundle determines the bundle width, but other parameters such as torque and bundle rotation rate can also influence the tightness of the bundle. This points out that the bundle rotation rate of swrA strain can be smaller than two other strains due to geometrical restriction. The average bundle length is ~7.21 μm which is in the same order of the cell length (Fig. 4.7b) and agrees with the reported values in the literature [50, 158]. The other parameter that we evaluated for the bundles is a scale of the body of cell which we indicated it by x in Fig. 4.6b. The corresponding values for different strains do not show any trend and their average is ~4 μm. The average length of the cell body from the tracking experiments by dark field microscopy for all strains was around 8 μm. This emphasizes that the overlapped area by the bundles does not cover the entire cell body and the outward extended bundles just partially mask the cell surface.

We also considered few characteristic length of twenty individual unmoving or stuck filaments of WT strain which is assumed to have normal helicity (see Fig. 4.2c). We measured the filament pitch length λ=2.26±0.17 μm, diameter d=1.7±0.75 μm, and axial length H=6.7±0.86 μm where the errors are standard deviations. These results are in good agreement with the reported values for *B. subtilis* and *E. coli* in the

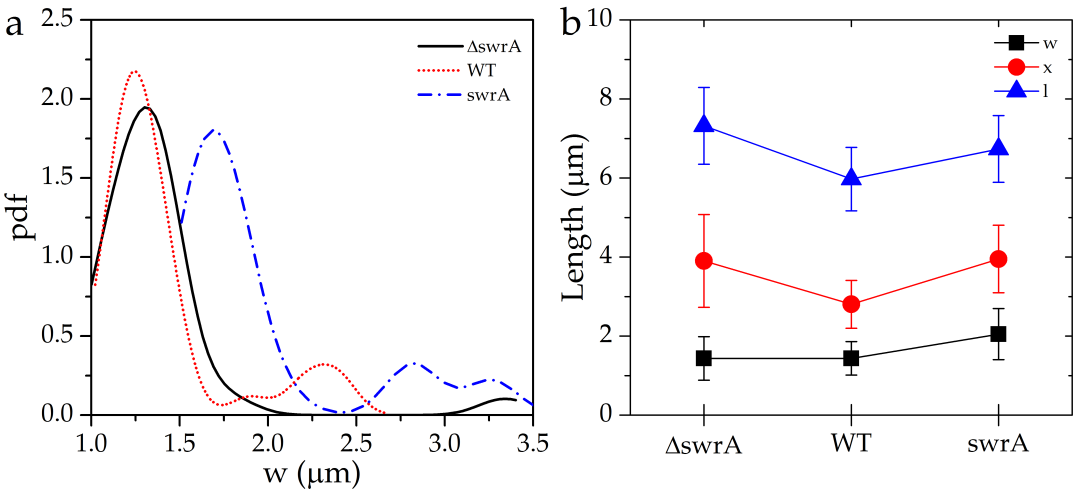

Figure 4.7: (a) Distribution of the bundle width w for various strains. (b) Measured length scales for the different strains are approximately the same (see Fig. 4.6b for the schematic illustration of the parameters).

literature [43, 44, 50]. One can use the formula $H\sqrt{1+\pi^2(d/\lambda)^2}$ to obtain 12.13±2.3 μm as the contour length of the filaments [43].

4.4.3 Effective aspect ratio of cells

The geometrical properties of the individual bundles and in particular their width were nearly the same without any significant tendency. Here, we discuss the relative alignment of the bundles on the observation plane to gain insight into the origin of different kinematic behavior of strains. To this end, we studied the projected angles between the bundles and considered three different angles between them in front, middle, and back of the intersection point of the bundles when they lie on the observation plane as was schematically drawn in Fig. 4.6b. These angles are correlated and increase from the tip to the rear of the cell, and they were measured together to ensure the tendency between the strains. Interestingly, the projected angles widen with the total number of flagella on the cell body. The middle projected angle ranges from 30 to 45 degrees while it can be generally smaller in three dimensional space. We define the effective cell aspect ratio as $\frac{A}{B}$ in Fig. 4.6b that can be easily shown is equal with $\frac{1}{2}\cot\frac{\alpha}{2}$. We assume this ratio partially includes the cell body in the same manner for all strains. The effective aspect ratio of the cells decreases from 2.5 in ΔswrA to 1.7 in swrA strain with increasing the number of flagella. The effective aspect ratios of cells including the bundles are remarkably smaller than the aspect ratio of the cell body without the bundle that is around 8 μm. Angles between the bundles and aspect ratios are presented in the graph of Fig. 4.8.

It was shown in the previous chapter that the most significant impact of flagellar number of *B. subtilis* bacteria is modification of persistency by varying angular parameters, i.e., rotational diffusion and turning angle after tumbling. The reason behind the connection between the turning angle and the flagellar number to some extent was explained based on the literature. The maximum average turning angle for *B. subtilis* strains is ~60° which is smaller than ~70° reported for *E. coli* cells [83, 110]. It is known *E. coli* is not polar meaning that the bundles can be formed at either end of the cell body. In fact, this type of bundle rearrangement is in favor of large reorientations after tumbling. Due to the formation of multiple bundles in *B. subtilis*, it is less possible that all of them reform on the opposite side of the body. Therefore,

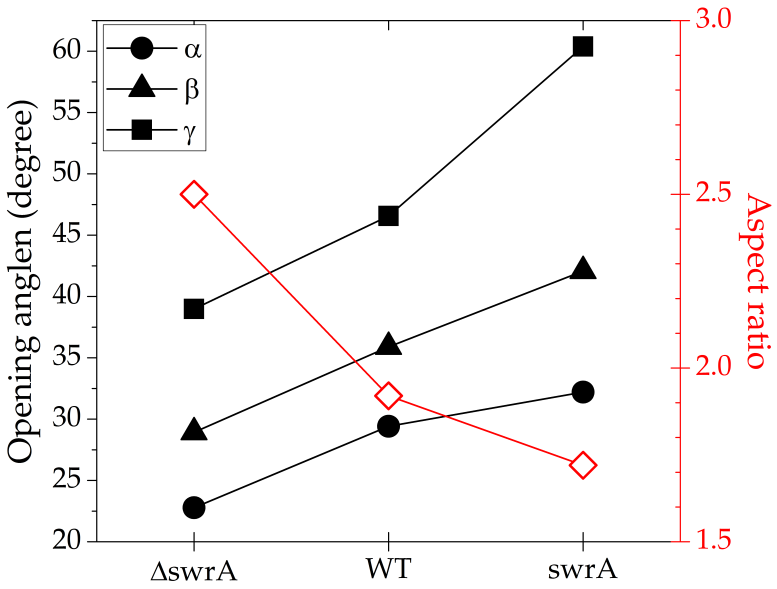

Figure 4.8: Opening angles between the bundles and effective cell aspect ratio for the strains.

the average turning angle decreases and the cells disperse more persistent than *E. coli*. Moreover, common analytical models such as resistive force theory approximate the bundle as a rotating single thick helix which is aligned along the main axis of the cell body. While this approach ignores the body wobbling, it predicts the swimming speed as a function of bundle rotation rate and its geometrical properties [25, 86]. The wobbling angle is correlated with rotational diffusion and they both increase with flagellar number (see Figs. 3.10c and 3.19a) where we associate these properties to the wider opening angle between the bundles. Wobbling is indeed due to the misalignment of the body relative to the bundle. The cell body has to rotate as well to compensate the imposed torque by the bundle rotation since swimming microorganisms are force and torque free [25]. Higher deviation of bundle relative to the body direction and likewise wider opening between the bundles will consequently cause a larger wobbling angle. The entire configuration of the bundles spins CCW when it is observed from the rear of the cell due to the CW rotation of the cell body. The hydrodynamic force between the helices rotating in the same direction is attractive and the helices can collapse to a single bundle. However, it has been shown that only the rotation of the cell body is sufficient to wind the helices even in the absence of hydrodynamic interaction and rotation of helices [88]. The body length of *B. subtilis* is longer than *E. coli* and the limited flagella length can suppress the collapse of all bundles to a single one. Incorporating several flagella from the large area of the cell surface into different bundles reduces the geometrical freedom of each bundle and keep them separated. In addition, this geometrical restriction is enhanced with embedding more flagella in the bundles which consequently makes the opening angle between the bundles wider.

Measurement of the translational diffusion coefficient using mean square displacement curve is more robust property of microswimmers since it can be calculated independent of the run and tumble characteristics of the cells. Slight change of rotational diffusion and turning angle after tumbling can substantially influence the transport properties of cells. The reported translational diffusion coefficients for *E. coli* range from ~150 to 500 $\mu m^2/s$ [137, 159, 160] which are less than the measured values for our *B. subtilis* strains due to formation of multiple bundles and higher persistency during run phase.

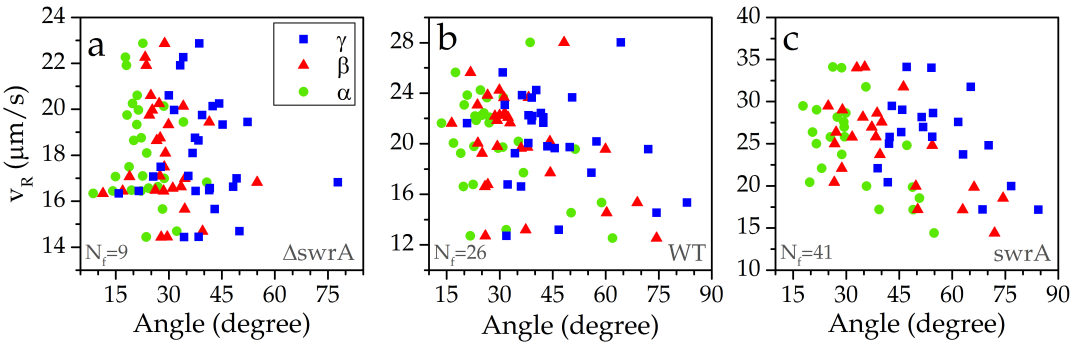

Figure 4.9: (a-c) Run speed as a function of projected opening angles between the bundles. The correlation coefficients of the middle angle β (solid triangle) for the strains swrA, WT, and ΔswrA are -0.65, -0.42, and -0.15, respectively.

4.4.4 Consequences of multiple bundles

The run speeds as functions of projected opening angles are represented in Fig. 4.9. The correlation coefficients between the middle angle and swimming speed for the strains swrA, WT, and ΔswrA are r=-0.65, -0.42, and -0.15, respectively. The correlation is not very significant for ΔswrA since the width of its distribution is not as large as the other strains. Although larger projected angle between the bundles directly increases the effective cell size and viscous drag, it also raises the wobbling angle that is in favor of speed reduction. It is remarkable to mention that swimming speed is a function of several parameters including the geometrical properties of the bundle, bundle length, orientation of the bundles relative to the body, and bundle rotation rate (see section 2.3.2 for a simple analytical estimation of propulsion force by single helix). Therefore, it is not straight forward to compare the run speeds between different strains especially in the absence of all aforementioned factors.

Run speed, middle opening angle, and bundle width as a function of number of bundles are shown in Fig. 4.10 for all strains as box plots. Run speed for swrA mutant decreases with increasing the number of bundles while this tendency for other strains does not monotonically hold as one or four bundles are exceptions. The projected angle between the bundles slightly decreases for ΔswrA and WT strain but it does not follow specific trend for swrA mutant. One may expect necessary reduction of the angle between the bundles by increasing the number of equally spaced bundles in a three dimensional cone-like arrangement but it should be kept in mind that our measurements were done on the two dimensional observation plane. The bundle width for different strains was discussed in section 4.4.2. It seems that the bundle width slightly contracts for ΔswrA mutant with more bundles while there is no specific tendency for the other strains. The widths of single bundles are around twice of the width of multiple bundles which can be due to the distinct way of measurement. However, decisive conclusion on the data shown in Fig. 4.10 is not feasible due to insufficient statistics. Collecting more data may not significantly help since the probability of observing different bundles is not the same, and it will mainly improve the statistics for three bundles (see Fig. 4.4).

4.5 Summary

In this chapter, we performed fluorescence microscopy to get further insight into the dynamics of bundle formation and flagellar propulsion. We observed that *B. subtilis* bacteria could make several bundles at the same time during the run phase as it was

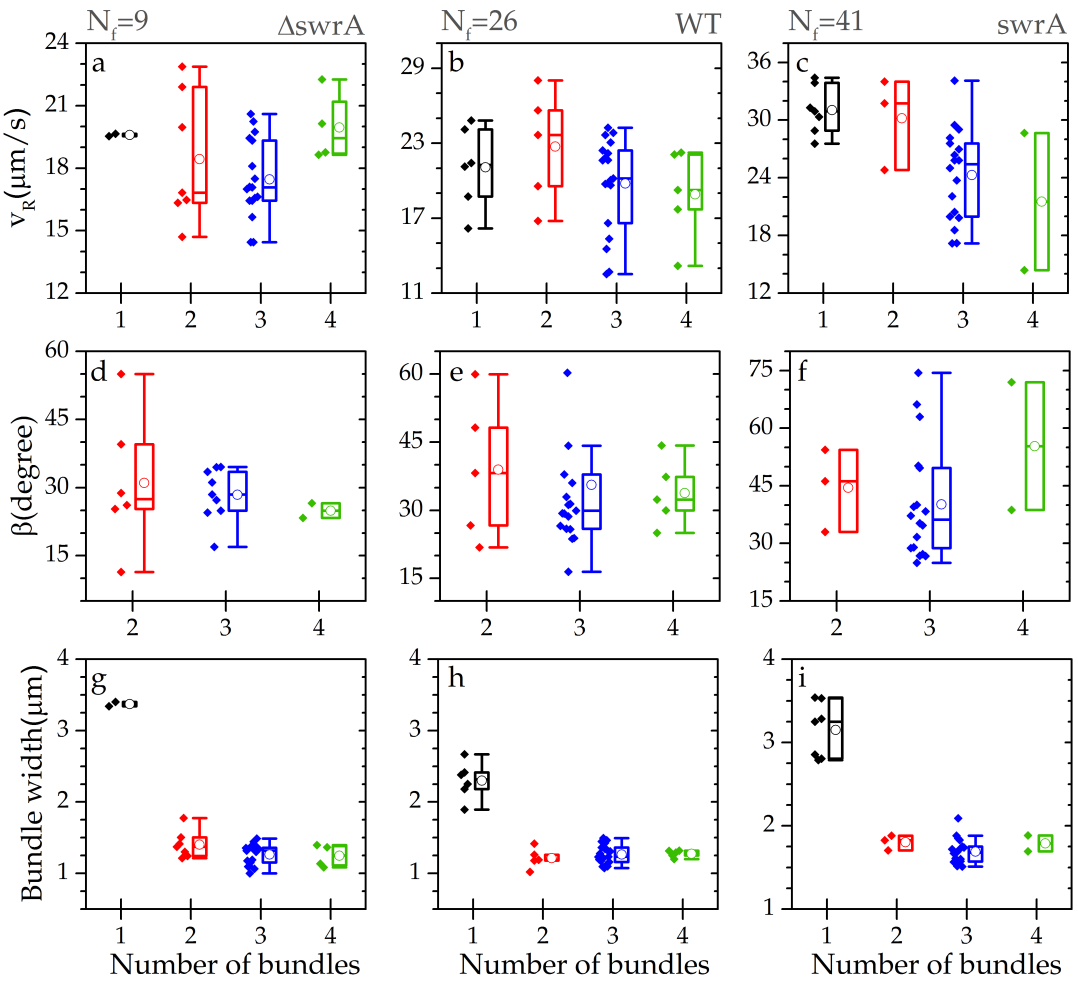

Figure 4.10: Variation of run speed (top row), projected opening angle (middle row), and bundle width (bottom row) as functions of the number of bundles are shown for different strains. Horizontal solid lines and hollow symbols inside the boxes show the average value and median for each set, respectively. Individual symbols belong to the measurements on one cell.

mentioned in the literature [50]. We quantified multiple bundle arrangements for the first time and found out that the number of bundles each mutant can make is independent of the flagellar number likely due to the similar cell body length. The most probable number of bundles is always three. The geometrical characterization of the relative bundle positions revealed that the projected angle between the bundles on the observation plane increases with the flagellar number. This causes that cells with the larger number of flagella have a smaller effective aspect ratio including their bundles. Run speed decreases with increasing projected angle between the bundles for each strain. Our visual inspections show that cells with longer body make several lateral bundles. Thus, we mainly associate the formation of numerous bundles to the geometrical restriction because of the long body length of *B. subtilis* in comparison with other peritrichous cells such as *E. coli*. The striking point is that the number of bundles for a bacterium can vary from one run phase to another, and it is not strictly defined for each cell. Bundles are loose with the width larger than the cell diameter, and their length is approximately the same as the body length.

5

Collective Motion

Contents

5.1 Literature survey

Simple active behavior of individual animal species within the crowd population often leads to emerging of complex collective motion. Flocking is one the most fascinating phenomena in nature that includes the complex classic example of ordered motion of flocks of birds and schools of fishes. Many individuals move coherently in a flock and respond to external stimuli while they have very restricted information about the entire flock [161, 162]. Collective motion has numerous advantages for the populations and is known to protect them from environmental challenges such as heat, chemical stress, predation, and sustain a suitable condition for reproduction. Some examples of the collective behavior at different length scales are depicted in Fig. 5.1. The statistical study of flocking began with the seminal work of Vicsek in 1995 [168] although there was an earlier model in the context of computer animation proposed by Reynolds in 1987 [169]. Vicsek introduced a minimal model where particles move at a constant speed and their only interaction is to align their moving direction with each other. Particles adjust their direction at each step to the local average within a radius R while exposed to some noises. Many studies have been inspired by Vicsek's work and from statistical physics point of view quantitatively characterized the dynamic transition from disordered random phase to polar ordered phase where

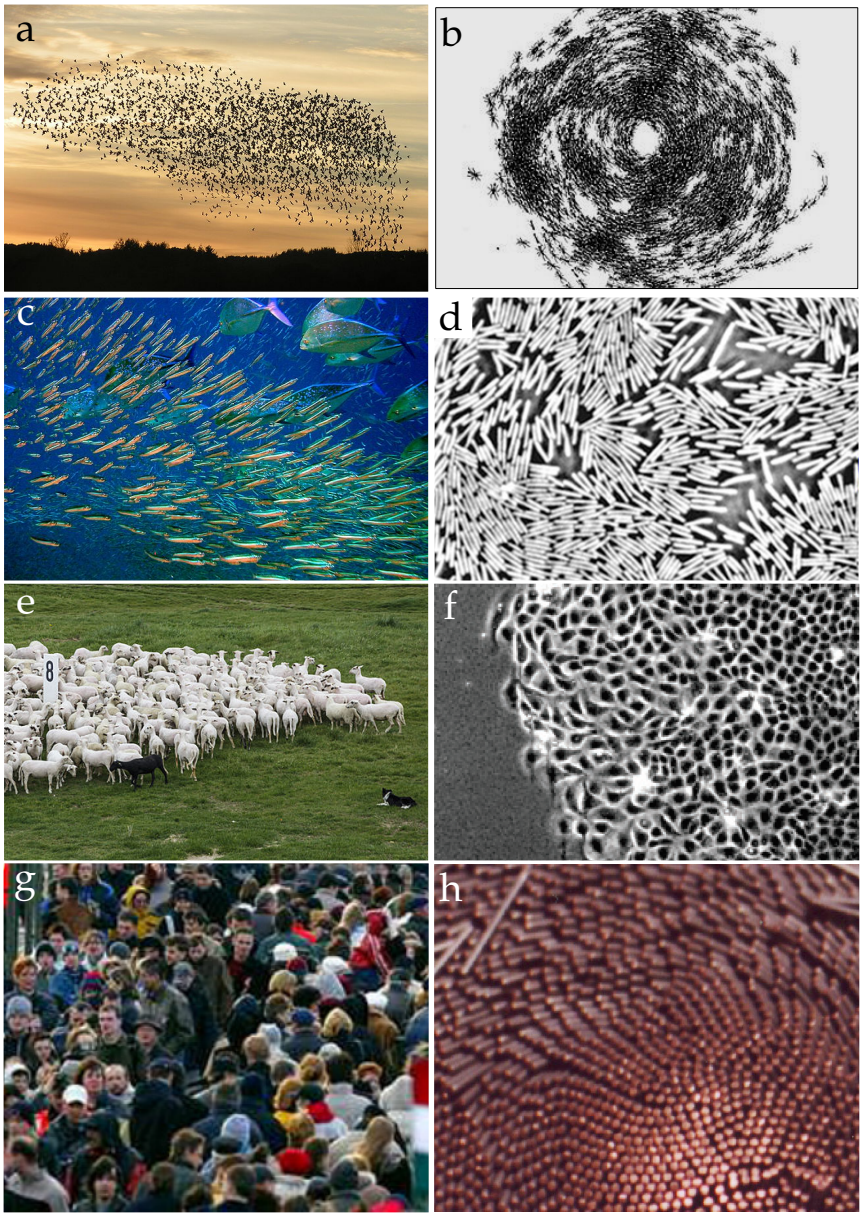

Figure 5.1: Typical examples of collective motion in nature. (a) Fascinating aerial display of starlings [163]. (b) Rotating colony of army ants [161]. (c) Vortices of schooling fish [164]. (d) Swarming bacteria on the agar surface [21]. (e) Sheep are known to move coherently [165]. (f) Collective migrating cell sheet [166]. (g) People spontaneously ordered into 'traffic lanes' as passing a bridge in a large number [161]. (h) Self-organized vortices of vibrating granular rods [167].

the objects move together. It is still, to some extent, controversial whether this transition is continuous or discontinuous [170, 171]. Movement is the main requisite for the emergence of collective motion as it has been also seen in vibrated granular rods [167, 172, 173], disks [174], colloids [175], and other active biological systems such as cells [166, 176]. The aim of some studies, on top of the characterization of systems, is to discover universality of density fluctuations in different scales [21, 173, 177].

Collective motion is also observed at the microscopic level where dense suspensions of self-propelled bacteria at high volume fractions show organized vortices and jets in the length scales that are several orders of magnitude larger than their individual size. These organized fluid disturbances are absent in the passive systems of colloidal

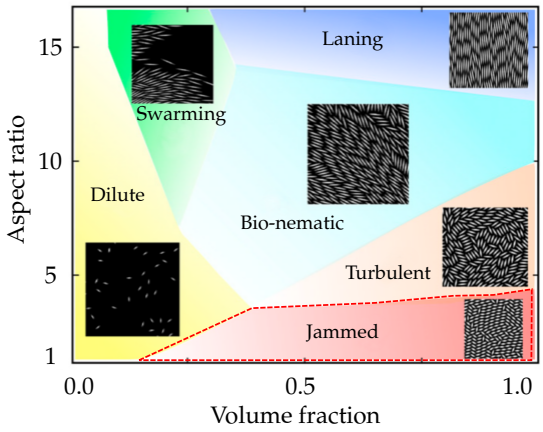

Figure 5.2: Schematic phase diagram of two dimensional self-propelled rods (SPR) exhibiting six distinct regions in the simulation. High concentrated suspensions with the aspect ratio of the swimmers close to unity turn into a jammed state that is separated by the dashed line. The image has been adopted from [183].

suspensions [178–182]. The flow of jets is similar to a flocking transition. It often becomes unstable and can even be described as 'meso-scale turbulence' [183]. Collective motion of bacteria can appear as a three dimensional phenomenon in the dense suspension of swimming cells inside the fluid or as a two dimensional one on top of the nutritious surface (see section 2.1.1). The coherent motion of bacteria in two dimensions is known as swarming, and it has been the subject of several studies [184]. Collective behavior during the swarming is physiologically different from the dense swimming bacteria in the aqueous medium, and it allows studying of the individuals precisely due to its two dimensional nature [21, 185, 186]. Bacterial systems are modeled as a dense collection of self-propelled rods on a substrate [187–189] where hard rods propel themselves along their long axis, and the short range steric repulsion due to collision between them leads to alignment and collective behavior as Vicsek model describes. Another class of models includes the fluid in which the cells are swimming and the long range hydrodynamic interactions between the cells have important effects [190]. Hydrodynamic interactions among the cells cause collective behavior in which the emerged instability depends on whether the cells push or pull themselves through the fluid [191]. Phase space of the collective behavior of swimming microorganisms has been obtained in the plane of volume fraction and swimmer's aspect ratio in the absence of hydrodynamic interactions [183] (Fig. 5.2). Most of the researches have used *B. subtilis* to characterize the ordered motion of dense bacterial suspensions where the rod-shaped morphology with large cell aspect ratio promotes the order through the steric and hydrodynamic interactions. Other species with shorter elongation such as *E. coli* have been recently investigated as well [192, 193]. Moreover, collective motion in the wild type strain of *S. marcescens* with spherical shape has been observed and compared with the similar behavior of rod-shaped cells from the same strain [194]. Investigation of swarming bacteria reveals that the statistics of collective motion depends on the aspect ratio of cells in a fundamental way [195]. Wild type strain and mutants with a similar length have the fastest motion while shorter or longer mutants exhibit anomalous non-Gaussian statistics and non-exponential decay of the autocorrelation function representing lower collective motility. Furthermore, it appears that the velocity and vorticity correlation lengths of the swarming *B. subtilis* increase with cell aspect ratio [195]. The velocity correlation length of the dense bacterial suspension increases with the swimming speed and reaches a plateau at ~40

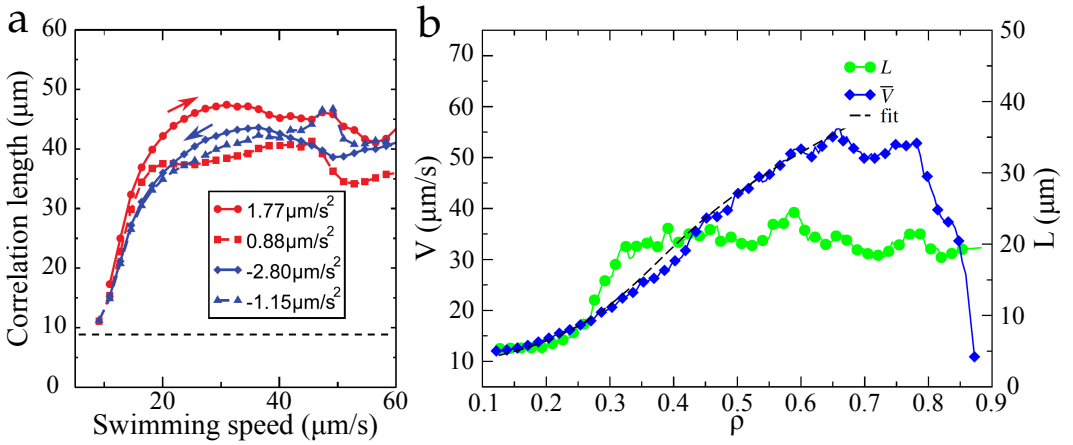

Figure 5.3: (a) Correlation length of the velocity direction as a function of swimming speed for different rates of speed changes. The arrows indicate the directions of speed variation. The speed was controlled by the oxygen concentration in the suspended film of bacteria [102]. (b) Average swimming speed V and correlation length of the velocity direction L as functions of volume fraction [179].

μm for speeds faster than 20 μm/s [102] as it can be seen in Fig. 5.3a. Sublethal antibiotics concentrations can also modify the statistics of collectively swarming *B. subtilis* in a similar manner. It leads to a heavy-tailed speed distribution as well as a two-step temporal correlation of velocity directions due to formation of non-motile subpopulations [196, 197]. The colony expansion and growth rate are not influenced by the antibiotics. Self-segregation of motility defective cells into regions has been suggested as a strategy of bacteria to fight antibiotic stress.

Some studies put forward the key question of chemical secretions that can regulate the intercellular interactions and communications which deal with another exciting problem in the context of highly concentrated bacterial suspensions [194, 198].

5.2 Motivation

While many studies have been devoted to investigating the influence of the cell concentration on different properties of the collective behavior [179, 192] (see for example Fig. 5.3b), the effect of the cell aspect ratio and the kinematic specifics of the individual swimmers have not yet been well understood [191, 199]. The interesting question that arose by considering the effect of the cell aspect ratio is whether the bacterial flagella should be included in the measurement of the aspect ratio or not. Flagella are generally not stiff enough to be considered as a part of the bacterium length at its rear inside a dense suspension of cells, but it can impose a little asymmetry in the cell shape to some extent. Some bacterial species elongate and synthesize more flagella during the two dimensional swarming motility while it is not well understood whether hyper-flagellation is an essential demand for collective motion or it is only a consequence of cell elongation [24]. It is also known that the tumbling of individual cells cannot influence the collective behavior due to collisions and cooperative motion if the corresponding noise does not dominate and continuously interrupts the rather straight cell swimming [102]. However, it has not been yet experimentally studied how the swimming properties during the run phase, such as rotational diffusion and circular swimming of the individuals, can modify the characteristic time and length scales of the coherent patterns [139, 200]. We mainly study the influence of swimming

persistency and flagellar number on the collective motion to answer the introduced questions.

5.3 Methods

5.3.1 Sample preparation

Here, the collective motion of two strains WT and swrA have been studied. ΔswrA was discarded because its culture contains a considerable fraction of filamentous and slow moving cells that cannot be effectively separated from the motile ones (see chapters 3 and 4 for the details on individual cells). The imposed noise by this type of cells dominates the collective motion and suppresses it, while in the dilute swimming regime they were simply removed by applying filters on the speed and length of the swimmers.

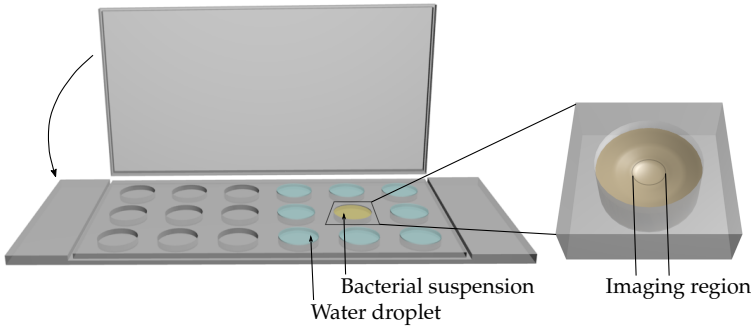

Figure 5.4: Schematic image of the sample. Around the well of bacterial suspension, several wells were filled as humidity suppliers. Images were recorded in the middle of well where the meniscus film is almost flat.

A few colonies from the fresh LB-agar plate were stirred in TB (Terrific Broth, EZMix^{TM}, Sigma Aldrich) to be grown during the night at 37 °C. The overnight culture was diluted to the optical density 0.1 and grown for about four more hours to reach the exponential phase with the optical density ~1. The swrA mutant was induced by 1 mM IPTG solution to induce hyperflagellation. Cells were first visually examined under the microscope to ensure the motility of high fraction of them. Then, 10 ml of the cell suspension in the exponential phase was pipetted into a falcon tube and centrifuged for two minutes with 4000 rpm spinning rate. The supernatant was carefully separated from the rest of suspension and the remaining pellet resuspended in fresh TB to reach 400 folds of the optical density of exponential phase. This density contains ~2×10^{10} cm^{-3} cells and corresponds to the volume fraction of ~12 percent. The pellet and TB were mixed using a vortex generator or very gentle pipetting. All the experiments were performed within the same optical density. Circular wells with 5 mm diameter and 30 μl volume (μ-Slide 18 Well-Flat, ibidi) were used as the chambers. Our samples resemble the chambers that have been already used in some other studies [193, 201, 202]. Around 12 μl of the cell suspension was transported to the well and after filling the surrounding wells with water to provide humidity, the lid was closed to reduce the evaporation rate during the experiment period (Fig. 5.4). This volume of cell suspension leads to a meniscus film of fluid with the height less than 60 μm in the middle of the well which ensures that there is no bioconvection [193]. The data reported here are based on 17 WT and 12 swrA samples that were obtained from 8 and 4 distinct cultures, respectively.

5.3.2 Microscopy

We exploited a Nikon eclipse T2000-s microscope in the bright field mode together with 50x/0.55 Nikon air immersion objective. Image sequences were recorded using a Fastec HiSpec 2G camera for 10 seconds at a rate of 100 fps in the middle of the well where the fluid surface was flat. The image and pixel size were 1120×1124 pixel and 0.28 μm. Two sets of images were recorded for each sample in the interface of air-liquid and 10 μm under the free surface where the cell concentration does not noticeably change.

5.3.3 Data analysis

The recorded images were analyzed using the common method of particle image velocimetry (see section 2.5) by PIVlab tool for Matlab [82]. Contrast limited adaptive histogram equalization (CLAHE) and two dimensional Wiener filter with respectively windows of 20 and 5 pixels width were applied on the images in the pre-processing steps for denoising. All data sets were investigated in the Fourier space by two passes of interrogation windows with 64 and 32 pixels width and 50% overlapped area. Linear interpolation was used for the window deformation, and peaks locations were estimated by a 3-point Gaussian fit to the vertical and horizontal pixels. For each set of measurements, the distributions of components of velocity vectors were visually inspected and restricted in the post-processing stage to remove the outliers. Moreover, two other filters based on the standard deviation of velocity components and the local median filter were applied to validate the vector fields. The influence of applied filters and size of interrogation windows on the results were also examined and the difference was not significant. The output vector fields after smoothing were used to calculate the correlation functions. The temporal and spatial correlation functions of the velocity directions can be obtained as,

$$C_{\mathrm{t}}(\tau) =< [\hat{u}(r,t+\tau).\hat{u}(r,t)]_{\mathrm{t}} >_{\mathrm{r}}, \tag{5.1}$$

$$C_{\mathrm{r}}(R) = [< \hat{u}(r+R,t).\hat{u}(r,t) >_{\mathrm{r}}]_{\mathrm{t}}, \tag{5.2}$$

where $\hat{u}(r,t)$ indicates the unit vector in the direction of velocity and $<>_{\mathrm{r}}$ and $[]_{\mathrm{t}}$ stand for spatial and temporal averaging, respectively. The spatial correlation function $C_{\mathrm{r}}(R)$ has been radially defined here. The distance R does not increase by equal steps size because it has been measured on the discrete grid of vector fields. Normalized temporal correlation functions of the velocity and vorticity magnitude were also calculated using the following equation,

$$J_{\mathrm{t}}(\tau) = \left\langle \frac{[\psi(r,t+\tau)\psi(r,t)]_{\mathrm{t}} - [\psi(r,t)]^2_{\mathrm{t}}}{[\psi^2(r,t)]_{\mathrm{t}} - [\psi(r,t)]^2_{\mathrm{t}}} \right\rangle_{\mathrm{r}}. \tag{5.3}$$

The function $\psi(r,t)$ can be replaced by the scaler field of the speed or vorticity [201].

Vorticity ω for a vector field $\mathbf{f}(\mathbf{r},t)$ is defined as the curl of the field. For two dimensional fields, it has only one component in the perpendicular direction to the plane of vectors. Therefore, the vorticity of the velocity vector field is in the positive or negative z direction representing counter clockwise or clockwise rotating vectors on the observation plane. A representative frame of the velocity field before extracting desired parameters is shown in Fig. 5.5a. Heatmap of $\cos\theta$ for the same vector field is plotted in Fig. 5.5b where θ is the angle of individual velocity vectors with respect to the direction of x axis. This parameter graphically shows how many cells swim to the left or right side which roughly looks equal in this frame. Heatmap of the vorticity

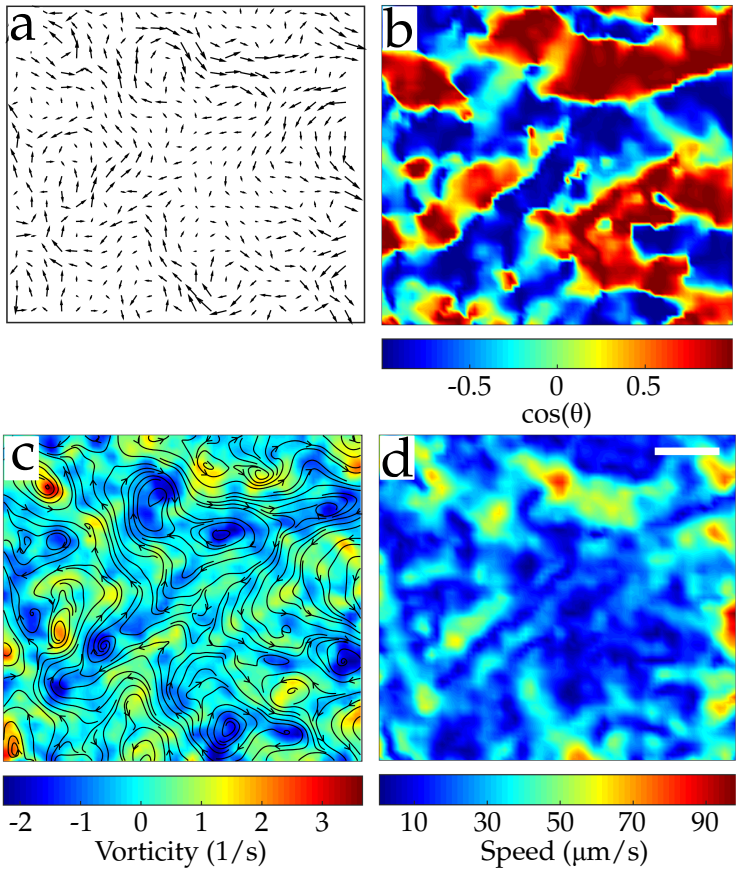

Figure 5.5: (a) An exemplary snapshot of a vector field after post processing. The density of vectors is reduced for better visualization. (b) Representative heatmap to get an impression about the direction of vectors relative to the x axis. Red and blue colors show the vectors towards the right and left sides, respectively. (c) Streamlines of the vector field are overlaid on the heatmap of vorticity. (d) Heatmap of the speed. The scale bar is 50 μm for all graphs.

along with the flow fields and also heatmap of the speed are indicated in Figs. 5.5c and d.

5.4 Results and discussion

5.4.1 Temporal evolution

Bacterial flow properties can be studied by following the literature and statistical analysis of classical turbulence [103]. Temporal evolution of the two dimensional kinetic energy $E_{xy}(t) =< (v_x^2 + v_y^2)/2 >_r$ and enstrophy $\Omega_z(t) =< \omega_z^2/2 >_r$ are plotted in Figs. 5.6a and b where ω_z is the vertical component of the vorticity. The enstrophy and kinetic energy fluctuate in a correlated manner and their temporal average over all the frames of each sample can be linearly scaled as $\Omega_z = [E_{xy}]_t/\Lambda^2$ where Λ is the length scale [103]. This scaling relation is demonstrated in Fig. 5.6c for the wild type data and the corresponding length scale is obtained as Λ~12 μm that is nearly half of the decay length of the spatial correlation function. The temporal evolution of the direction of the resultant velocity vector in each frame, Θ, that has been shown in Fig. 5.6d looks different from the fluctuation of kinetic energy and enstrophy. It appears that the global velocity direction at some time intervals is almost locked in specific directions as indicated by shaded areas on the graph.

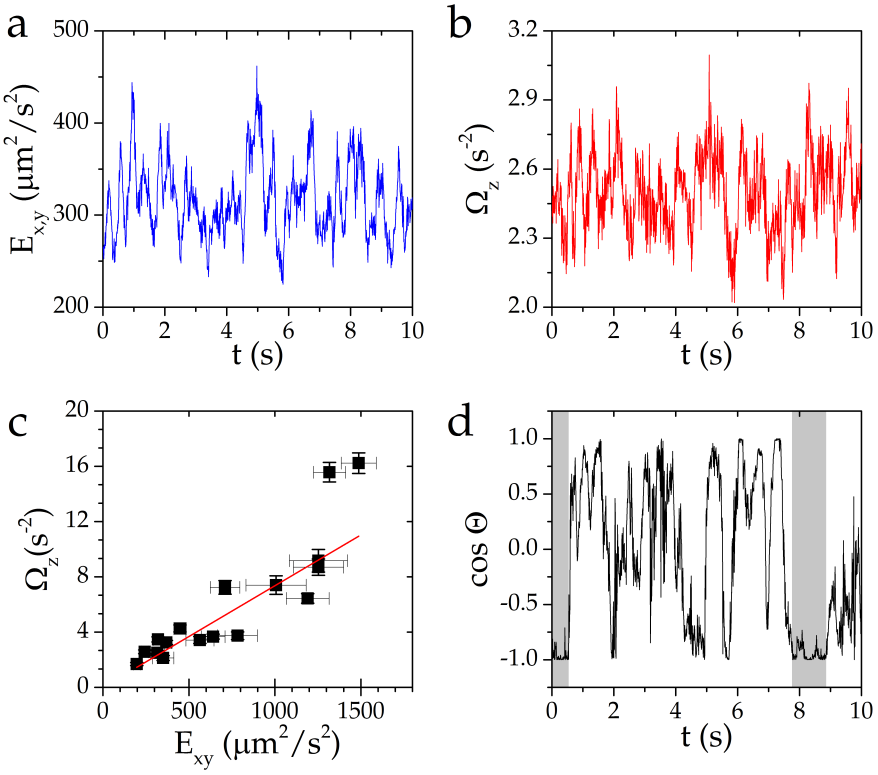

Figure 5.6: The fluctuation of (a) two dimensional kinetic energy and (b) enstrophy for one sample. (c) The temporal average of the enstrophy and kinetic energy scales linearly. The red line is a linear regression fit to the data and error bars are the standard deviations. (d) The temporal evolution of the global velocity direction is almost constant in a few intervals as shown by the shaded bars. The data are shown for wild type sample.

5.4.2 Speed and vorticity

Distributions of velocity components and speed of the velocity vector field are represented in Figs. 5.7a and b. The probability densities of velocity components are approximately Gaussian distributions where their tails are slightly wider. The scaled fourth moment of the distribution, kurtosis, was calculated to quantify the heaviness of the tail. This moment for a normal distribution has to be three but the average value for the wild type is 3.7±0.5 representing slightly broader tail of the distributions. Vorticity distributions are not also perfect normal functions and their average kurtosis is 3.6±0.5. The shapes of distributions of the other strain, swrA, qualitatively follow the same manner as wild type but their scaled moments are a little smaller. The deviation from the normal distribution can be due to the collective motion [103] or segregation of the cell population to different groups because of the variations in the swimming speed [196]. The speed probability density can be well approximated by a *Rayleigh distribution* with the form of $x\sigma^{-2}\exp\frac{-x^2}{2\sigma^2}$ where σ is the scale parameter of the distribution and indicates the mode in which the peak of the distribution is achieved. Rayleigh distributions will collapse on a master curve with $\sigma = 1$ upon rescaling by σ. Rayleigh distribution of the speed probability density relies on the approximately normal distribution of velocity components with the standard deviation of σ on the two dimensional plane [194]. The vorticity and velocity of all frames are very weakly correlated, while they show high correlation after spatial averaging over each frame (Pearson's r=0.6) as it can be seen in Figs. 5.8a and b and was also reflected in Figs. 5.6a and b. The collective motion of swimmers appears as swirls

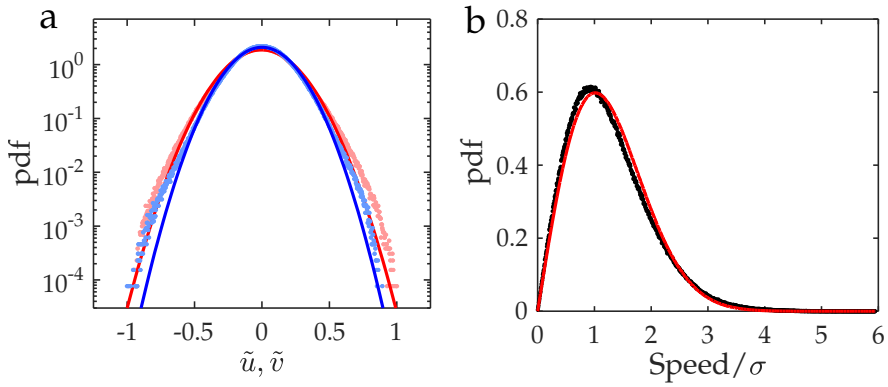

Figure 5.7: (a) Probability density of the components of velocity vectors normalized to the maximum of the absolute values in each direction. Solid lines are Gaussian fits to the data. (b) Probability density of speed for the same data along with a Rayleigh distribution fit.

and jets where groups move in a circular or rather straight path, respectively [184]. The speeds in three different vorticity ranges (terciles) were obtained for all samples

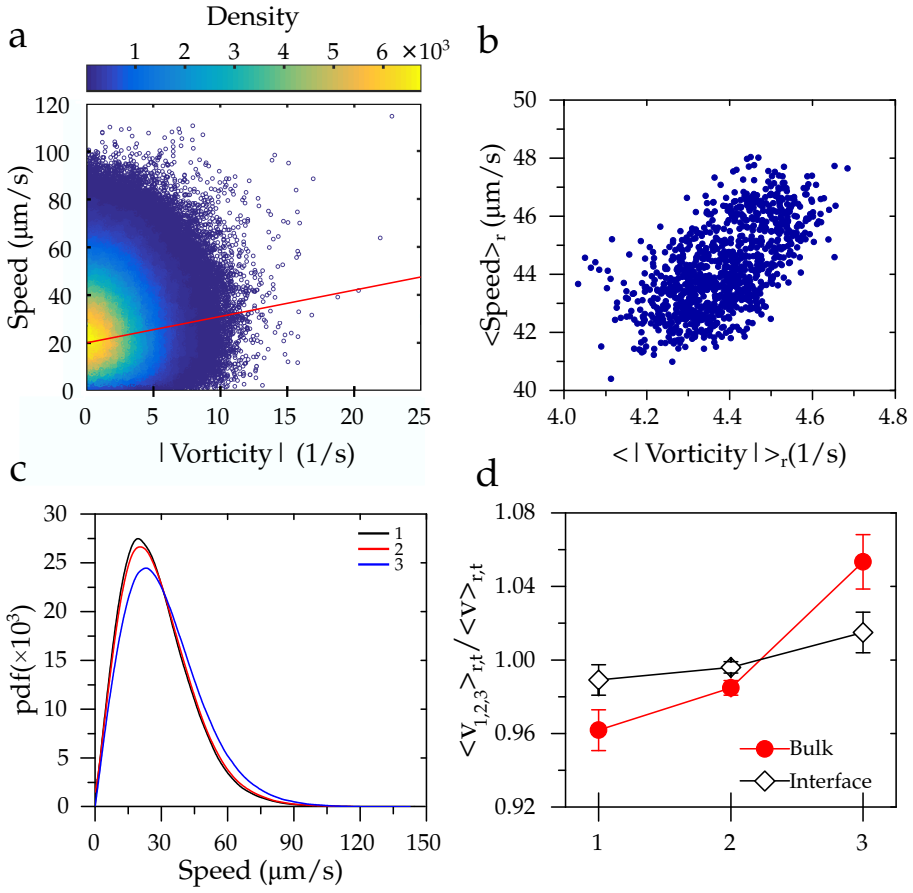

Figure 5.8: (a) Speed as a function of vorticity for all frames does not show a significant correlation as can be read out through the color-coded density of points. Data is divided into equal bins in the x and y directions to find the density of points. Solid line is a linear regression fit to the data. (b) Average speed and vorticity per frame are highly correlated. (c) Probability density of speeds in the various parts of the vorticity terciles. (d) Normalized average speeds in the first, second, and third part of the vorticity terciles in the bulk and interface.

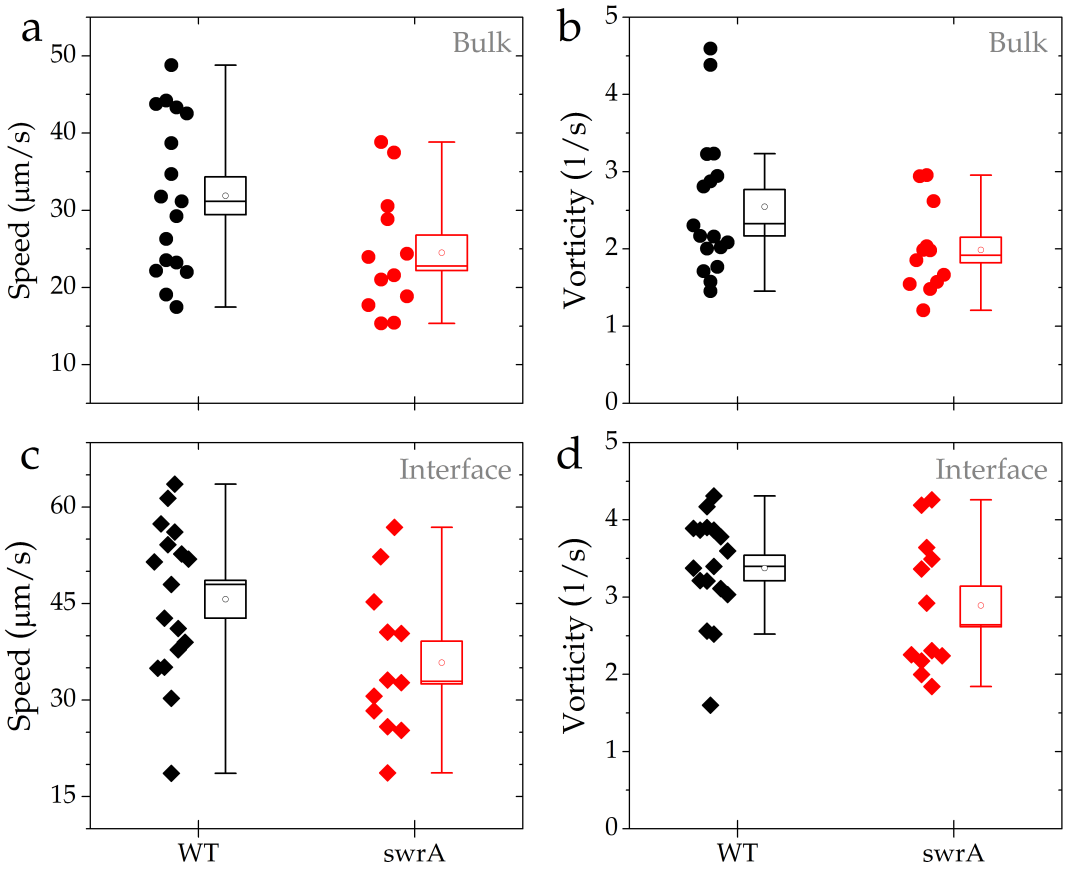

Figure 5.9: (a,b) Speed and vorticity in the bulk and (c,d) interface of air-liquid. The speed of wild type is statistically faster than swrA while the vorticity is similar for both strains. The speed and vorticity of each strain in the interface are significantly higher than the bulk region.

and exemplary probability distributions are represented in Fig. 5.8c. The normalized average speed in the bulk continuously increases from the first to the third part of the tercile indicating cells swim faster inside the swirls rather than inside the jets. The trend of swimming cells in the interface is the same but according to the results of t-test the difference is not significant (Fig. 5.8d).

The strains that were studied have different effective aspect ratio considering the bundles according to the fluorescence experiments. Longer cells can promote alignment and have some advantages in the collective motion [195]. The average speed and vorticity for all samples of both strains are delineated in Fig. 5.9 as box plots. The average speed of the wild type which has a little higher aspect ratio is larger than the average speed of swrA mutant in the bulk and also in the free surface of suspension. Moreover, cells swim on the surface faster than in the bulk in each sample of every strain, and the speed difference is substantial according to the t-test with the significance level of 0.05. It has been discussed in the literature that a higher cell aspect ratio can raise the speed of collective motion [195], but here the different speed of strains cannot be solely attributed to this fact because the average speed of individual cells of the wild type was also higher than the swrA mutant (see Fig. 3.7a). Therefore, the impact of swimming persistency of individual cells cannot be disentangled from the impact of cell's aspect ratio especially because in this case, they both can modify the swimming speed of collective motion in the same direction. Regarding the swimming cells in the interface of air-liquid, from the one hand, their bodies are aligned on the two dimensional surface and their interactions increase

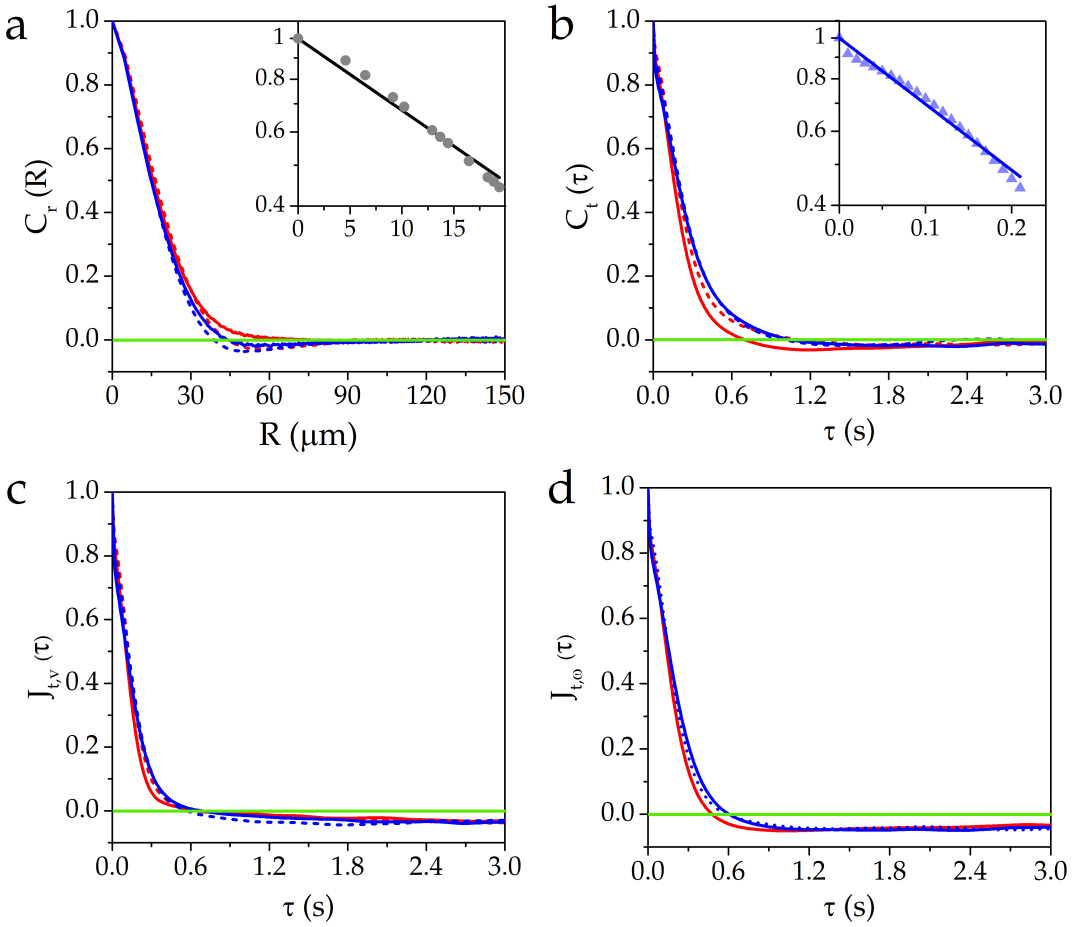

Figure 5.10: (a) The spatial and (b) temporal correlation functions of the velocity directions for both strains in the bulk and interface of air-liquid. Insets show an exemplary exponential fit to the data of wild type inside the suspension in the semi-logarithmic scale. (c) Temporal correlation functions of the speed and (d) vorticity magnitude. Each curve is an ensemble average over all samples. Red (blue) curve corresponds to WT (swrA) strain and solid (dashed) curve belongs to the measurements in the bulk (air-liquid interface).

due to the excluded volume effect. On the other hand, the bundles of cell tend to be aligned with the cell body and the opening angle between them likely decreases because of the interaction with the boundary [203]. This interaction in the individual cell level leads to a non-trivial rise of the speed even close to the solid surface with no slip boundary condition, while one may expect a reduction in the speed because of the enhanced drag force. The impact of oxygen gradient close to the surface can be neglected due to the shallow depth of the samples. It seems the variation of speed is governed by the reduction of opening angles between the bundles of individual cells rather than the effective alignment of the cell bodies. We discuss in the next section that the size of vortices does not change on the surface in comparison to the bulk.

The averages of vorticity values follow the trend of speed. The vorticity is in general larger for wild type cells and for each strain a higher vorticity can be achieved on the surface (see Figs. 5.9b and d). Only the difference of vorticity between the interface and the bulk regions for each strain is significant according to the t-test. The similar tendency of the speed and vorticity is due to their correlation as was shown in Fig. 5.8b.

5.4.3 Characteristic time and length

The most important features of the collective motion are characteristic length and time scales. They can be obtained using the spatial and temporal correlation functions that were introduced in section 5.3.3. Time and length scales can be estimated by diverse ways such as an exponential fit, finding the first minimum of the curve, and the point where the curve drops below zero. One should keep in mind that all these methods will not give the same values and they can be interpreted in different ways. All the results that have been presented here are based on the fit $C_t(\tau)=\exp(-\frac{\tau}{\tau_0})$ and $C_r(R)=\exp(-\frac{R}{\lambda})$ to the data. It has been already reported that swarming bacteria can show anomalous statistics with a two-step decay of temporal correlation function of the velocity direction [196]. This feature has been associated to the immotile subpopulation that self-segregates into regions as systems of active Brownian particles can be divided into two phases with different speeds [197]. Segregation can also be observed in the binary mixture of granular spheres colliding 'inelastically' that resembles more to the bacterial interactions [204]. Spatial and temporal correlation functions of the velocity direction are shown in Figs. 5.10a and b. All curves drop to the minus values. The spatial correlation functions of some samples of swrA strain develop rather deep valleys representing the strong anti-correlation of the velocity direction due to the vortex formation. This behavior cannot be seen in the temporal correlation functions, even though they are anti-correlated in the long intervals most likely due to the translation of vortices. The overall temporal correlation of vorticity and velocity magnitude are plotted in Figs. 5.10c and d.

The characteristic lengths of the spatial correlation of velocity directions λ in the bulk and interface are presented in Figs. 5.11 a and c, respectively. The length scale in the bulk is ~25 μm which is almost three times the length of a bacterium. This length is smaller than 40 μm of the vortex size that was obtained as the first minimum of the curves in Fig. 5.10a. The values in the interfaces are also in the same range, and there is no statistical difference neither among the strains nor among the bulk and interface. Transportation properties of a single bacterium of different strains inside the fluid do not modify the characteristic length scales of collective motion (the diffusion coefficients of the strains differ by a factor of two). The typical size of vortices in the air-liquid interface of the dense suspension of both strains is similar while the average radius of circular trajectories of the wild type was twice swrA in the dilute suspensions (see Fig. 3.22b). Interestingly, even considering a very extreme condition of circular swimmers on the surface and rather random motion of individuals in the bulk approximately yield equal results. The correlation length is nearly constant for the swimming speeds faster than around 20 μm/s (see Fig. 5.3a). It also seems to be independent of the single cell persistency, effective ratio of the cell, and flagellar number in the range of our experimental values. The decay times of the temporal correlation of velocity directions in the bulk and interface for both strains are statistically similar, and one can consider 0.27 s as the overall estimate (see Figs. 5.11b and d). The only significant difference is between the decay times of the wild type in the bulk and interface (p-value=0.022). The striking feature is that there is no preference in the vorticity direction of the swirls on the surface although individual bacteria swim in a counter clockwise manner in the air-liquid interface. It is not directly clear whether the different observation planes are influenced by each other or not due to the two-dimensional velocity field. We reduced the height of the suspensions below 100 μm to suppress the bioconvection and large up-down movement of the cells, and thus we assume various layers are just weakly affected by each other. Therefore, the observed similarities between the focal planes in the bulk and interface

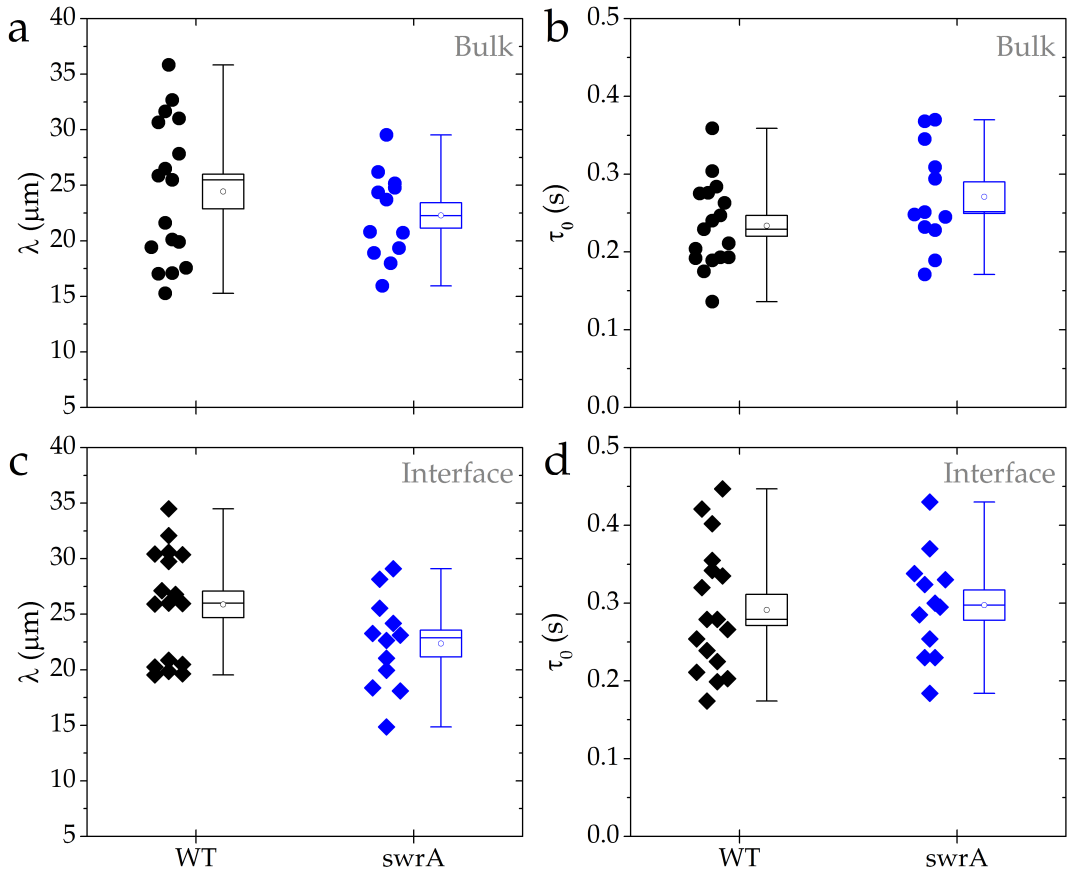

Figure 5.11: (a,b) Characteristic length and time scales in the bulk and (c,d) interface of air-liquid. There is no statistical difference between the strains in the bulk and interface regions.

are not because of the strong interaction between the layers, otherwise the speed should also be the same.

It had been suggested that the correlation length of the collective motion is governed by the geometrical shape of swimmers [102] but recent investigations of spherical and rod-shaped cells of the same strain revealed that the correlation length and time are not influenced by the cell shape [194]. The latter study also proposes the dominant contribution of chemical secretion or physical properties of the medium such as viscosity in the appearance of collective motion instead of the cell geometry. In principle, the chiral motion can be due to two reasons: anisotropy in the particles shape which leads to a hydrodynamic coupling of translation and rotation or anisotropy in the propulsion mechanism itself [139]. These mechanisms can also simultaneously influence the motion for example in the chiral trajectories of L-shaped swimmers [205]. Swimmers that are moving together due to hydrodynamic interactions or collisions can lead to a situation in which the cluster center experiences non-vanishing torque [206]. The specific torque on the swirls and jets of bacteria imposed by their particular geometry and size can cause the same collective behavior independent of the shape or trajectory of single cells.

5.4.4 Diffusion of numerical tracers

Following individual bacteria can be difficult inside the dense suspensions [192]. The common alternative approach of PIV to quantify such dense systems is the tracking

of tracer beads in the suspension [103, 207–211]. Trajectories of the numerical tracers have been studied here to confirm some results of the collective motion. The reported values can be directly examined by tracking real tracer beads in the suspension since it has been shown that the numerical and real tracers yield the same result [186].

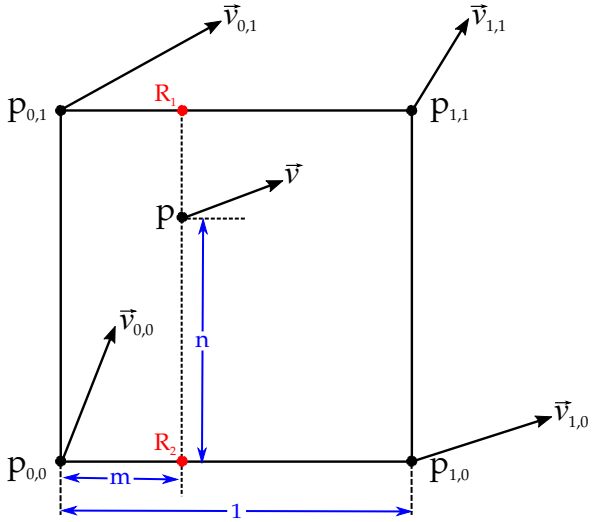

Figure 5.12: Schematic illustration of the bilinear interpolation of the velocity on a rectilinear grid.

Vector fields of each measurement have been used to follow the path of 500 numerical particles through the frames. Tracers randomly were sampled in the middle of the field of view to achieve temporally long trajectories. The corresponding velocity vector in the selected point has been obtained based on 'bilinear interpolation' [212]. This interpolation through an image is graphically equivalent with zooming in the image. The principle of the method is schematically demonstrated in Fig. 5.12 where the aim is to find the velocity vector in point p using the surrounding velocities in the corners of the grid. The components of the velocity vector are first interpolated in R_1 and R_2 and then the results are used to estimate the vector components in p. It can be shown that the interpolated vector in p can be written as [212, 213],

$$\mathbf{v} = (1-n)(1-m)\mathbf{v}_{0,0} + (1-n)m\mathbf{v}_{1,0} + n(1-m)\mathbf{v}_{0,1} + mn\mathbf{v}_{1,1}. \tag{5.4}$$

The interpolated velocity vector and initial point were used to solve the ordinary differential equation (ODE) by Euler's method and find the position of tracer in the next frame. This procedure was continued through all frames. Trajectories of the tracers were employed to measure the MSDs, translational diffusion coefficients, and characteristic decay times as was performed in section 3.3.4.

The imaginary tracers pursue the motion of swirls and jets, and sometimes they instantly switch between different swirls. The trajectories are consequently very curved paths that can also follow small closed loops or experience large directional changes as shown in Fig. 5.13a. The equation 2.34 was fitted to the MSD curves to obtain the effective decay time τ_e and translational diffusion coefficient D. Scaled MSDs of the various samples can collapse on a master curve $f(x) = x - 1 + \exp(-x)$ upon dividing by MSD$/(4D\tau_e)$ and τ/τ_e (see Fig. 5.13b). Tracers follow the pathlines of jets and swirls. Thus, their persistency in the short time limits has a characteristic time in the order of lifetime of jets and swirls. The motion in this regime is assumed to be ballistic although superdiffusive behavior has been observed as well [210]. The direction of trajectories continually varies because of the exchange between different

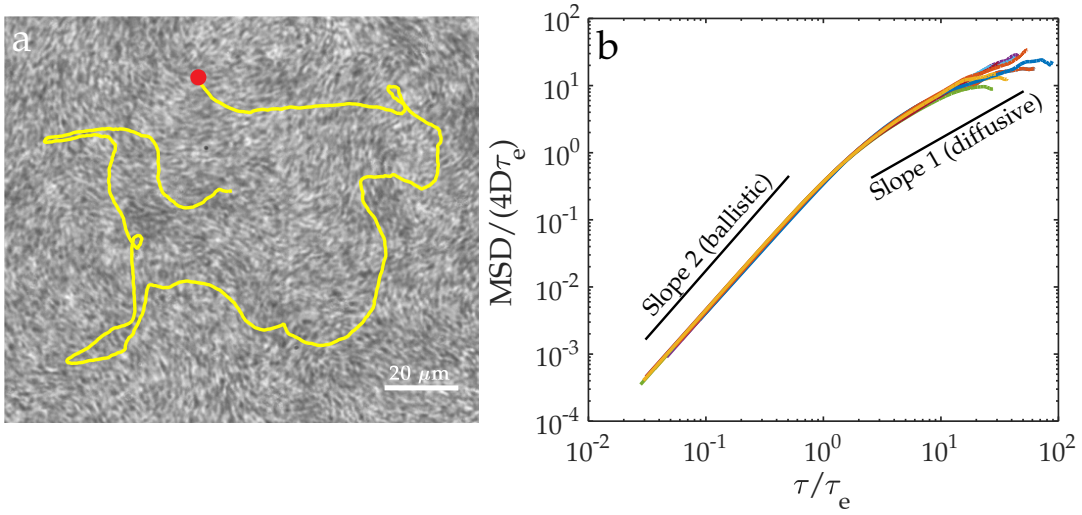

Figure 5.13: (a) An exemplary trajectory of a numerical tracer. It starts from the red point and lasts for 10 s in the middle of the field of view. (b) The normalized MSDs and lag times for different samples collapse on a master curve.

swirls and the motion becomes random in long time limit. The characteristic decay times and translational diffusion coefficients are delineated in Fig. 5.14. The difference in decay times in the bulk between two strains are significant, and there is a borderline statistical trend (p-value=0.0473) between the time scales of the wild type in the bulk and interface. The characteristic time scales of the numerical tracers are in the same order of magnitude as the decay times of the velocity directions. Only the diffusion coefficients of the wild type in the bulk and surface are statistically distinct. The diffusion coefficient of freely swimming wild type bacteria is around five times of swrA strain while this ratio is not the same for the diffusion coefficients of the numerical tracers neither in bulk nor the interface. Moreover, the diffusion coefficient of tracers in the dense suspension of the wild type strain is one order of magnitude smaller than freely swimming wild type cells representing restricted motion because of vortex formation. Measurement of the diffusion coefficients of the passive beads with the diameter of 4.5 μm and 10 μm in the same range of bacterial density gives smaller values [210] than what was obtained here. The size of tracers practically influences the diffusion properties by modifying the drag force. The equivalent size of a passive tracer with the same diffusion coefficient that was obtained here is in the order of picometer. Therefore, it appears that numerical tracers without any hydrodynamic resistance pursue the path of active swimmers and flow lines. Following the Eq. 2.35 velocity of the tracers can be written as $v = \sqrt{2D/\tau_e}$ and the characteristic length $l_c = v\tau_e = \sqrt{2D\tau_e}$ can be defined which in the bulk is around 9 μm for the wild type and 11 μm for the swrA strain. These length scales are roughly half of the vortex size λ that was obtained using the decay length of the velocity directions at the constant times. One should keep in mind that these length scales are intrinsically distinct. The former is over the time representing how far a typical vortex can be transported and also shows to what extent a bacterium can move persistently. The latter is over individual frames where the time is fixed and it indicates the size of vortices. The persistent length l_c for both strains is approximately the same while the average run length of the wild type in the space was twice of swrA (see Fig. 3.8a). Furthermore, the length of run segments of wild type and swrA were respectively around 60 μm and 30 μm that is considerably larger than l_c values. This indicates the fact that individual bacteria in a dense suspension cannot freely select their moving direction and instead

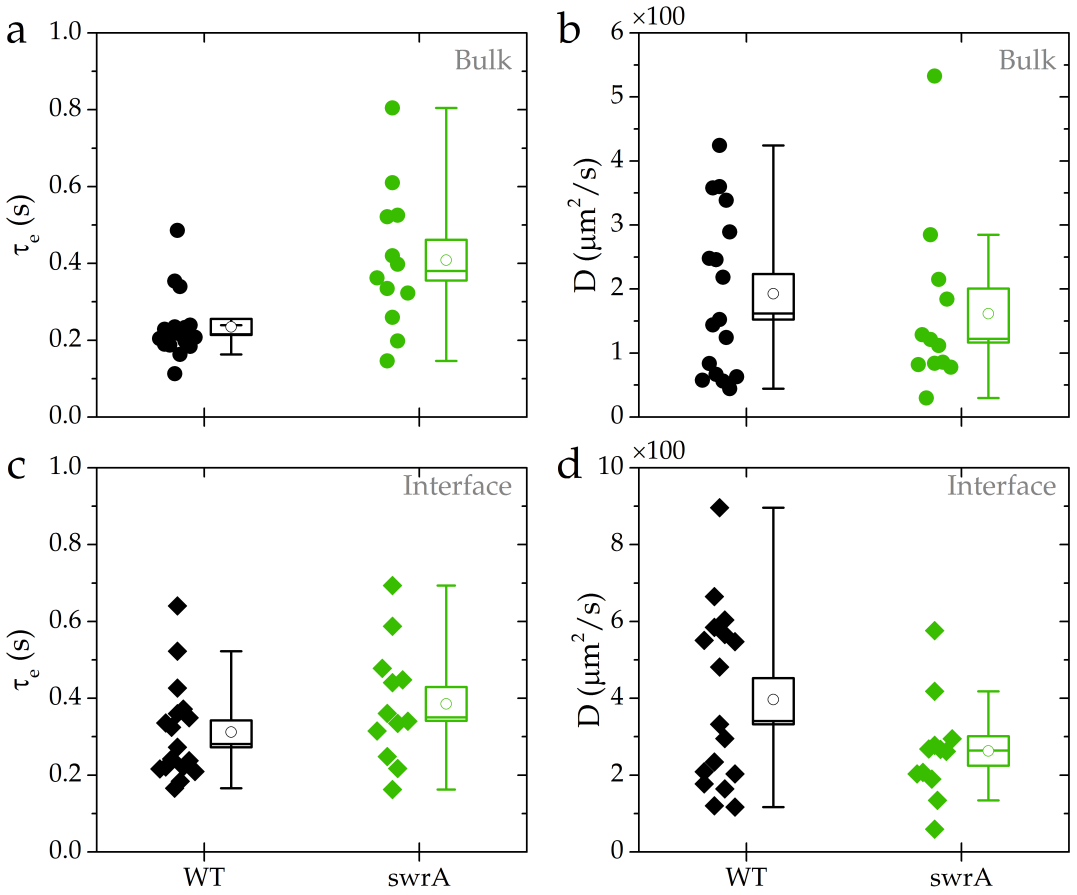

Figure 5.14: (a,b) Characteristic decay times and diffusion coefficients of the numerical tracers in the bulk and (c,d) interface of air-liquid. The decay times of the strains in the bulk and diffusion coefficients of the wild type in the bulk and interface are statistically different according to the t-test with the significance level of 0.05.

follow the path of swirls. The traditional run and tumble motion is not applicable in such a situation due to frequent collisions, and the persistency of trajectories are shorter than the run segments.

5.5 Summary

We studied collective behavior to figure out how the persistency of the individual swimmers and their effective aspect ratio comprising the bundles can impact coherent motion of cells. The groups of wild type strain with a larger aspect ratio of cells and higher persistency than swrA mutant are faster, but we could not unwind the contribution of these parameters, mainly because the individual wild type cells also have higher swimming speeds. The spatial average vorticity and speed per frame are correlated, and groups of cells in the vortices swim faster than jets. The average characteristic decay time and length of the temporal and spatial correlation functions of the velocity directions are almost the same. The decay length and time are respectively 25 μm and 0.25 s. Interestingly, we did not find a significant difference between the swimming cells in the bulk and air-liquid interface. Even the chiral motion of the individual cells in the interface could not bias the vorticity of collectively moving cells, and the distribution of vorticity has always left-right symmetry. We sampled hundreds of numerical tracers in the middle of the field of view and investigated their

trajectories. They follow the pathlines of swirls and jets in the short time limit in a persistent manner which appears as a ballistic phase in the MSD curve. The motion turns into a diffusive phase in the long time limit when the tracers frequently switch between the swirls or jets. The transition time indicates the lifetime of swirls and is approximately equal to the decay time of the velocity directions. It comes out from our measurements that to a reasonable extent the collective motion of bacteria is robust against the kinematic of individual swimmers, and it appears the chirality of individuals cannot influence the motion of cells as the groups. The other crucial geometrical parameter governing the collective motion beside the shape of individual swimmers could be the size and geometry of clusters and co-moving groups of cells as they can affect the torque imposed on the group as a whole.

6

Conclusion and Perspectives

Conclusion

We studied *B. subtilis* as a model system of microswimmers from the individual cell level to the collective motion. The central goal was to understand the impact of the flagellar number on several fundamental swimming parameters. The results can be summarized as the following.

• In the single cell level, we studied the influence of flagellar number on different swimming parameters. We mainly figured out that increasing number of flagella is not beneficial for swimming speed, but it enhances rotational diffusion, turning angle after tumbling, and wobbling angle. The run time reduces with the number of flagella which supports the 'veto model' for tumbling. Accordingly, cells with higher number of flagella are less persistent during the run phases and tumbling events that decreases corresponding translational diffusion of cells. The experimental results were confirmed by an analytical and numerical two-state random walk model, and the phase spaces of the translational diffusion in the planes of practically relevant parameters were obtained. The variation of persistency during the run phases, i.e., rotational diffusion, in the range of experimental parameters can mainly modify dispersion properties. We performed Monte Carlo simulations of the random searchers and calculated the mean first passage time as a function of the persistency during the run phase. The optimum persistency minimizes the search time and monotonically increases with the size of the search environment. Therefore, many flagella are advantageous for the local search while fewer flagella are beneficial for the long distance search. Wild type cells with intermediate persistency (flagellar number) can have the optimum global search efficiency in short and long distances.

• We investigated the dynamics of bundle formation in *B. subtilis* bacteria to get insight into their swimming kinematics. We confirmed the formation of multiple bundles during the run phase and for the first time quantified bundles characteristics. The number of bundles that each mutant can make is independent of the flagellar number. The most probable number of bundles is always three likely due to the similar cell body length. The projected angle between the bundles on the observation plane increases with the number of flagella, i.e., the effective aspect ratio of cells including bundles decreases. Run speed drops with increasing projected angles between the bundles for each strain. Cells with elongated body qualitatively make several side bundles, and accordingly, we primarily assign the formation of numerous bundles to the geometrical restriction because of the long body length of *B. subtilis*. The number

of bundles for each bacterium is not strictly defined, and it can remarkably vary from one run phase to another.

• We studied the collective behavior of cells to unravel the influence of persistency of individual swimmers, and their effective aspect ratio comprising the bundles, on the coherent motion of cells. The groups of wild type cells with larger aspect ratio and higher persistency than swrA cells are faster, but we could not disentangle the contribution of aforementioned parameters. The average decay time and length of the temporal and spatial correlation functions of the velocity directions are almost the same. The decay length and time are respectively 25 μm and 0.25 s. Coherent cells in the interface of air-liquid swim faster while we could not find any other significant difference. The distribution of vorticity always has left-right symmetry in the air-liquid interface which contrasts to the chiral motion of individual cells in dilute suspensions. We also investigated the trajectories of numerical tracers and showed that their movement consists of ballistic and diffusive phases. The transition time represents the lifetime of swirls and agrees with the decay time of velocity directions. It appears from our results that to a great extent the collective motion of bacteria is independent of some properties of individual swimmers such as their persistency and flagellar number.

Perspectives

I studied various topics on microswimmers during my research which due to the limited time, some of them were left unfinished or just remained as an idea. In the next steps of this thesis, the following works can be done.

• **Swimming in non-Newtonian fluids.** To the best of our knowledge, the swimming of bacteria with a various number of flagella (in particular peritrichously flagellated bacteria) has not been systematically studied in non-Newtonian fluids. For this purpose, different polymeric solutions such as PVP[1], PEG[2], CMC[3], and XG[4] with various molecular weight and radius of gyration can be employed with different concentrations [129, 214]. The swimming parameters of the strains can be linked to the rheological properties of the solutions. Swimming speeds and run-tumble statistics can be measured in the different solutions and compared to the performance of the strains in Newtonian fluid regarding the influence of the flagellar number. The strain with a higher number of flagella can insert more shear forces around the cell body which in shear thinning polymeric solutions leads to a locally lower viscosity. This can increase the speed of cells and cause significant differences in their behavior.

• **Chemotaxis.** Chemotaxis is at least as crucial as motility and cell growth rate in the evolutionary competition. Thus, the chemotaxis system is expected to be highly optimized as it has been indeed suggested by several studies [215, 216]. An appropriate microfluidic device can be designed to practically study the efficiency of the chemotactic response in the presence of chemical gradients inside the microchannel. The microchannel can consist of two separate chambers that one should be filled with chemo-attractant, e.g., aspartate, serine [9], and the other one with the bacterial suspension. The chambers are connected by a narrow channel creating a gradient of attractant in the connecting channel by diffusion. The concentration of the chemical

[1] Polyvinylpyrrolidone
[2] Poly-ethylene glycol
[3] Carboxy-methyl cellulose
[4] Xanthan gum

at each point between the chambers can be obtained as a function of time by solving the diffusion equation. The bacteria sense and immigrate towards the nutrient, and their movement can be characterized inside the connecting channel. One can measure the same parameters as mentioned in section 3.4.1 that among the others includes the drift velocity as a function of chemical concentration. The drift velocity gives an overall gauge to compare the efficiency of chemotaxis between different strains. To disentangle the impact of the different swimming parameters on the chemotaxis, one can recalculate the run and tumble-related quantities that were studied in the homogeneous environment. On the one hand, it has been already reported that bacteria can modify their running time [9] and directional persistency [123] to swim up-gradient. On the other hand, there are some remarks in the literature that increased flagellar number can improve the chemotactic efficiency by increasing the turning angle [43]. Our tracking results indicate that cells with more flagella tend to swim in a restricted manner. This outcome together with the analytical arguments in section 3.4.4 leads to the contrary conclusion that cells with more flagella have worse chemotactic performance. The response from the different strains can practically be more complicated and not follow the same manner. For example the strain with higher flagellar number can correct efficiently its swimming direction due to its more substantial freedom in selecting the new direction after tumbling if it can bias the turning angle in a controllable way. Some experiments have to be done on the mutants with the different flagellar number in the presence of chemical gradients to resolve this discrepancy.

• **Bundle configuration in the dense suspension.** There was no significant difference in the collective motion of cells even though they had various flagellar numbers and aspect ratios. The critical point that can help to figure out the role of flagellar bundle in the collective motion is their direct observation in the dense suspension. The bundle and the trajectories of *E. coli* in the two dimensional swarm have been qualitatively described, and four kinds of tracks have been distinguished [217]. Collective motion in the swarming form is somehow different from the coherent movements in the dense suspension as discussed in sections 2.1.1 and 5.1. The preliminary question arising with the swimming *B. subtilis* cells in the dense suspension is whether they can make several bundles in such a crowd environment or not. It surprisingly appears they are still able to form multiple bundles according to the early experiments that I performed. How does the suspension density and collision with neighbor bacteria impact the bundle arrangement? Is there any difference between the bundle configurations in the bulk and air-liquid interface? Simultaneous observation of the body and bundle during the collective motion can also give further insights into the propulsion mechanism and bundle alignment relative to the cell body in the dense suspension. Trajectories of the cell body can be used to examine the numerical trajectories that were discussed in section 5.4.4.

• **Biofilm formation.** One of the exciting features of *B. subtilis* during the swarming is the secretion of a kind of biological surfactant known as 'surfactin'. It lubricates the surface and facilitates the movement of bacteria on the solid agar surface. We examined that different concentrations of surfactin do not vary the swimming speeds of wild type cells. Some studies show that surfactin is also involved in the biofilm development on the agar surface [218–220]. During my research, some efforts have been put to grow few biofilms and start to quantify them in collaboration with Dr. Sigolene Lecuyer at LiPhy lab in Grenoble. The primary goals were to study the impact of surfactin concentration and gradient on the biofilm growth rate and morphology. Despite the challenge in controlling the humidity of the growth chamber and sensitivity

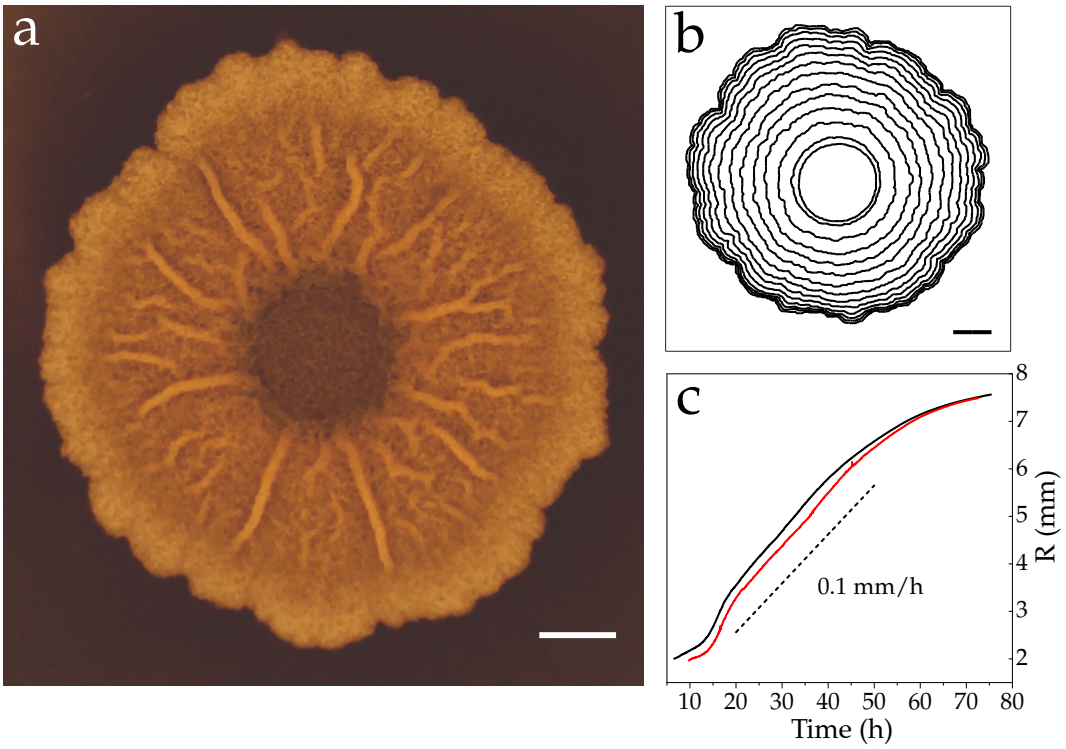

Figure 6.1: a) Typical biofilm pattern after three days of incubation at 30 °C. b) Tracking the proceeding front with 5 hours time lag between two subsequent contours. c) The growth rate in the middle phase is 0.1 mm/h and afterwards it decreases. The scale bars are 2 mm.

of the biofilm morphology to the composition of the growth medium (see Appx. B for the details), a few trials were successful, and some control measurements have been done as represented in Fig. 6.1. The main ideas are to investigate how the surfactin concentration and gradient can modify the growth rate and principle morphological features such as front roughness and topology of the height. The other interesting object can be studying asymmetrically grown patterns by imposing extragenic surfactin gradient [221].

A

Analytical Approach

To describe the persistent motion of bacteria interrupted by stochastic tumbling periods, we developed an analytical framework for a random walker with two states of motility, as described by the set of master Eqs. 3.4. In the following, we briefly explain how arbitrary moments of displacement can be obtained by a Fourier-z-transform technique. Here, a two-dimensional motion is considered but extension to three dimensions is straightforward. The Fourier transform of $P_t^j(x,y|\gamma)$ is defined as

$$P_t^j(\boldsymbol{\omega}|m) \equiv \int_{-\pi}^{\pi} \mathrm{d}\gamma\, e^{im\gamma} \int \mathrm{d}y \int \mathrm{d}x\, e^{i\boldsymbol{\omega}\cdot\boldsymbol{r}} P_t^j(x,y|\gamma), \tag{A.1}$$

with $j\in\{R,T\}$. An arbitrary moment of displacement $\langle x^{k_1} y^{k_2}\rangle^j(t)$ can be obtained as

$$\langle x^{k_1} y^{k_2}\rangle^j(t) \equiv \int \mathrm{d}\gamma \int \mathrm{d}y \int \mathrm{d}x\; x^{k_1} y^{k_2} P_t^j(x,y|\gamma) \tag{A.2}$$

$$= (-i)^{k_1+k_2} \frac{\partial^{k_1+k_2} P_t^j(\omega_x,\omega_y|m{=}0)}{\partial\omega_x^{k_1}\partial\omega_y^{k_2}}\bigg|_{(\omega_x,\omega_y)=(0,0)}. \tag{A.3}$$

The master Eqs. 3.4 after Fourier transformation read

$$\begin{aligned} &P^R_{t+\Delta t}(\omega,\alpha|m) = \\ &\sum_{k=-\infty}^{\infty} i^k\, e^{-ik\alpha}\, J_k(\omega\, v_{\mathrm{R}}\Delta t)\Big[f_{\mathrm{T}\to\mathrm{R}}\, \mathcal{R}(m{+}k)\, P_t^T(\omega,\alpha|m{+}k) \\ &+ (1{-}f_{\mathrm{R}\to\mathrm{T}})\, p(m{+}k)\, P_t^R(\omega,\alpha|m{+}k)\Big], \end{aligned} \tag{A.4}$$

$$\begin{aligned} &P^T_{t+\Delta t}(\omega,\alpha|m) = \\ &\sum_{k=-\infty}^{\infty} i^k\, e^{-ik\alpha}\, J_k(\omega\, v_{\mathrm{T}}\Delta t)\Big[f_{\mathrm{R}\to\mathrm{T}}\, P_t^R(\omega,\alpha|m{+}k) \\ &+ (1{-}f_{\mathrm{T}\to\mathrm{R}})\, P_t^T(\omega,\alpha|m{+}k)\Big], \end{aligned} \tag{A.5}$$

where we used the kth order Bessel's function

$$J_k(z) = \frac{1}{2\pi i^k} \int_{-\pi}^{\pi} \mathrm{d}\gamma\; e^{iz\cos\gamma} e^{-ik\gamma}, \tag{A.6}$$

the Fourier transforms of the turning-angle distribution

$$\mathcal{R}(m) = \int_{-\pi}^{\pi} \mathrm{d}\phi \; e^{im\phi} R(\phi), \tag{A.7}$$

and the distribution of the directional change along the run trajectory

$$p(m) = \int_{-\pi}^{\pi} \mathrm{d}\theta \; e^{im\theta} R(\theta). \tag{A.8}$$

The Fourier transform of the probability $P_t^j(\omega, \alpha|m)$ can be expanded as a Taylor series

$$\begin{aligned} P_t^j(\omega, \alpha|m) = Q_{0,t}^j(\alpha|m) + i\,\omega\, v_{\mathrm{j}} \Delta t \; Q_{1,t}^j(\alpha|m) \\ - \frac{1}{2}\omega^2 \, v_{\mathrm{j}}^2 (\Delta t)^2 \; Q_{2,t}^j(\alpha|m) + \cdots, \end{aligned} \tag{A.9}$$

and the moments of displacement can be read in terms of the Taylor expansion coefficients. For example,

$$\langle x^2 \rangle^j(t) = v_{\mathrm{j}}^2 (\Delta t)^2 \, Q_{2,t}^j(0|0). \tag{A.10}$$

Thus we expand both sides of the master equations A.4 and A.5 and collect all terms with the same power in ω. As a result, coupled recursion relations for the Taylor expansion coefficients of terms with the same power in ω can be obtained. Next, the time indices on both sides of these equations can be equalized by means of z-transform, which enables us to obtain the moments of displacement in the z-space. For example, one obtains the following exact expression for the mean square displacement

$$\begin{aligned} &\langle x^2 \rangle(z) = \sum_{t=0}^{\infty} z^{-t} \langle x^2 \rangle(t) = \\ &(\Delta t)^2 \Big[v_{\mathrm{R}}^2 Q_2^R(z, 0|0) + v_{\mathrm{T}}^2 Q_2^T(z, 0|0) \Big] = \\ &(\Delta t)^2 \Big[(1 - f_{\mathrm{R}\to\mathrm{T}}) Q_0^R(z, 0|0) + f_{\mathrm{T}\to\mathrm{R}} Q_0^T(z, 0|0) \Big] \times \\ &\left[\frac{z\left[z - (1 - f_{\mathrm{T}\to\mathrm{R}})\right]}{(z-1)G(z)} v_{\mathrm{R}}^2 + \frac{z}{(z-1)G(z)} f_{\mathrm{R}\to\mathrm{T}} \, v_{\mathrm{R}} v_{\mathrm{T}} - \frac{1}{2(z-1)} v_{\mathrm{R}}^2 \right] \\ &+ (\Delta t)^2 \Big[f_{\mathrm{R}\to\mathrm{T}} Q_0^R(z, 0|0) + (1 - f_{\mathrm{T}\to\mathrm{R}}) Q_0^T(z, 0|0) \Big] \times \\ &\left[\frac{z\left[z - (1 - f_{\mathrm{T}\to\mathrm{R}})p\right]}{(z-1)G(z)} v_{\mathrm{T}}^2 + \frac{z}{(z-1)G(z)} f_{\mathrm{T}\to\mathrm{R}} \, \mathcal{R} \, v_{\mathrm{R}} v_{\mathrm{T}} - \frac{1}{2(z-1)} v_{\mathrm{T}}^2 \right], \end{aligned} \tag{A.11}$$

where

$$G(z) = \left[z - (1 - f_{\mathrm{T}\to\mathrm{R}})\right]\left[z - (1 - f_{\mathrm{R}\to\mathrm{T}})p\right] - f_{\mathrm{R}\to\mathrm{T}} f_{\mathrm{T}\to\mathrm{R}} \, \mathcal{R}. \tag{A.12}$$

By inverse z-transforming the moments of displacement in the z-space, the moments can be obtained as a function of time.

B

Biofilm Growth

The minimal biofilm inducing medium is known as MSgg[1] and can be prepared in the liquid or solid form following the protocol of table B.1. To make the solid plates, 2x MSgg has to be mixed with the equal volume of 3% autoclaved agar solution (the final plates will contain 1.5% agar). The MSgg can be stored in the fridge and mixed with the melted agar solution one day before the experiment. Around 30 ml of the medium should be conveyed to the standard petri dish plate and cooled down with the closed cap. The plates should be dried around 30 minutes before the inoculation under the hood. The biofilms in Fig. 6.1 were grown by spotting 2 μl of the wild type *B. subtilis* suspension with the optical density of ~1 in the center of the agar plate. After drying the droplet in around 20 minutes under the hood, the plate should be incubated at 30 °C for three days in a humidity chamber. Saturated sodium chloride salt solution was used to keep the humidity in the high level inside the chamber. A ring LED lamp was used to illuminate the plates from the top and time lapse imaging was performed by an USB camera with the pixel resolution 2048×1536 connected to a PC. Images were recorded using a custom written Matlab script at desired time intervals.

[1] Minimal salts glutamate glycerol

Table B.1: The composition and ratio of the chemicals to prepare the liquid and solid MSgg for the biofilm growth.

	Liquid				Plates-2x MSgg		
	250 mL	100 mL	500 mL		400 mL	1 L	2 L
0.1 M phosphate buffer	12.5	5	25		20	50	100
0.5 M MOPS pH 7	50	20	100	Filter sterile-wrapped in foil	80	200	400
5 mM $FeCl_3$***	2.5	1	5	Wrapped in foil	80	200	400
0.1 M $MgCl_2$	5	2	10		8	20	40
0.1 M $CaCl_2$***	1.75	0.7	3.5		2.8	7	14
0.01 M $MnCl_2$	1.25	0.5	2.5		2	5	10
1 mM $ZnCl_2$	0.25	0.1	0.5		0.4	1	2
10 mM Thiamine hydrochloride	0.05	0.02	0.1	Filter sterilized-4 degrees	0.08	0.2	0.4
10 mg/mL L-Phenylalanine	1.25	0.5	2.5	Filter sterilized-4 degrees	2	5	10
10 mg/mL L-Trytophan	1.25	0.5	2.5	Filter sterilized-4 degrees	2	5	10
10 mg/mL L-Threonine	1.25	0.5	2.5	Filter sterilized-4 degrees	2	5	10
50% glycerol	2.5	1	5		4	10	20
10% glutamate	12.5	5	25		20	50	100
H_2O	158	63.2	316		52.72	131.8	263.6
***add after filter sterilization							
solid media	3% agar						
	1 L agar	30 gr agar					
	500 mL agar	15 gr agar					
	100 mL agar	3 gr agar					
phosphate buffer		2					
1 M K_2HPO_4	3.075	6.15	autoclaved				
1 M KH_2HPO_4	1.925	3.85					
H_2o	45	90	autoclaved				

Bibliography

[1] J. Postgate. *Microbes and man*. Cambridge University Press, 2000.

[2] F. Garcia-Pichel, J. Belnap, S. Neuer, and F. Schanz. "Estimates of global cyanobacterial biomass and its distribution". *Algological Studies* 109.1 (2003), pp. 213–227.

[3] H. C. Berg. *E. coli in Motion*. Springer Science & Business Media, 2008.

[4] M. J. Waites, N. L. Morgan, J. S. Rockey, and G. Higton. *Industrial microbiology: an introduction*. John Wiley & Sons, 2009.

[5] A. E. Brown and A. E. Brown. *Microbiological applications: laboratory manual in general microbiology*. QR63 B76 2012. 2012.

[6] M. Theves. "Bacterial motility and growth in open and confined environments" (2013).

[7] S. Ramaswamy. "The mechanics and statistics of active matter" (2010).

[8] M. C. Marchetti, J.-F. Joanny, S. Ramaswamy, T. B. Liverpool, J. Prost, M. Rao, and R. A. Simha. "Hydrodynamics of soft active matter". *Reviews of Modern Physics* 85.3 (2013), p. 1143.

[9] H. C. Berg, D. A. Brown, et al. "Chemotaxis in Escherichia coli analysed by three-dimensional tracking". *Nature* 239.5374 (1972), pp. 500–504.

[10] G. M. Viswanathan, M. G. Da Luz, E. P. Raposo, and H. E. Stanley. *The physics of foraging: an introduction to random searches and biological encounters*. Cambridge University Press, 2011.

[11] M. Brambilla, E. Ferrante, M. Birattari, and M. Dorigo. "Swarm robotics: a review from the swarm engineering perspective". *Swarm Intelligence* 7.1 (2013), pp. 1–41.

[12] D. Helbing. "Traffic and related self-driven many-particle systems". *Reviews of modern physics* 73.4 (2001), p. 1067.

[13] J. Wang and W. Gao. "Nano/microscale motors: biomedical opportunities and challenges". *ACS nano* 6.7 (2012), pp. 5745–5751.

[14] W. F. Paxton, K. C. Kistler, C. C. Olmeda, A. Sen, S. K. St. Angelo, Y. Cao, T. E. Mallouk, P. E. Lammert, and V. H. Crespi. "Catalytic nanomotors: autonomous movement of striped nanorods". *Journal of the American Chemical Society* 126.41 (2004), pp. 13424–13431.

[15] R. F. Ismagilov, A. Schwartz, N. Bowden, and G. M. Whitesides. "Autonomous Movement and Self-Assembly". *Angewandte Chemie* 114.4 (2002), pp. 674–676.

[16] R. Dreyfus, J. Baudry, M. L. Roper, M. Fermigier, H. A. Stone, and J. Bibette. "Microscopic artificial swimmers". *Nature* 437.7060 (2005), pp. 862–865.

[17] H.-R. Jiang, N. Yoshinaga, and M. Sano. "Active motion of a Janus particle by self-thermophoresis in a defocused laser beam". *Physical review letters* 105.26 (2010), p. 268302.

[18] C. Bechinger, R. Di Leonardo, H. Löwen, C. Reichhardt, G. Volpe, and G. Volpe. "Active particles in complex and crowded environments". *Reviews of Modern Physics* 88.4 (2016), p. 045006.

[19] J. Elgeti, R. G. Winkler, and G. Gompper. "Physics of microswimmers—single particle motion and collective behavior: a review". *Reports on progress in physics* 78.5 (2015), p. 056601.

[20] D. L. Koch and G. Subramanian. "Collective hydrodynamics of swimming microorganisms: living fluids". *Annual Review of Fluid Mechanics* 43 (2011), pp. 637–659.

[21] H.-P. Zhang, A. Be'er, E.-L. Florin, and H. L. Swinney. "Collective motion and density fluctuations in bacterial colonies". *Proceedings of the National Academy of Sciences* 107.31 (2010), pp. 13626–13630.

[22] T. Pedley and J. Kessler. "Hydrodynamic phenomena in suspensions of swimming microorganisms". *Annual Review of Fluid Mechanics* 24.1 (1992), pp. 313–358.

[23] H.-C. Flemming and J. Wingender. "The biofilm matrix". *Nature Reviews Microbiology* 8.9 (2010), pp. 623–633.

[24] D. B. Kearns. "A field guide to bacterial swarming motility". *Nature Reviews Microbiology* 8.9 (2010), pp. 634–644.

[25] E. Lauga and T. R. Powers. "The hydrodynamics of swimming microorganisms". *Reports on Progress in Physics* 72.9 (2009), p. 096601.

[26] J. Henrichsen. "Bacterial surface translocation: a survey and a classification." *Bacteriological reviews* 36.4 (1972), p. 478.

[27] E. M. Purcell. "Life at low Reynolds number". *American journal of physics* 45.1 (1977), pp. 3–11.

[28] R. M. Harshey. "Bacterial motility on a surface: many ways to a common goal". *Annual Reviews in Microbiology* 57.1 (2003), pp. 249–273.

[29] D. B. Kearns and R. Losick. "Swarming motility in undomesticated Bacillus subtilis". *Molecular microbiology* 49.3 (2003), pp. 581–590.

[30] J. S. Mattick. "Type IV pili and twitching motility". *Annual Reviews in Microbiology* 56.1 (2002), pp. 289–314.

[31] A. J. Merz, M. So, and M. P. Sheetz. "Pilus retraction powers bacterial twitching motility". *Nature* 407.6800 (2000), pp. 98–102.

[32] G. A. O'toole and R. Kolter. "Flagellar and twitching motility are necessary for Pseudomonas aeruginosa biofilm development". *Molecular microbiology* 30.2 (1998), pp. 295–304.

[33] M. J. McBride. "Bacterial gliding motility: multiple mechanisms for cell movement over surfaces". *Annual Reviews in Microbiology* 55.1 (2001), pp. 49–75.

[34] S. L. Bardy, S. Y. Ng, and K. F. Jarrell. "Prokaryotic motility structures". *Microbiology* 149.2 (2003), pp. 295–304.

[35] H. C. Berg. "The rotary motor of bacterial flagella". *Annual review of biochemistry* 72 (2003).

[36] R. M. Macnab. “How bacteria assemble flagella”. *Annual Reviews in Microbiology* 57.1 (2003), pp. 77–100.

[37] S. Mukherjee and D. B. Kearns. “The structure and regulation of flagella in Bacillus subtilis”. *Annual review of genetics* 48 (2014), pp. 319–340.

[38] C. Brennen and H. Winet. “Fluid mechanics of propulsion by cilia and flagella”. *Annual Review of Fluid Mechanics* 9.1 (1977), pp. 339–398.

[39] F. D. Warner and P. Satir. “The structural basis of ciliary bend formation”. *The Journal of cell biology* 63.1 (1974), pp. 35–63.

[40] C. Calladine. “Change of waveform in bacterial flagella: the role of mechanics at the molecular level”. *Journal of Molecular Biology* 118.4 (1978), pp. 457–479.

[41] C Speier, R Vogel, and H Stark. “Modeling the bacterial flagellum by an elastic network of rigid bodies”. *Physical biology* 8.4 (2011), p. 046009.

[42] E. Lauga. “Bacterial hydrodynamics”. *Annual Review of Fluid Mechanics* 48 (2016), pp. 105–130.

[43] N. C. Darnton, L. Turner, S. Rojevsky, and H. C. Berg. “On torque and tumbling in swimming Escherichia coli”. *Journal of bacteriology* 189.5 (2007), pp. 1756–1764.

[44] L. Turner, W. S. Ryu, and H. C. Berg. “Real-time imaging of fluorescent flagellar filaments”. *Journal of bacteriology* 182.10 (2000), pp. 2793–2801.

[45] R Kamiya, S Asakura, K Wakabayashi, and K Namba. “Transition of bacterial flagella from helical to straight forms with different subunit arrangements”. *Journal of molecular biology* 131.4 (1979), pp. 725–742.

[46] W. contributors. *Bacillus subtilis — Wikipedia, The Free Encyclopedia*. [Online; accessed 18-January-2018]. 2017. URL: \url{https://en.wikipedia.org/w/index.php?title=Bacillus_subtilis&oldid=817349849}.

[47] W. contributors. *Operon — Wikipedia, The Free Encyclopedia*. [Online; accessed 18-January-2018]. 2017. URL: \url{https://en.wikipedia.org/w/index.php?title=Operon&oldid=810545681}.

[48] S. B. Guttenplan, S. Shaw, and D. B. Kearns. “The cell biology of peritrichous flagella in Bacillus subtilis”. *Molecular microbiology* 87.1 (2013), pp. 211–229.

[49] F. Morrison. *An Introduction to Fluid Mechanics*. Cambridge University Press, 2013. ISBN: 9781107003538. URL: https://books.google.de/books?id=TTh8crFP8CUC.

[50] M. Li. “Experimental study of swimming flagellated bacteria and their collective behaviour in concentrated suspensions” (2010).

[51] S. Chattopadhyay, R. Moldovan, C. Yeung, and X. Wu. “Swimming efficiency of bacterium Escherichiacoli”. *Proceedings of the National Academy of Sciences* 103.37 (2006), pp. 13712–13717.

[52] H. C. Berg. *Random walks in biology*. Princeton University Press, 1993.

[53] S. Chattopadhyay and X.-L. Wu. “The effect of long-range hydrodynamic interaction on the swimming of a single bacterium”. *Biophysical journal* 96.5 (2009), pp. 2023–2028.

[54] J Gray. “The movement of sea-urchin spermatozoa”. *Journal of Experimental Biology* 32.4 (1955), pp. 775–801.

[55] J. Gray and G. Hancock. "The propulsion of sea-urchin spermatozoa". *Journal of Experimental Biology* 32.4 (1955), pp. 802–814.

[56] S. Chattopadhyay. "Study of bacterial motility using optical tweezers". PhD thesis. University of Pittsburgh, 2008.

[57] B. Rodenborn, C.-H. Chen, H. L. Swinney, B. Liu, and H. Zhang. "Propulsion of microorganisms by a helical flagellum". *Proceedings of the National Academy of Sciences* 110.5 (2013), E338–E347.

[58] S. J. Lighthill. *Mathematical biofluiddynamics*. SIAM, 1975.

[59] G. Hancock. "The self-propulsion of microscopic organisms through liquids". In: *Proceedings of the Royal Society of London A: Mathematical, Physical and Engineering Sciences*. Vol. 217. 1128. The Royal Society. 1953, pp. 96–121.

[60] J. Lighthill. "Flagellar hydrodynamics". *SIAM review* 18.2 (1976), pp. 161–230.

[61] R. Brown. "On the particles contained in the pollen of plants; and on the general existence of active molecules in organic and inorganic bodies". *Edinburgh New Philosophical Journal* 5 (1828), pp. 358–371.

[62] A. Einstein. "On the motion of small particles suspended in liquids at rest required by the molecular-kinetic theory of heat". *Annalen der physik* 17 (1905), pp. 549–560.

[63] M. By Smoluchowski. "On the Kinetic Theory of Brownian Molecular Motion and Suspensions". *annals of physics* 326.14 (1906), pp. 756–780.

[64] P. Langevin. "Sur la théorie du mouvement brownien". *CR Acad. Sci. Paris* 146.530-533 (1908), p. 530.

[65] F. Höfling and T. Franosch. "Anomalous transport in the crowded world of biological cells". *Reports on Progress in Physics* 76.4 (2013), p. 046602.

[66] W. T. Coffey and Y. P. Kalmykov. *The Langevin equation: with applications to stochastic problems in physics, chemistry and electrical engineering*. World Scientific, 2004.

[67] R. Metzler and J. Klafter. "The random walk's guide to anomalous diffusion: a fractional dynamics approach". *Physics reports* 339.1 (2000), pp. 1–77.

[68] Wikipedia contributors. *Rotational diffusion — Wikipedia, The Free Encyclopedia*. https://en.wikipedia.org/w/index.php?title=Rotational_diffusion&oldid=700589084. [Online; accessed 27-May-2018]. 2016.

[69] P. S. Lovely and F. Dahlquist. "Statistical measures of bacterial motility and chemotaxis". *Journal of theoretical biology* 50.2 (1975), pp. 477–496.

[70] J. Taktikos. "Modeling the random walk and chemotaxis of bacteria: Aspects of biofilm formation" (2012).

[71] K Martens, L Angelani, R Di Leonardo, and L Bocquet. "Probability distributions for the run-and-tumble bacterial dynamics: An analogy to the Lorentz model". *The European Physical Journal E* 35.9 (2012), p. 84.

[72] Ò. Guadayol, K. L. Thornton, and S. Humphries. "Cell morphology governs directional control in swimming bacteria". *Scientific reports* 7.1 (2017), p. 2061.

[73] F. Schweitzer. *Brownian agents and active particles: collective dynamics in the natural and social sciences*. Springer Science & Business Media, 2007.

[74] G. E. Uhlenbeck and L. S. Ornstein. "On the theory of the Brownian motion". *Physical review* 36.5 (1930), p. 823.

[75] G. Volpe, S. Gigan, and G. Volpe. "Simulation of the active Brownian motion of a microswimmer". *American Journal of Physics* 82.7 (2014), pp. 659–664.

[76] M. Raffel, C. E. Willert, S. T. Wereley, and J. Kompenhans. *Particle image velocimetry: a practical guide*. Springer, 2013.

[77] E. G. Drucker and G. V. Lauder. "Locomotor forces on a swimming fish: three-dimensional vortex wake dynamics quantified using digital particle image velocimetry". *Journal of Experimental Biology* 202.18 (1999), pp. 2393–2412.

[78] E. J. Stamhuis. "Basics and principles of particle image velocimetry (PIV) for mapping biogenic and biologically relevant flows". *Aquatic Ecology* 40.4 (2006), pp. 463–479.

[79] J. Westerweel, D Dabiri, and M. Gharib. "The effect of a discrete window offset on the accuracy of cross-correlation analysis of digital PIV recordings". *Experiments in fluids* 23.1 (1997), pp. 20–28.

[80] D. P. Hart. "Super-resolution PIV by recursive local-correlation". *Journal of Visualization* 10 (1999), pp. 1–10.

[81] H Huang, D Dabiri, and M. Gharib. "On errors of digital particle image velocimetry". *Measurement Science and Technology* 8.12 (1997), p. 1427.

[82] W. Thielicke and E. Stamhuis. "PIVlab–towards user-friendly, affordable and accurate digital particle image velocimetry in MATLAB". *Journal of Open Research Software* 2.1 (2014).

[83] H. C. Berg and R. A. Anderson. "Bacteria swim by rotating their flagellar filaments". *Nature* 245.5425 (1973), p. 380.

[84] L. Turner, L. Ping, M. Neubauer, and H. C. Berg. "Visualizing flagella while tracking bacteria". *Biophysical journal* 111.3 (2016), pp. 630–639.

[85] G. H. Wadhams and J. P. Armitage. "Making sense of it all: bacterial chemotaxis". *Nature Reviews Molecular Cell Biology* 5.12 (2004), p. 1024.

[86] P. Kanehl and T. Ishikawa. "Fluid mechanics of swimming bacteria with multiple flagella". *Physical Review E* 89.4 (2014), p. 042704.

[87] S. Y. Reigh, R. G. Winkler, and G. Gompper. "Synchronization and bundling of anchored bacterial flagella". *Soft Matter* 8.16 (2012), pp. 4363–4372.

[88] T. R. Powers. "Role of body rotation in bacterial flagellar bundling". *Physical Review E* 65.4 (2002), p. 040903.

[89] P. J. Mears, S. Koirala, C. V. Rao, I. Golding, and Y. R. Chemla. "Escherichia coli swimming is robust against variations in flagellar number". *Elife* 3 (2014).

[90] A. Ishihara, J. E. Segall, S. M. Block, and H. C. Berg. "Coordination of flagella on filamentous cells of Escherichia coli." *Journal of Bacteriology* 155.1 (1983), pp. 228–237.

[91] P. A. Spiro, J. S. Parkinson, and H. G. Othmer. "A model of excitation and adaptation in bacterial chemotaxis". *Proceedings of the National Academy of Sciences* 94.14 (1997), pp. 7263–7268.

[92] B. W. Andrews, T.-M. Yi, and P. A. Iglesias. "Optimal noise filtering in the chemotactic response of Escherichia coli". *PLoS computational biology* 2.11 (2006), e154.

[93] N. Vladimirov, L. Løvdok, D. Lebiedz, and V. Sourjik. "Dependence of bacterial chemotaxis on gradient shape and adaptation rate". *PLoS computational biology* 4.12 (2008), e1000242.

[94] N. Vladimirov, D. Lebiedz, and V. Sourjik. "Predicted auxiliary navigation mechanism of peritrichously flagellated chemotactic bacteria". *PLoS computational biology* 6.3 (2010), e1000717.

[95] M. W. Sneddon, W. Pontius, and T. Emonet. "Stochastic coordination of multiple actuators reduces latency and improves chemotactic response in bacteria". *Proceedings of the National Academy of Sciences* 109.3 (2012), pp. 805–810.

[96] S. Terasawa, H. Fukuoka, Y. Inoue, T. Sagawa, H. Takahashi, and A. Ishijima. "Coordinated reversal of flagellar motors on a single Escherichia coli cell". *Biophysical journal* 100.9 (2011), pp. 2193–2200.

[97] B. Hu and Y. Tu. "Coordinated switching of bacterial flagellar motors: Evidence for direct motor-motor coupling?" *Physical review letters* 110.15 (2013), p. 158703.

[98] P. J. Mears. *Illuminating the relationship between flagellar activity and bacterial swimming*. University of Illinois at Urbana-Champaign, 2014.

[99] E. A. Korobkova, T. Emonet, H. Park, and P. Cluzel. "Hidden stochastic nature of a single bacterial motor". *Physical review letters* 96.5 (2006), p. 058105.

[100] J. Hu, M. Yang, G. Gompper, and R. G. Winkler. "Modelling the mechanics and hydrodynamics of swimming E. coli". *Soft matter* 11.40 (2015), pp. 7867–7876.

[101] A. P. Berke, L. Turner, H. C. Berg, and E. Lauga. "Hydrodynamic attraction of swimming microorganisms by surfaces". *Physical Review Letters* 101.3 (2008), p. 038102.

[102] A. Sokolov and I. S. Aranson. "Physical properties of collective motion in suspensions of bacteria". *Physical review letters* 109.24 (2012), p. 248109.

[103] J. Dunkel, S. Heidenreich, K. Drescher, H. H. Wensink, M. Bär, and R. E. Goldstein. "Fluid dynamics of bacterial turbulence". *Physical review letters* 110.22 (2013), p. 228102.

[104] I. Tuval, L. Cisneros, C. Dombrowski, C. W. Wolgemuth, J. O. Kessler, and R. E. Goldstein. "Bacterial swimming and oxygen transport near contact lines". *Proceedings of the National Academy of Sciences of the United States of America* 102.7 (2005), pp. 2277–2282.

[105] C. Douarche, A. Buguin, H. Salman, and A. Libchaber. "E. Coli and oxygen: a motility transition". *Physical review letters* 102.19 (2009), p. 198101.

[106] E. E. W. Rudi Rottenfusser and M. W. Davidson. *Enhancing Contrast in Transmitted Light*. n.d. URL: \url{http://zeiss-campus.magnet.fsu.edu/articles/basics/contrast.html}.

[107] A. C. Bovik. *The essential guide to image processing*. Academic Press, 2009.

[108] P. D. Frymier, R. M. Ford, H. C. Berg, and P. T. Cummings. "Three-dimensional tracking of motile bacteria near a solid planar surface". *Proceedings of the National Academy of Sciences* 92.13 (1995), pp. 6195–6199.

[109] P. D. Frymier and R. M. Ford. "Analysis of bacterial swimming speed approaching a solid–liquid interface". *AIChE journal* 43.5 (1997), pp. 1341–1347.

[110] M. Molaei, M. Barry, R. Stocker, and J. Sheng. "Failed escape: solid surfaces prevent tumbling of Escherichia coli". *Physical review letters* 113.6 (2014), p. 068103.

[111] J.-B. Masson, G. Voisinne, J. Wong-Ng, A. Celani, and M. Vergassola. "Noninvasive inference of the molecular chemotactic response using bacterial trajectories". *Proceedings of the National Academy of Sciences* 109.5 (2012), pp. 1802–1807.

[112] Y. Hyon, T. R. Powers, R. Stocker, H. C. Fu, et al. "The wiggling trajectories of bacteria". *Journal of Fluid Mechanics* 705 (2012), pp. 58–76.

[113] C. Valeriani, M. Li, J. Novosel, J. Arlt, and D. Marenduzzo. "Colloids in a bacterial bath: simulations and experiments". *Soft Matter* 7.11 (2011), pp. 5228–5238.

[114] E. Meijering, O. Dzyubachyk, and I. Smal. "Methods for cell and particle tracking". In: *Methods in enzymology*. Vol. 504. Elsevier, 2012, pp. 183–200.

[115] M. R. Shaebani, Z. Sadjadi, I. M. Sokolov, H. Rieger, and L. Santen. "Anomalous diffusion of self-propelled particles in directed random environments". *Physical Review E* 90.3 (2014), p. 030701.

[116] Z. Sadjadi, M. R. Shaebani, H. Rieger, and L. Santen. "Persistent-random-walk approach to anomalous transport of self-propelled particles". *Physical Review E* 91.6 (2015), p. 062715.

[117] J. Saragosti, P. Silberzan, and A. Buguin. "Modeling E. coli tumbles by rotational diffusion. Implications for chemotaxis". *PloS one* 7.4 (2012), e35412.

[118] P. Tierno and M. R. Shaebani. "Enhanced diffusion and anomalous transport of magnetic colloids driven above a two-state flashing potential". *Soft matter* 12.14 (2016), pp. 3398–3405.

[119] O Bénichou, C Loverdo, M Moreau, and R Voituriez. "Two-dimensional intermittent search processes: An alternative to Lévy flight strategies". *Physical Review E* 74.2 (2006), p. 020102.

[120] M. Chabaud, M. L. Heuzé, M. Bretou, P. Vargas, P. Maiuri, P. Solanes, M. Maurin, E. Terriac, M. Le Berre, D. Lankar, et al. "Cell migration and antigen capture are antagonistic processes coupled by myosin II in dendritic cells". *Nature communications* 6 (2015), p. 7526.

[121] J.-F. Rupprecht, O. Bénichou, and R. Voituriez. "Optimal search strategies of run-and-tumble walks". *Physical Review E* 94.1 (2016), p. 012117.

[122] V. Tejedor, R. Voituriez, and O. Bénichou. "Optimizing persistent random searches". *Physical review letters* 108.8 (2012), p. 088103.

[123] J. Saragosti, V. Calvez, N. Bournaveas, B. Perthame, A. Buguin, and P. Silberzan. "Directional persistence of chemotactic bacteria in a traveling concentration wave". *Proceedings of the National Academy of Sciences* 108.39 (2011), pp. 16235–16240.

[124] J. E. Segall, S. M. Block, and H. C. Berg. "Temporal comparisons in bacterial chemotaxis". *Proceedings of the National Academy of Sciences* 83.23 (1986), pp. 8987–8991.

[125] A. Celani and M. Vergassola. "Bacterial strategies for chemotaxis response". *Proceedings of the National Academy of Sciences* 107.4 (2010), pp. 1391–1396.

[126] D. A. Clark and L. C. Grant. "The bacterial chemotactic response reflects a compromise between transient and steady-state behavior". *Proceedings of the National Academy of Sciences of the United States of America* 102.26 (2005), pp. 9150–9155.

[127] J. T. Locsei. "Persistence of direction increases the drift velocity of run and tumble chemotaxis". *Journal of mathematical biology* 55.1 (2007), pp. 41–60.

[128] L. Dewenter, C. Alpmann, M. Woerdemann, and C. Denz. "Video-based analysis of the rotational behaviour of rod-shaped, self-propelled bacteria in holographic optical tweezers". In: *Biophotonics: Photonic Solutions for Better Health Care III*. Vol. 8427. International Society for Optics and Photonics. 2012, 84270N.

[129] A. Patteson, A. Gopinath, M Goulian, and P. Arratia. "Running and tumbling with E. coli in polymeric solutions". *Scientific reports* 5 (2015), p. 15761.

[130] F. Perrin. "Mouvement brownien d'un ellipsoide-I. Dispersion diélectrique pour des molécules ellipsoidales". *Journal de Physique et le Radium* 5.10 (1934), pp. 497–511.

[131] F. Perrin. "Mouvement Brownien d'un ellipsoide (II). Rotation libre et dépolarisation des fluorescences. Translation et diffusion de molécules ellipsoidales". *Journal de Physique et le Radium* 7.1 (1936), pp. 1–11.

[132] E. Lauga, W. R. DiLuzio, G. M. Whitesides, and H. A. Stone. "Swimming in circles: motion of bacteria near solid boundaries". *Biophysical journal* 90.2 (2006), pp. 400–412.

[133] ROTHSCHILD. "Non-random distribution of bull spermatozoa in a drop of sperm suspension". *Nature* 198.488 (1963), p. 1221.

[134] Y. Han, A. M. Alsayed, M. Nobili, J. Zhang, T. C. Lubensky, and A. G. Yodh. "Brownian motion of an ellipsoid". *Science* 314.5799 (2006), pp. 626–630.

[135] L. Lemelle, J.-F. Palierne, E. Chatre, C. Vaillant, and C. Place. "Curvature reversal of the circular motion of swimming bacteria probes for slip at solid/liquid interfaces". *Soft Matter* 9.41 (2013), pp. 9759–9762.

[136] L. Lemelle, J.-F. Palierne, E. Chatre, and C. Place. "Counterclockwise circular motion of bacteria swimming at the air-liquid interface". *Journal of bacteriology* 192.23 (2010), pp. 6307–6308.

[137] H. C. Berg and L. Turner. "Chemotaxis of bacteria in glass capillary arrays. Escherichia coli, motility, microchannel plate, and light scattering". *Biophysical Journal* 58.4 (1990), pp. 919–930.

[138] R Di Leonardo, D Dell'Arciprete, L Angelani, and V Iebba. "Swimming with an image". *Physical review letters* 106.3 (2011), p. 038101.

[139] H. Löwen. "Chirality in microswimmer motion: From circle swimmers to active turbulence". *The European Physical Journal Special Topics* 225.11-12 (2016), pp. 2319–2331.

[140] C. G. Ehrenberg. *Die Infusionsthierchen als vollkommene Organismen*. Leopold Voss, Leipzig, Germany, 1838.

[141] K. Reichert. "Uber die Sichtbarmachung der Geisseln und die Geisselbewegung der Bakterien". *Zentbl. Bakteriol. Parasitenk. Infektionskr. Abt. 1Orig.* 51 (1909), pp. 274–305.

[142] E. Leifson. "Staining, shape, and arrangement of bacterial flagella". *Journal of bacteriology* 62.4 (1951), p. 377.

[143] A. Houwink and W. Van Iterson. "Electron microscopical observations on bacterial cytology II. A study of flagellation". *Biochimica et biophysica acta* 5 (1950), pp. 10–44.

[144] A Pijper, M. L. Neser, and G Abraham. “The wavelengths of helical bacterial flagella”. *Microbiology* 14.2 (1956), pp. 371–380.

[145] R. Macnab and D. Koshland Jr. “Bacterial motility and chemotaxis: light-induced tumbling response and visualization of individual flagella”. *Journal of molecular biology* 84.3 (1974), pp. 399–406.

[146] R. M. Macnab. “Examination of bacterial flagellation by dark-field microscopy.” *Journal of clinical microbiology* 4.3 (1976), pp. 258–265.

[147] R. M. Macnab and M. K. Ornston. “Normal-to-curly flagellar transitions and their role in bacterial tumbling. Stabilization of an alternative quaternary structure by mechanical force”. *Journal of molecular biology* 112.1 (1977), pp. 1–30.

[148] H. Hotani. “Micro-video study of moving bacterial flagellar filaments: III. Cyclic transformation induced by mechanical force”. *Journal of molecular biology* 156.4 (1982), pp. 791–806.

[149] S. Kudo, Y. Magariyama, and S.-I. Aizawa. “Abrupt changes in flagellar rotation observed by laser dark-field microscopy”. *Nature* 346.6285 (1990), p. 677.

[150] Y. Magariyama, S. Sugiyama, and S. Kudo. “Bacterial swimming speed and rotation rate of bundled flagella”. *FEMS microbiology letters* 199.1 (2001), pp. 125–129.

[151] H.-P. Grossart, G. F. Steward, J. Martinez, and F. Azam. “A simple, rapid method for demonstrating bacterial flagella”. *Applied and environmental microbiology* 66.8 (2000), pp. 3632–3636.

[152] C. Weibull. “Some chemical and physico-chemical properties of the flagella of Proteus vulgaris”. *Biochim. et Biophys. Acta* 2 (1948), pp. 351–361.

[153] R. Kamiya and S. Asakura. “Helical transformations of Salmonella flagella in vitro”. *Journal of molecular biology* 106.1 (1976), pp. 167–186.

[154] K. M. Blair, L. Turner, J. T. Winkelman, H. C. Berg, and D. B. Kearns. “A molecular clutch disables flagella in the Bacillus subtilis biofilm”. *science* 320.5883 (2008), pp. 1636–1638.

[155] M. Arnaud, A. Chastanet, and M. Débarbouillé. “New vector for efficient allelic replacement in naturally nontransformable, low-GC-content, gram-positive bacteria”. *Applied and environmental microbiology* 70.11 (2004), pp. 6887–6891.

[156] K. R. Spring and M. W. Davidson. *Introduction to Fluorescence Microscopy*. n.d. URL: \url{https://www.microscopyu.com/techniques/fluorescence/introduction-to-fluorescence-microscopy}.

[157] M. F. L. Derek K. Toomre and M. W. Davidson. *Introduction to Spinning Disk Confocal Microscopy*. n.d. URL: \url{http://zeiss-campus.magnet.fsu.edu/articles/spinningdisk/introduction.html}.

[158] M. Ito, N. Terahara, S. Fujinami, and T. A. Krulwich. “Properties of motility in Bacillus subtilis powered by the H+-coupled MotAB flagellar stator, Na+-coupled MotPS or hybrid stators MotAS or MotPB”. *Journal of molecular biology* 352.2 (2005), pp. 396–408.

[159] P. Lewus and R. M. Ford. “Quantification of random motility and chemotaxis bacterial transport coefficients using individual-cell and population-scale assays”. *Biotechnology and bioengineering* 75.3 (2001), pp. 292–304.

[160] R. R. Vuppula, M. S. Tirumkudulu, and K. Venkatesh. "Chemotaxis of Escherichia coli to L-serine". *Physical biology* 7.2 (2010), p. 026007.

[161] T. Vicsek and A. Zafeiris. "Collective motion". *Physics Reports* 517.3-4 (2012), pp. 71–140.

[162] D. J. Sumpter. "The principles of collective animal behaviour". *Philosophical Transactions of the Royal Society B: Biological Sciences* 361.1465 (2006), pp. 5–22.

[163] W. Commons. *File:Fugle, ørnsø 073.jpg — Wikimedia Commons, the free media repository*. [Online; accessed 23-May-2018]. 2016. URL: \url{https://commons.wikimedia.org/w/index.php?title=File:Fugle,_%C3%B8rns%C3%B8_073.jpg&oldid=224526699}.

[164] W. Commons. *File:Moofushi Kandu fish.jpg — Wikimedia Commons, the free media repository*. [Online; accessed 23-May-2018]. 2016. URL: \url{https://commons.wikimedia.org/w/index.php?title=File:Moofushi_Kandu_fish.jpg&oldid=188092446}.

[165] W. Commons. *File:Cologne Germany Flock-of-sheep-01.jpg — Wikimedia Commons, the free media repository*. [Online; accessed 23-May-2018]. 2017. URL: \url{https://commons.wikimedia.org/w/index.php?title=File:Cologne_Germany_Flock-of-sheep-01.jpg&oldid=268111374}.

[166] X. Trepat, M. R. Wasserman, T. E. Angelini, E. Millet, D. A. Weitz, J. P. Butler, and J. J. Fredberg. "Physical forces during collective cell migration". *Nature physics* 5.6 (2009), p. 426.

[167] D. L. Blair, T Neicu, and A. Kudrolli. "Vortices in vibrated granular rods". *Physical Review E* 67.3 (2003), p. 031303.

[168] T. Vicsek, A. Czirók, E. Ben-Jacob, I. Cohen, and O. Shochet. "Novel type of phase transition in a system of self-driven particles". *Physical review letters* 75.6 (1995), p. 1226.

[169] C. W. Reynolds. "Flocks, herds and schools: A distributed behavioral model". In: *ACM SIGGRAPH computer graphics*. Vol. 21. 4. ACM. 1987, pp. 25–34.

[170] G. Baglietto and E. V. Albano. "Nature of the order-disorder transition in the Vicsek model for the collective motion of self-propelled particles". *Physical Review E* 80.5 (2009), p. 050103.

[171] M. R. D'Orsogna, Y.-L. Chuang, A. L. Bertozzi, and L. S. Chayes. "Self-propelled particles with soft-core interactions: patterns, stability, and collapse". *Physical review letters* 96.10 (2006), p. 104302.

[172] A. Kudrolli, G. Lumay, D. Volfson, and L. S. Tsimring. "Swarming and swirling in self-propelled polar granular rods". *Physical review letters* 100.5 (2008), p. 058001.

[173] V. Narayan, S. Ramaswamy, and N. Menon. "Long-lived giant number fluctuations in a swarming granular nematic". *Science* 317.5834 (2007), pp. 105–108.

[174] J. Deseigne, O. Dauchot, and H. Chaté. "Collective motion of vibrated polar disks". *Physical review letters* 105.9 (2010), p. 098001.

[175] A. Bricard, J.-B. Caussin, N. Desreumaux, O. Dauchot, and D. Bartolo. "Emergence of macroscopic directed motion in populations of motile colloids". *Nature* 503.7474 (2013), p. 95.

[176] E. Méhes and T. Vicsek. "Collective motion of cells: from experiments to models". *Integrative biology* 6.9 (2014), pp. 831–854.

[177] X. Chen, X. Dong, A. Be'er, H. L. Swinney, and H. Zhang. "Scale-invariant correlations in dynamic bacterial clusters". *Physical review letters* 108.14 (2012), p. 148101.

[178] C. Dombrowski, L. Cisneros, S. Chatkaew, R. E. Goldstein, and J. O. Kessler. "Self-concentration and large-scale coherence in bacterial dynamics". *Physical review letters* 93.9 (2004), p. 098103.

[179] A. Sokolov, I. S. Aranson, J. O. Kessler, and R. E. Goldstein. "Concentration dependence of the collective dynamics of swimming bacteria". *Physical review letters* 98.15 (2007), p. 158102.

[180] A. Sokolov, R. E. Goldstein, F. I. Feldchtein, and I. S. Aranson. "Enhanced mixing and spatial instability in concentrated bacterial suspensions". *Physical Review E* 80.3 (2009), p. 031903.

[181] S. Vedel, S. Tay, D. M. Johnston, H. Bruus, and S. R. Quake. "Migration of cells in a social context". *Proceedings of the National Academy of Sciences* 110.1 (2013), pp. 129–134.

[182] F. G. Woodhouse and R. E. Goldstein. "Spontaneous circulation of confined active suspensions". *Physical review letters* 109.16 (2012), p. 168105.

[183] H. H. Wensink, J. Dunkel, S. Heidenreich, K. Drescher, R. E. Goldstein, H. Löwen, and J. M. Yeomans. "Meso-scale turbulence in living fluids". *Proceedings of the National Academy of Sciences* 109.36 (2012), pp. 14308–14313.

[184] N. H. Mendelson, A. Bourque, K. Wilkening, K. R. Anderson, and J. C. Watkins. "Organized cell swimming motions in Bacillus subtilis colonies: patterns of short-lived whirls and jets". *Journal of bacteriology* 181.2 (1999), pp. 600–609.

[185] N. C. Darnton, L. Turner, S. Rojevsky, and H. C. Berg. "Dynamics of bacterial swarming". *Biophysical journal* 98.10 (2010), pp. 2082–2090.

[186] H. Zhang, A. Be'Er, R. S. Smith, E.-L. Florin, and H. L. Swinney. "Swarming dynamics in bacterial colonies". *EPL (Europhysics Letters)* 87.4 (2009), p. 48011.

[187] A. Baskaran and M. C. Marchetti. "Hydrodynamics of self-propelled hard rods". *Physical Review E* 77.1 (2008), p. 011920.

[188] F. Ginelli, F. Peruani, M. Bär, and H. Chaté. "Large-scale collective properties of self-propelled rods". *Physical review letters* 104.18 (2010), p. 184502.

[189] F. Peruani, A. Deutsch, and M. Bär. "Nonequilibrium clustering of self-propelled rods". *Physical Review E* 74.3 (2006), p. 030904.

[190] A. Baskaran and M. C. Marchetti. "Statistical mechanics and hydrodynamics of bacterial suspensions". *Proceedings of the National Academy of Sciences* 106.37 (2009), pp. 15567–15572.

[191] D. Saintillan and M. J. Shelley. "Emergence of coherent structures and large-scale flows in motile suspensions". *Journal of the Royal Society Interface* (2011), rsif20110355.

[192] J Gachelin, A Rousselet, A Lindner, and E Clement. "Collective motion in an active suspension of Escherichia coli bacteria". *New Journal of Physics* 16.2 (2014), p. 025003.

[193] T. Ishikawa, N. Yoshida, H. Ueno, M. Wiedeman, Y. Imai, and T. Yamaguchi. "Energy transport in a concentrated suspension of bacteria". *Physical review letters* 107.2 (2011), p. 028102.

[194] A. Rabani, G. Ariel, and A. Be'er. "Collective motion of spherical bacteria". *PloS one* 8.12 (2013), e83760.

[195] B. Ilkanaiv, D. B. Kearns, G. Ariel, and A. Be'er. "Effect of Cell Aspect Ratio on Swarming Bacteria". *Physical review letters* 118.15 (2017), p. 158002.

[196] S. Benisty, E. Ben-Jacob, G. Ariel, and A. Be'er. "Antibiotic-induced anomalous statistics of collective bacterial swarming". *Physical review letters* 114.1 (2015), p. 018105.

[197] P. Romanczuk, M. Bär, W. Ebeling, B. Lindner, and L. Schimansky-Geier. "Active brownian particles". *The European Physical Journal Special Topics* 202.1 (2012), pp. 1–162.

[198] M. B. Miller and B. L. Bassler. "Quorum sensing in bacteria". *Annual Reviews in Microbiology* 55.1 (2001), pp. 165–199.

[199] B.-q. Ai, Z.-G. Shao, and W. Zhong. "Mixing and demixing of binary mixtures of polar chiral active particles". *Soft Matter* (2018).

[200] B. Liebchen and D. Levis. "Collective behavior of chiral active matter: pattern formation and enhanced flocking". *Physical review letters* 119.5 (2017), p. 058002.

[201] L. H. Cisneros, R. Cortez, C. Dombrowski, R. E. Goldstein, and J. O. Kessler. "Fluid dynamics of self-propelled microorganisms, from individuals to concentrated populations". *Experiments in Fluids* 43.5 (2007), pp. 737–753.

[202] L. H. Cisneros, J. O. Kessler, S. Ganguly, and R. E. Goldstein. "Dynamics of swimming bacteria: Transition to directional order at high concentration". *Physical Review E* 83.6 (2011), p. 061907.

[203] T. Eisenstecken, J. Hu, and R. G. Winkler. "Bacterial swarmer cells in confinement: a mesoscale hydrodynamic simulation study". *Soft Matter* 12.40 (2016), pp. 8316–8326.

[204] E. Ben-Naim and P. L. Krapivsky. "The inelastic Maxwell model". In: *Granular Gas Dynamics*. Springer, 2003, pp. 65–94.

[205] F. Kümmel, B. ten Hagen, R. Wittkowski, I. Buttinoni, R. Eichhorn, G. Volpe, H. Löwen, and C. Bechinger. "Circular motion of asymmetric self-propelling particles". *Physical review letters* 110.19 (2013), p. 198302.

[206] A. Kaiser, K. Popowa, and H. Löwen. "Active dipole clusters: from helical motion to fission". *Physical Review E* 92.1 (2015), p. 012301.

[207] C. Chen, S. Liu, X.-q. Shi, H. Chaté, and Y. Wu. "Weak synchronization and large-scale collective oscillation in dense bacterial suspensions". *Nature* 542.7640 (2017), p. 210.

[208] G. Ariel, A. Rabani, S. Benisty, J. D. Partridge, R. M. Harshey, and A. Be'Er. "Swarming bacteria migrate by Lévy Walk". *Nature communications* 6 (2015), p. 8396.

[209] G. Ariel, A. Be'er, and A. Reynolds. "Chaotic model for Lévy walks in swarming bacteria". *Physical review letters* 118.22 (2017), p. 228102.

[210] X.-L. Wu and A. Libchaber. "Particle diffusion in a quasi-two-dimensional bacterial bath". *Physical review letters* 84.13 (2000), p. 3017.

[211] K. C. Leptos, J. S. Guasto, J. P. Gollub, A. I. Pesci, and R. E. Goldstein. "Dynamics of enhanced tracer diffusion in suspensions of swimming eukaryotic microorganisms". *Physical Review Letters* 103.19 (2009), p. 198103.

[212] W. H. Press, S. A. Teukolsky, W. T. Vetterling, and B. P. Flannery. *Numerical recipes in C*. Vol. 2. Cambridge university press Cambridge, 1996.

[213] Wikipedia contributors. *Bilinear interpolation — Wikipedia, The Free Encyclopedia*. [Online; accessed 13-May-2018]. 2017. URL: https://en.wikipedia.org/w/index.php?title=Bilinear_interpolation&oldid=809623103.

[214] V. A. Martinez, J. Schwarz-Linek, M. Reufer, L. G. Wilson, A. N. Morozov, and W. C. Poon. "Flagellated bacterial motility in polymer solutions". *Proceedings of the National Academy of Sciences* 111.50 (2014), pp. 17771–17776.

[215] R. G. Endres and N. S. Wingreen. "Accuracy of direct gradient sensing by single cells". *Proceedings of the National Academy of Sciences* 105.41 (2008), pp. 15749–15754.

[216] M. Kollmann, L. Løvdok, K. Bartholomé, J. Timmer, and V. Sourjik. "Design principles of a bacterial signalling network". *Nature* 438.7067 (2005), p. 504.

[217] L. Turner, R. Zhang, N. C. Darnton, and H. C. Berg. "Visualization of flagella during bacterial swarming". *Journal of bacteriology* 192.13 (2010), pp. 3259–3267.

[218] S. Trinschek, K. John, S. Lecuyer, and U. Thiele. "Continuous versus Arrested Spreading of Biofilms at Solid-Gas Interfaces: The Role of Surface Forces". *Physical review letters* 119.7 (2017), p. 078003.

[219] J. Dervaux, J. C. Magniez, and A. Libchaber. "On growth and form of Bacillus subtilis biofilms". *Interface focus* 4.6 (2014), p. 20130051.

[220] X. Wang, S. Meng, and J. Han. "Morphologies and phenotypes in Bacillus subtilis biofilms". *Journal of Microbiology* 55.8 (2017), pp. 619–627.

[221] M. Fauvart, P Phillips, D Bachaspatimayum, N. Verstraeten, J. Fransaer, J. Michiels, and J. Vermant. "Surface tension gradient control of bacterial swarming in colonies of Pseudomonas aeruginosa". *Soft Matter* 8.1 (2012), pp. 70–76.